10-19-2022

INVESTIGATION OF POLYMER NANOCOMPOSITES WITH SILICON DIOXIDE FILLERS AS HELIUM COOLED HIGH-TEMPERATURE SUPERCONDUCTING CABLE DIELECTRICS

Jordan Thomas Cook
Rowan University

Recommended Citation

Cook, Jordan Thomas, "INVESTIGATION OF POLYMER NANOCOMPOSITES WITH SILICON DIOXIDE FILLERS AS HELIUM COOLED HIGH-TEMPERATURE SUPERCONDUCTING CABLE DIELECTRICS" (2022). *Theses and Dissertations*. 3068.
https://rdw.rowan.edu/etd/3068

INVESTIGATION OF POLYMER NANOCOMPOSITES WITH SILICON DIOXIDE FILLERS AS HELIUM COOLED HIGH-TEMPERATURE SUPERCONDUCTING CABLE DIELECTRICS

by

Jordan Thomas Cook

A Thesis

Submitted to the
Department of Mechanical Engineering
College of Engineering
In partial fulfillment of the requirement
For the degree of
Master of Science in Mechanical Engineering
at
Rowan University
May 31, 2021

Thesis Chair: Wei Xue, Ph.D., Associate Professor, Department of Mechanical Engineering, Robert R. Krchnavek, Ph.D., Professor, Department of Electrical and Computer Engineering

Committee Members:
Francis Haas, Ph.D., Assistant Professor, Department of Mechanical Engineering
Behrad Koohbor, Ph.D., Assistant Professor, Department of Mechanical Engineering

Dedications

I would like to dedicate this manuscript to my parents, Ronald Cook and Joanna Kabshura-Cook. Your constant support and encouragement, to push myself past what I though was possible, has allowed me to reach this point. Overcoming the moments of uncertainty and frustration wouldn’t have been possible without you, and I cannot thank you enough for everything.

Acknowledgments

I would like to express my deepest gratitude to my advisor, Dr. Wei Xue. Through your patience and encouragement, I have been able to grow into a better engineer, researcher, and person. Every second I have spent under your guidance, has made me better off. I would also like to extend a thank you to Dr. Robert Krchnavek for both his guidance and rigor in all project decisions. I would also like to thank Dr. Lei Yu for his extensive organic chemistry knowledge and assistance with FTIR and TGA characterization.

I want to thank my friends and lab mates, Muhammet E. Cavusoglu, Rhandy Paladines, Nicholas Pagliocca, Kemal Yakut, and Mahsa Raeisinezhad for making my time in the lab more memorable. I would like to thank my friends and coworkers, Michael McCaffrey and Jacob Mahon for supporting me, through the work we conducted together. Additionally, I want to thank the undergraduate engineering clinic students for all their hard work and commitment which was essential to progressing the project forward. Finally, a special thank you to Harrison Hones for being an amazing friend and coworker, who supported me in even the most minor of tasks.

Lastly, the work presented within this manuscript was made possible by the Department of Defense under the Naval Surface Warfare Center's (NSWC) Naval Engineering Education Consortium (NEEC) program, grant number NSWC IHEODTD N00174-17-1-0008). Support was also provided by the National Science Foundation with the grant number CBET #1625816. I would also like to thank the Applied Superconductivity team at the Naval Surface Warfare Center Philadelphia Division, for their continued guidance and expertise on cryogenic dielectrics and systems.

Abstract

Jordan Thomas Cook
INVESTIGATION OF POLYMER NANOCOMPOSITES WITH SILICON DIOXIDE FILLERS AS HELIUM COOLED HIGH-TEMPERATURE SUPERCONDUCTING CABLE DIELECTRICS
2021-2022
Wei Xue, Ph.D., and Robert R. Krchnavek, Ph.D.
Master of Science in Mechanical Engineering

In this thesis, three polymer nanocomposite configurations are fabricated for investigation as dielectrics in helium-cooled high-temperature superconducting (HTS) cables. Polyimide, polyamide, and polymethyl methacrylate are utilized as host polymers. The composite samples are synthesized through an in situ process, dispersing silicon dioxide nanoparticles throughout the polymer hosts. Fourier transform infrared spectroscopy and scanning electron microscopy were employed to validate the synthesis of each composite configuration. Thin film samples of each configuration were also tested for their dielectric strength at both room (300 K) and cryogenic (92 K) temperatures. When going from room to cryogenic temperatures, all materials demonstrated a significant increase in dielectric strength. This increase in strength is explained through an expanded, temperature dependent breakdown model. Currently, apparatuses necessary for further material validation as cable coatings, as well as at temperatures as low as 55 K, have been designed and are being manufactured for further experimentation. The continued efforts of this research can ultimately lead to the ideal polymer nanocomposite configuration for use as an HTS cable dielectric.

Table of Contents

Abstract v

List of Figures ix

List of Tables xii

Chapter 1: Introduction 1

- 1.1. HTS Cables and Applications 1
- 1.2. Dielectric Considerations 4
- 1.3. Polymer Nanocomposites 8
  - 1.3.1 Host Matrix - Polyimide 9
  - 1.3.2 Host Matrix – Polyamide 10
  - 1.3.3 Host Matrix - Polymethyl Methacrylate 11
  - 1.3.4 Nanoparticle – Silicon Dioxide 12
- 1.4 Dielectric Breakdown in Polymer Nanocomposites 14
- 1.5 Cryogenic Testing Chamber 16
- 1.6 Cable Coating 18
- 1.7 Motivation and Objectives 19
- 1.8 General Layout of Thesis 20

Chapter 2: Material Preparation 21

- 2.1 Nanoparticle Generation 21
- 2.2 Polymer Nanocomposite Fabrication 23
  - 2.2.1 Polyimide-SiO_2 Preparation 24
  - 2.2.2 Polyamide-SiO_2 Preparation 27
  - 2.2.3 PMMA-SiO_2 Preparation 29

Table of Contents (Continued)

2.3 Attempted Fabrication Methods 30

2.3.1 Ex Situ Dispersion 31

2.3.2 PMMA Preparation..31

2.3.3 Low Temperature Imidization: PI...33

Chapter 3: Material Validation and Characterization Methods 35

3.1 Scanning Electron Microscopy (SEM) 35

3.1.1 Energy-Dispersive X-ray Spectroscopy..37

3.2 Thermogravimetric Analysis 40

3.3 Fourier-Transform Infrared Spectroscopy 42

3.3.1 Imidization of Polyamide..42

3.3.2 PMMA Validation 43

3.3.3 Low Temperature Imidization Attempts..45

3.4 Dielectric Breakdown Testing 48

3.4.1 Room Temperature Testing 49

3.4.2 Cryogenic Temperature Testing 50

Chapter 4: Material Characterization Results 53

4.1 Nanoparticle Dispersion...53

4.2 Dielectric Breakdown of Polyimide...58

4.3 Dielectric Breakdown of Polyamide..63

4.4 Dielectric Breakdown of PMMA...67

4.5 Expanded Model of Dielectric Breakdown Mechanisms 71

4.6 Discussion of All Composite Configurations 73

Table of Contents (Continued)

Chapter 5: Material Validation Apparatuses....................75

5.1 Wire Coating....................75

5.1.1 Cable Coating Set-Up....................75

5.1.2 Cable Coated Dielectric Breakdown Fixture....................80

5.2 55 K Testing Chamber Design....................83

5.3 55 K Dielectric Breakdown Fixture....................86

Chapter 6: Conclusions and Future Works....................89

6.1 Summary....................89

6.2 Future Works....................93

References....................97

List of Figures

Figure Page

Figure 1. Diagram of a LN_2 Cooled, Three-Phase HTS Cable, Housed Within a Cryostat 2

Figure 2. Diagram of a Cryogenic Cooling Loop Used in a Naval HTS Cable Feasibility Study [11] 4

Figure 3. Schematic of the Permeation of Multi-Layer Lapped Dielectric Tape by Helium Atoms 5

Figure 4. Contraction Rate of HTS Cable Cores (in red) Compared with the Rates of Other Common Cryogenic Materials [17] 7

Figure 5. Diagram of the Mismatch of CTE and Subsequent Shrinkage Between Extruded Polymers and HTS Cable Cores 7

Figure 6. A Section of a Nanocomposite with the Host Polymer Chains Oriented Around the Nanoparticles 9

Figure 7. Chemical Structure of Polyimide 10

Figure 8. Chemical Structure of Polyamide 11

Figure 9. Chemical Structure of Polymethyl Methacrylate 12

Figure 10. Silica Nanoparticles Under a SEM (left) and a TEM (right) After Formation in a Sol Gel for In Situ Composite Fabrication 14

Figure 11. A Schematic of the Multi-Core Model of Polymer Nanocomposite Dielectric Breakdown [45] 15

Figure 12. Gaseous Helium Cooling System Utilized for HTS Cable Cooling and Characterization [49] 17

Figure 13. The Stages of Nanoparticle Nucleation and Growth in a Sol Gel After Mixing Reagents [53] 22

Figure 14. General Nanocomposite Fabrication Process for All Nanocomposite Configurations Synthesized 24

Figure 15. Temperature Profile of the Curing Process of PI-SiO_2 Nanocomposites 26

Figure 16. Imidization Reaction of PAA Into PI Through the Removal of Two Water Molecules. 27

List of Figures (Continued)

Figure 17. Temperature Profile of the Curing Process of PI-SiO_2 Nanocomposites........ 29

Figure 18. Chemical Structure of the Polymerization Reaction of MMA into PMMA ... 32

Figure 19. Reaction of a Carboxylic Acid Group with Thionyl Chloride 34

Figure 20. SEM Image of (A) PI-SiO_2, (B) PA-SiO_2, and (C) PMMA-SiO_2 Nanocomposites with 4% Filler Concentrations.. 36

Figure 21. Elemental Map of Silicon of a 5% wt. PA-SiO_2 Composite Sample Obtained Through SEM-EDS [55] 38

Figure 22. EDS Maps of Silicon for (A) PI and (B) PMMA Based Samples.................. 39

Figure 23. TGA Weight with Respect to Temperature of (A) 4% PA-SiO_2 Cured at 80°C, (B) 4% PA-SiO_2 Cured at 115°C, and (C) 4% PMMA-SiO_2 Cured at 125°C 41

Figure 24. FTIR Spectra of PA and PI... 43

Figure 25. FTIR Spectrum of Attempted PMMA Synthesis with a Circle over the Characteristic Peak of PMMA 44

Figure 26. FTIR Spectra of (A) Thionyl Chloride, (B) UV Curing, and (C) DMF+CaCl Low Temperature Imidization Experiments 46

Figure 27. Diagram of the Room Temperature Breakdown Fixture and Electrode Contact 50

Figure 28. Zoomed in View of the Cryogenic Breakdown Fixture 51

Figure 29. SEM Images and Histograms of 4% Composite Samples of (A) PI, (B) PA, and (C) PMMA 54

Figure 30. Average Dielectric Breakdown Performance of PI Based Samples at Room (300 K) and Cryogenic (92 K) Temperatures 59

Figure 31. Weibull Distributions for Room Temperature Breakdown Testing of 0-6% PI-SiO_2 Nanocomposites 60

Figure 32. Weibull Distributions for Cryogenic Temperature Breakdown Testing of 0-6% PI-SiO_2 Nanocomposites 60

Figure 33. SEM Images of Dielectric Breakdown Holes for 4% PI-SiO_2 Samples at Room (left) and Cryogenic (right) Temperatures... 63

List of Figures (Continued)

Figure 34. Average Dielectric Breakdown Performance of PA Based Samples at Room (300 K) and Cryogenic (92 K) Temperatures ... 64

Figure 35. Weibull Distributions for Room Temperature Breakdown Testing of 0-6% PA-SiO_2 Nanocomposites ... 64

Figure 36. Weibull Distributions for Cryogenic Temperature Breakdown Testing of 0-6% PA-SiO_2 Nanocomposites ... 65

Figure 37. SEM Images of Dielectric Breakdown Holes for 4% PA-SiO_2 Samples at Room (left) and Cryogenic (right) Temperatures ... 67

Figure 38. Average Dielectric Breakdown Performance of PMMA Based Samples at Room (300 K) and Cryogenic (92 K) Temperatures ... 68

Figure 39. Weibull Distributions for Room Temperature Breakdown Testing of 0-6% PMMA-SiO_2 Nanocomposites ... 68

Figure 40. Weibull Distributions for Cryogenic Temperature Breakdown Testing of 0-6% PMMA-SiO_2 Nanocomposites ... 69

Figure 41. SEM Images of Dielectric Breakdown Holes for 4% PMMA-SiO_2 Samples at Room (left) and Cryogenic (right) Temperatures ... 71

Figure 42. Temperature-Dependent Model Depicting the Impact of Temperature on (top) Pure Polymers and (bottom) Polymer Nanocomposites ... 72

Figure 43. Rendering of the Initial Proof of Concept Wire-Coating Design ... 76

Figure 44. Motor, Tachometer, and Speed Controller Set-Up Used to Run the Cable Coating System ... 77

Figure 45. Cable Analog After a PA Coating has Been Applied and Cured ... 79

Figure 46. Front and Side View of the Improved Cable Coating Fixture ... 80

Figure 47. Diagram of the Cable Coated Dielectric Breakdown Fixture ... 82

Figure 48. Schematic of the Closed Loop Gifford-McMahon Cryocooler System ... 84

Figure 49. Rendering of the 55 K Testing Chamber’s Inner and Outer Vacuum Chambers ... 86

Figure 50. Rendering of the 55 K Dielectric Breakdown Fixture ... 87

Figure 51. (A) Front and (B) Back of the 55K Dielectric Testing Fixture Plug Board ... 88

List of Tables

Table Page

Table 1. Equations Used in Sol Gel Precursor Mass Calculations for PI-SiO_2 Composite Fabrication 25

Table 2. Equation used in Sol Gel Mass Calculations for PA-SiO_2 Composite Fabrication 28

Table 3. Equation Utilized in Sol Gel Mass Calculations for PMMA-SiO_2 Composite Fabrication 30

Table 4. Weibull Scale and Shape Parameters for 0-6% PI-SiO_2 Concentration Distributions at Room (300 K) and Cryogenic (92 K) Temperatures 61

Table 5. Weibull Scale and Shape Parameters for 0-6% PA-SiO_2 Concentration Distributions at Room (300 K) and Cryogenic (92 K) Temperatures 65

Table 6. Weibull Scale and Shape Parameters for 0-6% PMMA-SiO_2 Concentration Distributions at Room (300 K) and Cryogenic (92 K) Temperatures 69

Table 7. Comparison of Polymer Composites’ Dielectric Strengths Across Various Studies....................92

Chapter 1

Introduction

1.1 HTS Cables and Applications

The development of high-temperature superconducting (HTS) cables is a field that has garnered much attention in recent years, due to the substantial increase in power transmission efficiency these cables can provide. HTS cables can provide up to 100 times the effective power density, at a fraction of both the cost of construction and weight, than those of conventional cables [1]. It is also possible to deliver a 200% increase in transmission capacity compared to traditional cable circuits by installing one three-core HTS cable in place of a conventional cable [1]. This increased efficiency is due to the embedded superconducting materials within their construction. Superconductors, when cooled below their critical temperature, exhibit near zero internal resistance, allowing for near 100% efficient power transmission [2]. The most common HTS cables utilize superconductors with critical temperatures above 90 K, but are cooled to 77 K with liquid nitrogen (LN_2) to improve performance [3]. These superconductors are fabricated into long cylinders around the core of the cables, allowing for either single or three-phase constructions. A dielectric material is also wrapped around the cable cores to insulate the superconductors, and separate phases in three-phase cables, as depicted in Figure 1 [4].

Figure 1

Diagram of a LN_2 Cooled, Three-Phase HTS Cable, Housed Within a Cryostat

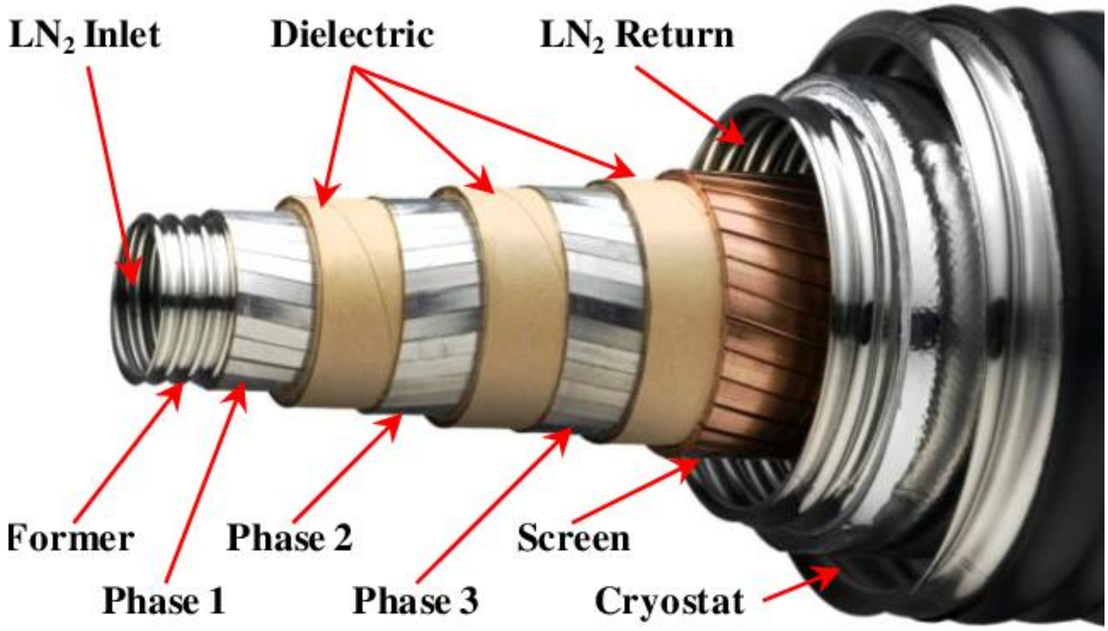

HTS cables provide a means of improving many high-power electrical systems, like those found in domestic and international power grids. According to the U.S. Department of Energy's Office of Electricity Delivery and Energy Reliability, roughly 10% of the energy generated is lost to the grid before it reaches the consumer [5]. As energy demands increase, the implementation of HTS cable systems can become a more efficient and cheaper option when constructing new conduit lines [1]. In addition, upgrading existing cable lines with HTS cables can also mitigate the need to construct new lines altogether. From the deficiencies associated with classical power transmission, several large-scale HTS cable projects exploring the feasibility of adopting superconducting cables into the power grids of countries around the globe have been undertaken [6-8].

HTS cable systems are also great candidates for use on naval ships which must be self-sufficient for extended periods of time. Navy ships need to minimize the weight and size of all their components while maximizing the power output generated on board to operate at sea. The need for maximized power output is highlighted by the operation of high-power systems such as Electromagnetic Aircraft Launching Systems (EMALS) on board naval ships. EMALS help launch aircraft off the ship when there is minimal space for takeoff. They can require up to 18 kA of current and 60 MW of peak power output to successfully initiate the launch of an aircraft [9]. Therefore, Once a sufficient amount of power is stored, low resistance transmission is paramount as up to 2 MW are lost to the internal resistance of conventional copper [9]. The lightweight construction and increased efficiency of HTS cables has sparked various feasibility studies into adopting these cable systems onto ships by naval researchers [10, 11]. An example of these feasibility study efforts can be seen in Figure 2 from Kephart *et al.* [11]. The system depicted cycled gaseous helium through a 50 m loop using four different cryostat sections to prove the potential of cooling long HTS cable sections. More extensive feasibility studies are expected as the U.S. Navy continues to explore adopting HTS systems onto naval vessels.

Figure 2

Diagram of a Cryogenic Cooling Loop Used in a Naval HTS Cable Feasibility Study [11]

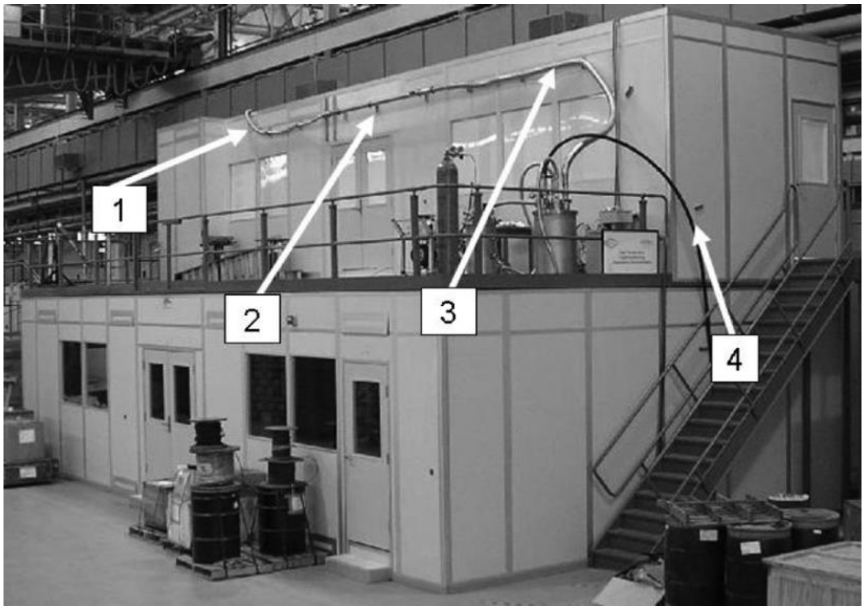

Note. The loop utilizes four different cryostat sections numbered 1 through 4, all from different vendors.

1.2 Dielectric Considerations

The dielectric layer of HTS cables is crucial in avoiding shorts and preserving efficiency. Most HTS cables are cooled with liquid nitrogen, which remains a liquid between 64 K to 77 K at 1 atm. These cables also utilize lapped dielectric tape as their dielectric. Recent naval research has determined the optimal operating temperature of HTS cables is 55 K, making the use of liquid nitrogen a less than optimal cryogen [10]. Citing this limitation, naval researchers have begun exploring other cryogen options such as gaseous helium. Helium remains a gas above 4 K and has added safety benefits, making it suitable as a coolant in HTS cables [10]. The use of gaseous helium, however, creates issues with using lapped tape as a dielectric layer. Lapped dielectric tape leaves gaps up to 0.1 µm wide that are large enough for helium atoms (0.49 Å in diameter) to permeate through, even with multiple layers of tape [12]. This issue results in electrical shorts within the cable and by extension, cable inefficiencies. The permeation issue, depicted in Figure 3, shows helium atoms permeating through multi-layer lapped dielectric tape.

Figure 3

Schematic of the Permeation of Multi-Layer Lapped Dielectric Tape by Helium Atoms

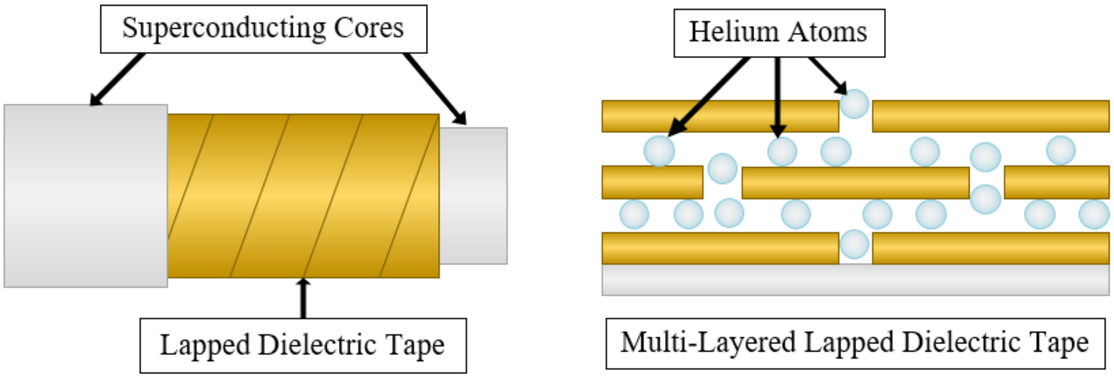

A less permeable option for gaseous helium cooled HTS cable dielectrics is polymer extrusion. Polymer extrusion is a common method of coating cables with a thermoset plastics [13]. In this process, a cable is pulled through a bath of liquid polymer, allowing it to adhere to the cable. The polymer is then heated and cured, forming one continuous and impermeable layer around the cable [14]. Polymers exhibit high dielectric strengths, as high as 640 kV/mm in some cases [15]. The HTS cables in question require dielectrics with strengths higher than 12 kV/mm, making polymers suitable candidates. Extruded polymers are still limited in this application due to their high thermal contraction rates, reflected by their high coefficients of thermal expansion (CTE), and high curing temperatures.

When cooled to 50 K from room temperature (293 K), polymers can contract by 0.6-2.7% of their initial length. The contraction rate of the gaseous helium cooled HTS cable cores, however, is 0.3% when cooled to the same temperature [5]. The different contraction rates of these two materials and other common cryogenic materials are illustrated in Figure 4 [5]. This mismatch in CTE between the polymers and the cable formers causes the polymers to reduce in length and contract tightly around the cores. The tightly bound polymers cause unnecessary stiffness and breakages, resulting in unwieldy and inefficient cables. A schematic displaying the differing CTE issue is shown in Figure 5. It is also important to consider the method of fabrication when applying the dielectric layer. In polymer extrusion, thermoset plastics require large amounts of heat to cure effectively. However, the HTS cables in question delaminate at temperatures above 175 °C [16]. The initial delamination can begin at temperatures as low as 140 °C, making 140 °C the upper temperature limit for the polymer extrusion process.

Figure 4

Contraction Rate of HTS Cable Cores (in red) Compared with the Rates of Other Common Cryogenic Materials [17]

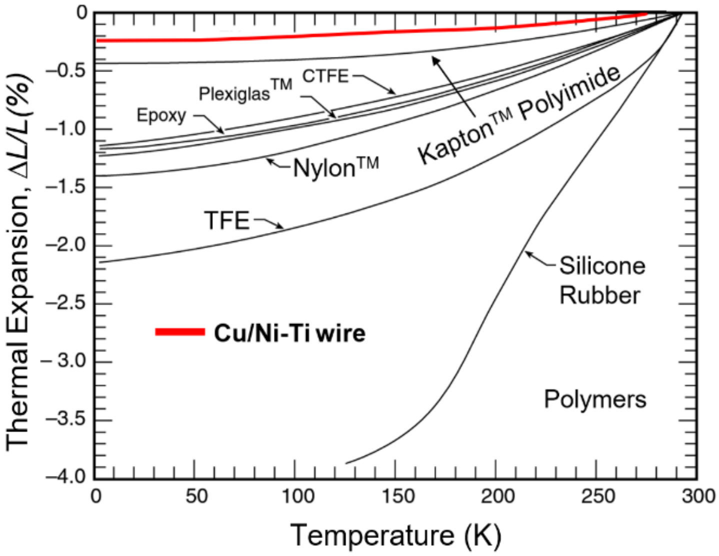

Figure 5

Diagram of the Mismatch of CTE and Subsequent Shrinkage Between Extruded Polymers and HTS Cable Cores

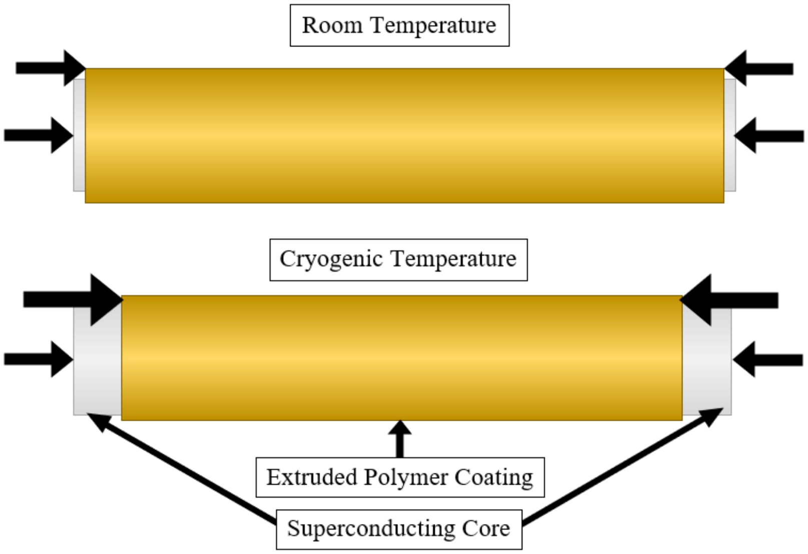

1.3 Polymer Nanocomposites

Composites are materials comprised of two (or more) dissimilar and/or discrete constituents with potentially superior properties. The phases that constitute a composite are the host matrix, or bulk phase, and the reinforcing or filler phase which is surrounded by the host matrix. Polymer nanocomposites are a form of composite where the bulk material, being some polymer, is loaded with a nanoscale filler. Nanocomposites with nanoparticle fillers can exhibit enhanced properties. In particular, they have shown an increased dielectric strength over their host matrix and other composites [18, 19]. A schematic of a nanocomposite with a nanoparticle filler is shown in Figure 6. The nature of nanocomposites being comprised of two or more different materials allows for control over the final mechanical properties of the composite. Adding a lower CTE nanofiller to a polymer has been proven effective in lowering the overall CTE of the final nanocomposite [20-22]. These two facts have led to the exploration of three polymer nanocomposite configurations for use in the helium cooled HTS cables.

Figure 6

A Section of a Nanocomposite with the Host Polymer Chains Oriented Around the Nanoparticles

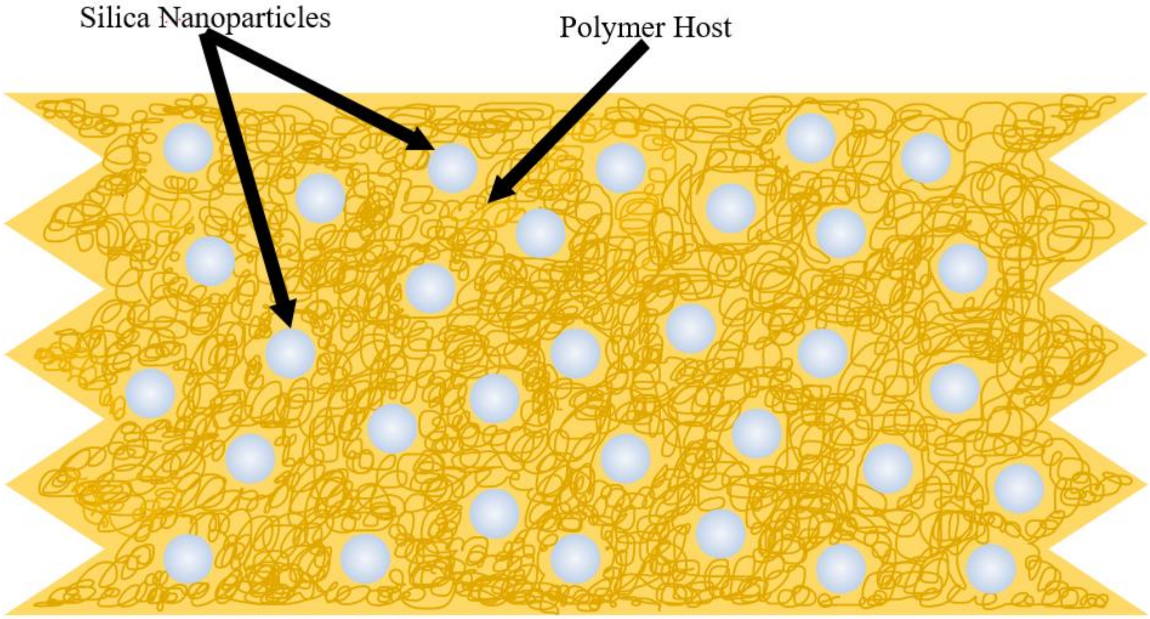

1.3.1 Host Matrix – Polyimide

Polyimide (PI) is an aromatic thermoset polymer and exhibits excellent dielectric strength with values of 100-300 kV/mm [23]. As a polymer, it exhibits a high CTE of 30-50 × 10−6 K−1 [24]. It was initially developed into a film known as Kapton by Dupont in the 1960s. Since its development, PI has been widely used as a dielectric in high temperature applications [25]. Off-the-shelf Kapton exists as a thin film or tape which does not readily allow for the introduction of nanoparticles. However, PI can be synthesized in-house from its precursor, polyamic acid (PAA) [25]. PAA formed through mixing pyromellitic dianhydride and oxydianiline produces poly(pyromellitic dianhydride-co-4,4′-oxydianiline) amic acid. Thermal curing then allows the excess solvents of this reaction to be removed and the process imidizes the PAA into PI. The chemical formula of PI after curing can be seen in Figure 7. PAA is a viscous liquid in its original form, making nanoparticle dispersion much more feasible. PI also demonstrates excellent mechanical properties with high flexibility and mechanical strength [26]. Citing the ease of synthesis and excellent mechanical properties, PI was selected as a potential host matrix for use in HTS cable dielectrics.

Figure 7

Chemical Structure of Polyimide

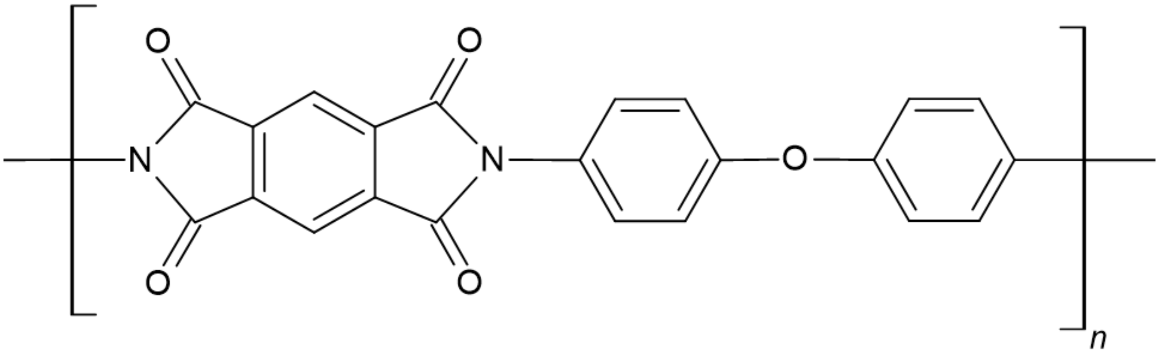

1.3.2 Host Matrix – Polyamide

Polyamides (PA) are another type of thermoset polymer similar to PI. PA is commercially available in many forms such as nylon and Nomex, which is a PA 6 aramid paper from Dupont. Nylon and Nomex are still subject to the same issues as Kapton when attempting to impregnate them with nanoparticles. PA is a precursor to PI, synthesized from PAA by halting the curing process before the imidization reaction takes place. Avoiding the imidization reaction, which requires temperatures >115 °C, enables a shortened curing process at lower temperatures [27]. The chemical formula of PA, as it is found in PAA, is depicted in Figure 8. The CTE of PA is slightly higher than that of PI with values ranging from 70–100 × 10−6 K−1 [28]. PA also exhibits a high dielectric strength with values ranging from 30-50 kV/mm on the low end, and as high as 460 kV/mm in some cases [29-31]. In a study previously published from this research, the average dielectric strength of PA was found to be 124 kV/mm [32]. PA exhibits excellent material and chemical properties, which are similar to PI, making it another excellent choice for a host matrix [33].

Figure 8

Chemical Formula of Polyamide

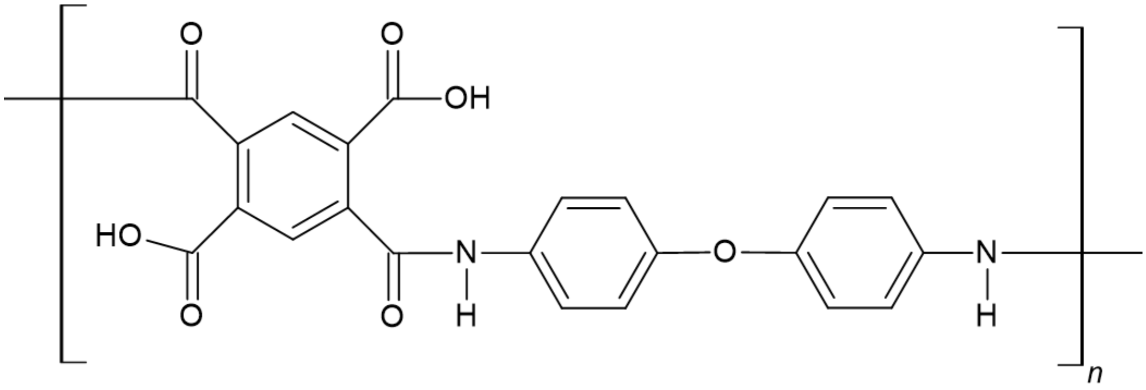

1.3.3 Host Matrix – Polymethyl Methacrylate

Polymethyl methacrylate (PMMA), also known as acrylic, is a thermoplastic with high transparency. PMMA, like the other polymers described previously, can be bought off-the-shelf but requires in-house preparation to introduce nanoparticles into it. PMMA is synthesized through the polymerization reaction of methyl methacrylate (MMA), which is PMMA’s monomer. For polymerization of MMA to take place, a catalyst, in the form of an additional reagent or UV light, must be introduced [34, 35]. PMMA is also available as a powder, allowing it to be dissolved in a solvent and cured to form the final polymer [36]. The chemical formula of PMMA can be seen in Figure 9. PMMA exhibits a lower dielectric strength than both PI and PA, with values ranging from 30-110 kV/mm [37]. The CTE of PMMA is comparable to that of PA with a value of about 70 × 10−6 K−1 [38]. This polymer also exhibits both high mechanical flexibility and low processing temperature with a glass transition temperature of 60-130 °C [37, 39]. These material properties make PMMA a suitable candidate for a host matrix in helium cooled HTS cables.

Figure 9

Chemical Structure of Polymethyl Methacrylate

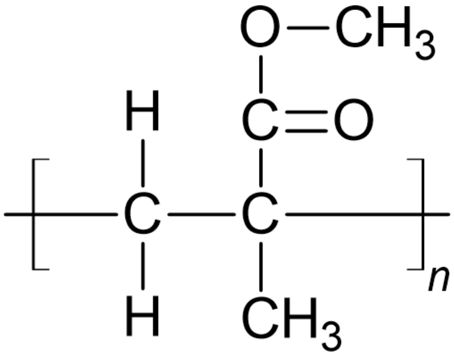

1.3.4 Nanoparticle – Silicon Dioxide

Silicon dioxide (silica, SiO_2) is the nanoparticle filler selected for use in the three host matrices described previously. SiO_2 is also a well-known insulator with dielectric strengths reported as high as 1000 kV/mm, depending upon purity [40]. Silica can be introduced to the host polymer through either in situ or ex situ processes. In situ nanocomposite fabrication involves synthesizing SiO_2 in-house through the use of a sol gel before being added to the polymer host [41, 42]. The ex situ process requires dried nanoparticles to be dispersed in another medium before being introduced to the host matrix [42]. An example of SiO_2 nanoparticles formed through a sol gel can be seen in Figure 10 [43]. This figure depicts images of dried silica nanoparticles under a scanning electron microscope (SEM) and a transmission electron microscope (TEM). The details of both in situ and ex situ processes are discussed in Chapter 2. Adding nanoparticles to a polymer has been found to increase the material's overall dielectric strength, furthering its efficacy as a dielectric [18]. However, the realistic strength requirement for helium cooled HTS cable dielectrics (~12 kV/mm) makes any change in dielectric strength a negligible concern when adding SiO_2 to a host polymer (typically higher than 100 kV/mm). The main drawback of silica is its low CTE with expansion/contraction rates 15-20 times lower than polymers like PI [17, 44]. Therefore, by controlling the concentration of silica in the composite, it may be possible to match the CTE of the final material to that of the HTS cable cores.

Figure 10

Silica Nanoparticles Under a SEM (left) and a TEM (right) After Formation in a Sol Gel for In Situ Composite Fabrication [43]

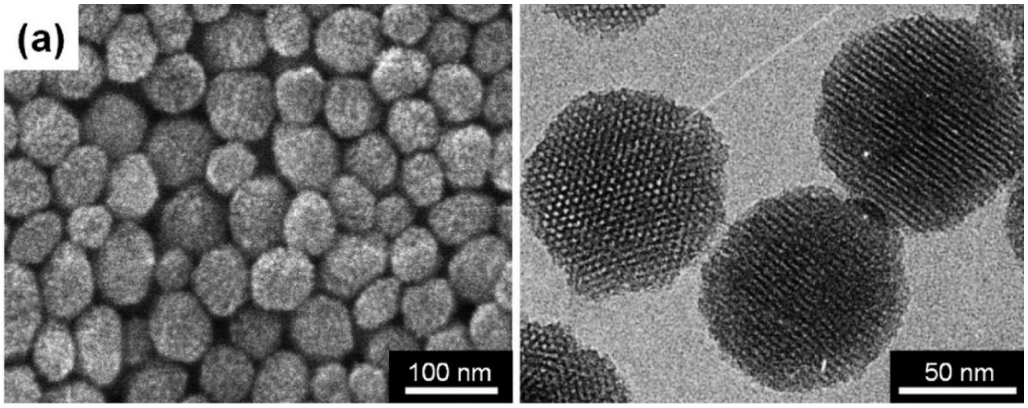

1.4 Dielectric Breakdown in Polymer Nanocomposites

The use of polymer nanocomposites as dielectrics has seen rigorous exploration in recent years. Multiple models depicting the mechanisms behind dielectric breakdown have been proposed such as Coulomb blockade effects, space charge, and multi-core models [45]. Of these models, the multi-core model, proposed by Tanaka, is the most widely accepted in describing polymers impregnated with oxide-based nanoparticles [18, 46]. This model has been expanded upon by Li et al. and is depicted in Figure 11 [45]. The model is comprised of a bonded region, transition region, and a normal region which are layers that form around the nanoparticle as the composite is cured. The bonded layer is formed due to unsaturated bonds at the ends of polymer chains bonding with the surface of the nanoparticle. These bonds cause the formation of the transition region which is characterized by tightly bound polymer chains bonded to the bonded region. The normal region exists outside the transitional layer where the host polymer orients randomly around the nanoparticle [18, 45].

Figure 11

A Schematic of the Multi-Core Model of Polymer Nanocomposite Dielectric Breakdown [45]

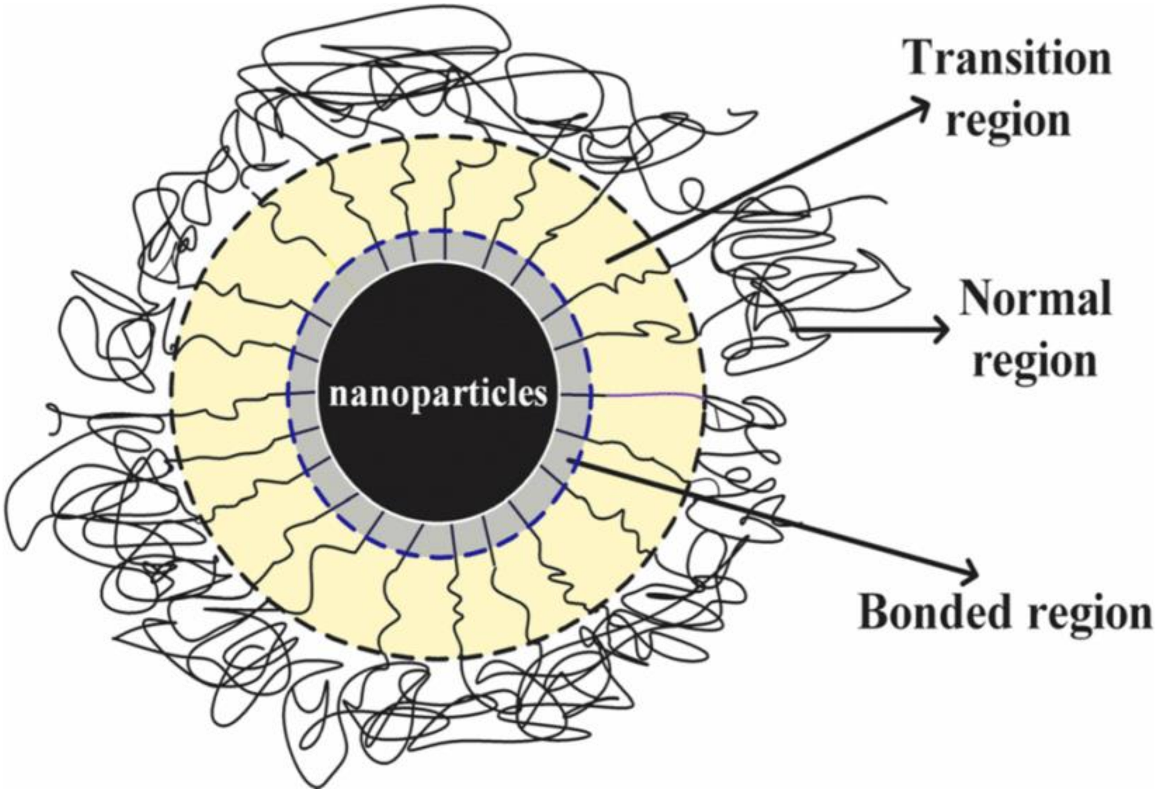

The transition and bonded regions introduce free volumes, or large spaces inside entangled polymer chains, into the nanocomposite which directly impact mobile charges during breakdown. These two layers also directly lower the overall permittivity of the final nanocomposite [45]. In addition, the bonded and transition regions alter the energy band structure of the composite. These alterations to the material properties, introduced through the layers of this model, are used to explain the increased dielectric strength seen in multiple oxide-based nanoparticle polymer composites [18]. It is also important to note that for most composites, estimation of material properties like dielectric strength can be attained through the rule of mixtures. The rule of mixtures employs the respective volume fractions of the host matrix and filler for a rough estimation of mechanical properties. However, this means of estimation is inaccurate when considering nanoparticle fillers due to their interaction with the polymer host and the layers they introduce into the bulk material. Therefore, Experimentation is required to understand the dielectric breakdown strength of a polymer nanocomposite [47].

1.5 Cryogenic Testing Chamber

Characterization of the polymer nanocomposites explored in this research currently takes place at room and cryogenic temperatures using liquid nitrogen (>77 K). These composites also need to be tested in a helium environment at 55 K to ensure they function as expected in the cables. Delivering a 55 K helium rich environment is difficult as there is a lack of research on gaseous helium as a cryogen. The few systems developed to achieve this environment are used primarily for cooling and testing HTS cable sections, not their individual components [48, 49]. Two examples of HTS cable section cooling systems can be seen in Figure 12 [49].

Figure 12

Gaseous Helium Cooling System Utilized for HTS Cable Cooling and Characterization [49]

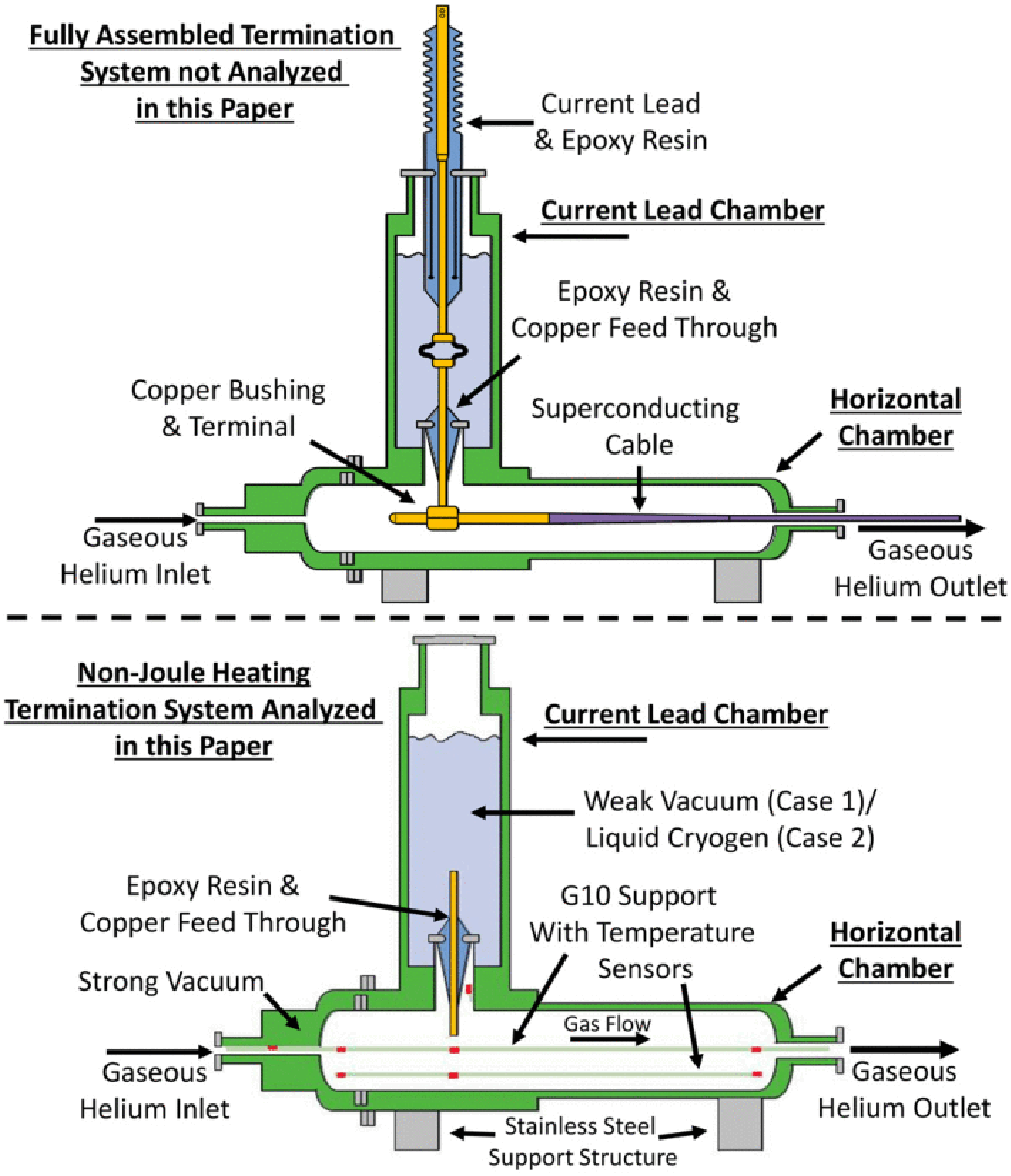

The solution to this issue is to adapt a gaseous helium cooling cycle for material characterization. This can be realized by manufacturing a custom cryogenic testing chamber that connects to the cooling cycle. Through the generosity of the Applied Superconductivity Team of the Naval Surface Warfare Center Philadelphia Division (NSWCPD), a cryocooler has been provided to us, making this solution possible. This cryocooler is capable of delivering 40 K gaseous helium environments with heaters to control the operating temperature. The cryogenic testing chamber has been designed to incorporate a dielectric testing rig for breakdown at 55 K, with plans to adapt it for other measurements, such as CTE, in the future.

1.6 Cable Coating

When fabricating polymer nanocomposites, the easiest method is spin coating which is the focus of this research. Spin coating involves applying the material to a substrate and spinning the substrate at high speeds to achieve an even thin film [50]. The film is then heated to evaporate the solvent and cure the composite. As thin films, nanocomposites act as excellent dielectric tapes but remain permeable to helium, citing the same issues as conventional lapped tapes. Eliminating the permeation and CTE mismatch issues with conventional dielectric layers would require utilizing polymer extrusion for an impermeable layer. Adapting polymer extrusion to utilize polymer nanocomposites could deliver an impermeable and CTE-matched dielectric coating. It is important to note that extruding nanocomposites onto a round wire would yield an altered dielectric strength compared to thin film data. The dielectric strength of a material is affected by its geometry, requiring a comparison between thin films and extruded coatings to validate the performance of the nanocomposite material as a cable coated dielectric [12].

1.7 Motivation and Objectives

The research undertaken in this work focuses on determining the ideal dielectric for use in helium cooled HTS cables. The nature of helium as a cryogen presents critical challenges in current dielectric options, leading to the investigation of polymer nanocomposites for this application. With careful material consideration and varying filler concentration, the material properties of a polymer nanocomposite can be adjusted to potentially match the CTE of helium cooled HTS cable cores. Previous research into the subject of helium cooled HTS cables has been conducted, but the majority of the work presented here is unique as it proposes three polymer nanocomposite configurations specifically as HTS cable cryogenic dielectrics in a comparative study. The motivation for this research leads to two main overarching goals: development and characterization of three potential polymer nanocomposites. Once achieved, the focus shifts to the validation of the materials as a cable coating dielectric and at the 55 K operating temperature.

The objectives to accomplish these goals include:

1. Fabricate thin film PI-SiO_2, PA-SiO_2, and PMMA-SiO_2 polymer nanocomposites.
2. Validate nanocomposite materials and conduct dielectric breakdown tests on the three composites with varying SiO_2 loadings to determine ideal configurations and concentrations for use in HTS cables.
3. Determine the dielectric performance of the composite configurations and the impact temperature has on dielectric strength.

4. Develop apparatuses to characterize the nanocomposites on a cable analog and at 55 K.

1.8 General Layout of Thesis

The 2nd chapter of this thesis will focus on material preparation. In said chapter, the methods of nanoparticle generation and the final thin film curing processes for all three nanocomposite configurations are described. All previous fabrication methods attempted are also detailed. In Chapter 3, material characterization methods through SEM, thermogravimetric analysis (TGA), Fourier-transform infrared spectroscopy (FTIR), and dielectric breakdown are all outlined. SEM and FTIR are used to validate each nanocomposite configuration to prove the composition of their constituent phases. The different methods employed for both room and cryogenic breakdown testing are also described in detail. The results of the material characterization are discussed in Chapter 4 with a dielectric strength comparison of all three host matrices at both room and cryogenic temperatures. The mechanisms behind breakdown and the results presented are explained through existing models and a proposed, expanded model. Chapter 5 contains the apparatuses that have been designed to aid in further material validation. This includes the design of a wire coating rig, a dielectric breakdown tester for nanocomposite wire coatings, and a 55 K cryogenic testing chamber. Chapter 6 concludes this thesis with a summary of the work conducted and a discussion of the future works planned as this project enters its final year.

Chapter 2

Material Preparation

2.1 Nanoparticle Generation

The method utilized for nanoparticle integration is critical for achieving evenly dispersed nanoparticles. The method focused on in this research is *in situ* as it was found to deliver a superior dispersion to *ex situ*. The *ex situ* process will be discussed later in this chapter. *In situ* nanoparticle generation begins with the formation of a sol gel in which nanoparticles nucleate and grow from a mixture of reagents. The term sol gel describes a combination of a sol, a colloid of particles in a liquid, and a gel which is a network of pores [51]. Many forms of the sol gel process exist with varying levels of control over the final size and the dispersion of nanoparticles [52]. A diagram of the sol gel process can be seen in Figure 13, depicting the nucleation, growth, and stabilization of nanoparticles within the sol gel [53]. The specific sol gel process utilized in this work for SiO_2 synthesis is the Stöber process, ©n which deionized water (DI water), ethanol (EtOH), tetraethyl orthosilicate (TEOS), and hydrochloric acid (HCl) form the sol gel [54]. The EtOH, TEOS, and HCl were all procured from Sigma Aldrich with concentration percentages of >99.5%, 98%, and 37% respectively.

Figure 13

The Stages of Nanoparticle Nucleation and Growth in a Sol Gel After Mixing Reagents [53]

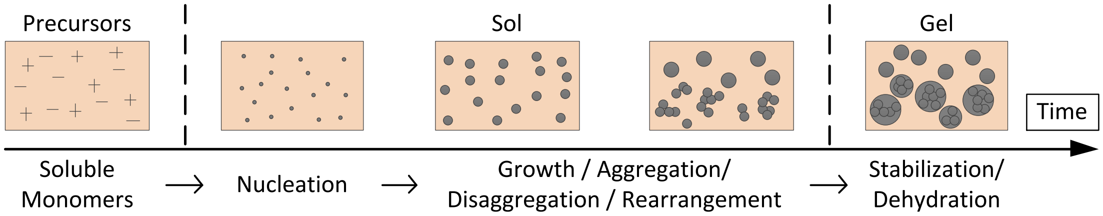

The sol gel is formed by mixing the four reagents in a 2:1:1:1 molar ratio of DI water, EtOH, TEOS, and HCl respectively, as per the Stöber process [54]. For ease of fabrication, the molar ratio was converted to a weight percent ratio of 11.03% DI water: 14.09% EtOH: 63.73% TEOS: 11.15% HCl. When mixing the reagents, the DI water and EtOH were mixed together first with the TEOS and HCl also being mixed separately. The two solutions were then combined to form the sol gel. This order of mixing was proven experimentally to provide the most reliable sol gel synthesis. Once combined, the sol gel is stirred with a magnetic stir bar spinning at 300 RPM for 30 minutes. The solution is also covered and placed in an ice bath to mitigate evaporation of any reagents due to the exothermic nature of the reaction. After the 30-minute mixing period, the silica nanoparticles have been formed and are ready for dispersion in the polymer host. The final sol gel is slightly acidic which is advantageous, as silica's solubility increases in alkaline solutions [51].

2.2 Polymer Nanocomposite Fabrication

Fabrication of the polymer nanocomposites is accomplished through four steps, nanoparticle and host matrix preparation, dispersion within the host, thin film preparation, and curing, as depicted in Figure 14. PI-SiO_2, PA-SiO_2, and PMMA-SiO_2 nanocomposites all utilize a similar fabrication process with alterations depending upon the host matrix in question. They are also all fabricated with 0%, 2%, 4% and 6% filler concentrations. The general fabrication process begins with host polymer preparation, in which the host polymer precursor is prepared and weighed for accurate silica concentration calculations. *In situ* nanoparticle synthesis, as previously described, is employed for all composite configurations to form the nanoparticles in the final material. Once the host polymer and sol gel are prepared, the sol gel is poured into the host matrix and mixed for 4 hours with a magnetic stir bar. The resulting composite is poured onto 75 mm × 25 mm microscope slides and spin coated to prepare the thin films. The general spin coating method is conducted in two steps. Composite coated slides are initially accelerated to 1000 RPM over the course of 10 seconds, followed by spinning at 1000 RPM for 45 seconds. This spin coating profile was proven experimentally to yield the most even and reliable thin films [55]. Spin coated slides are then moved to a hot plate where they are thermally cured according to the curing process needed for each of the host polymers. Once finished, the composite thin films are removed from the hot plate and the yielded films share the same length and width as the microscope slides.

Figure 14

General Nanocomposite Fabrication Process for All Nanocomposite Configurations Synthesized

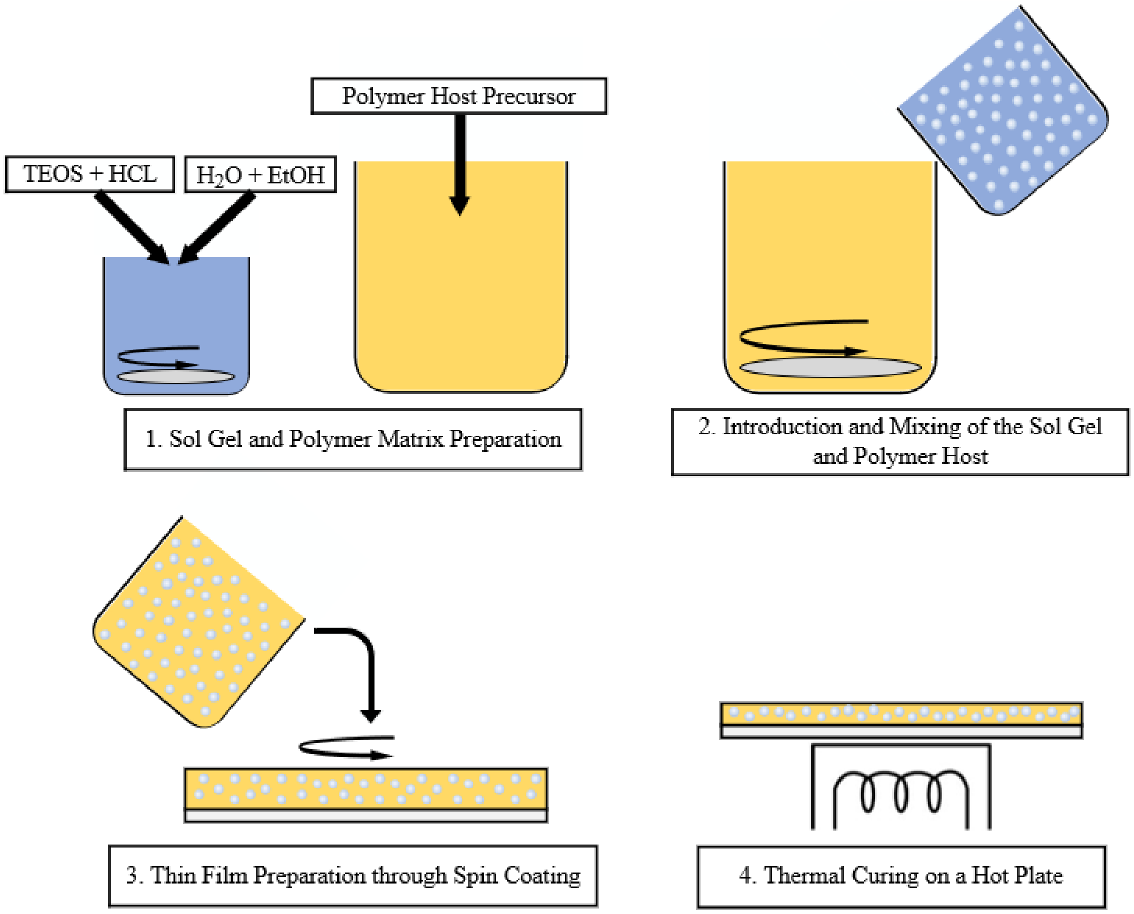

2.2.1 *Polyimide-SiO_2 Preparation*

Synthesis of PI-SiO_2 nanocomposites follows the general composite fabrication method and relies on PAA as the polymer precursor. Poly(pyromellitic dianhydride-*co*-4,4′-oxydianiline) amic acid solution was purchased off-the-shelf from Sigma Aldrich with a weight percent of 15 ∓ 5%. For accurate SiO_2 loadings, the final weight percentages of cured PI and dried silica were verified experimentally. The weight of the polymer host was proven experimentally to be 13.8% of the PAA precursor. The slight decrease from the listed 15% is attributed to the nature of the imidization reaction removing an OH^- group and a H^+ group from either end of the polymer chain in the form of water [56]. The final weight percentage of the dried silica was determined to be 18.38% of the sol gel. These percentages, as well as the mass of the PAA and the desired SiO_2 concentration, are used to determine the mass of the sol gel and its components via Equations (1-5) in Table 1. It is important to note that the mass of the sol gel (m_{solgel}) and its components are dependent upon both the desired concentration (n) and the mass of the PAA (m_{PAA}).

Table 1

Equations Used in Sol Gel Precursor Mass Calculations for PI-SiO_2 Composite Fabrication

To determine mass of:	Equation	Number
PI sol gel	$m_{solgel} = \frac{n}{1-n} \times \frac{m_{PAA} \times 0.138}{0.1838}$	(1)
EtOH	$m_{EtOH} = 0.1409 \times m_{solgel}$	(2)
TEOS	$m_{TEOS} = 0.6373 \times m_{solgel}$	(3)
HCl	$m_{HCl} = 0.1115 \times m_{solgel}$	(4)
H_2O	$m_{H2O} = 0.1103 \times m_{solgel}$	(5)

Once the sol gel and PAA are mixed, PI-SiO_2 nanocomposites continue with the general fabrication process, ending with the specific curing profile for PI. A graph of temperatures for each phase of the curing profile can be seen in Figure 15. Curing PI is a multi-step process beginning with heating at 80 °C for 30 minutes followed by heating at 100 °C for

10 minutes. These steps work to vaporize the solvents within the PAA and leave behind PA. The details of the conversion from PAA to PA is described in greater detail in the following Section 2.2.2. The samples are then slowly brought up to 250 °C, in 25 °C increments every 5 minutes. The temperature is maintained at 250 °C for 30 minutes during which the majority of the imidization from PA to PI takes place [57]. The imidization reaction from raw PAA to the final PI can be seen in Figure 16. A final step of thermal annealing at 370 °C for 10 minutes finishes the curing process. Finalized PI-SiO_2 thin films are measured with a Mitutoyo digital micrometer and are found to have an average thickness of 14.7 µm.

Figure 15

Temperature Profile of the Curing Process of PI-SiO_2 Nanocomposites

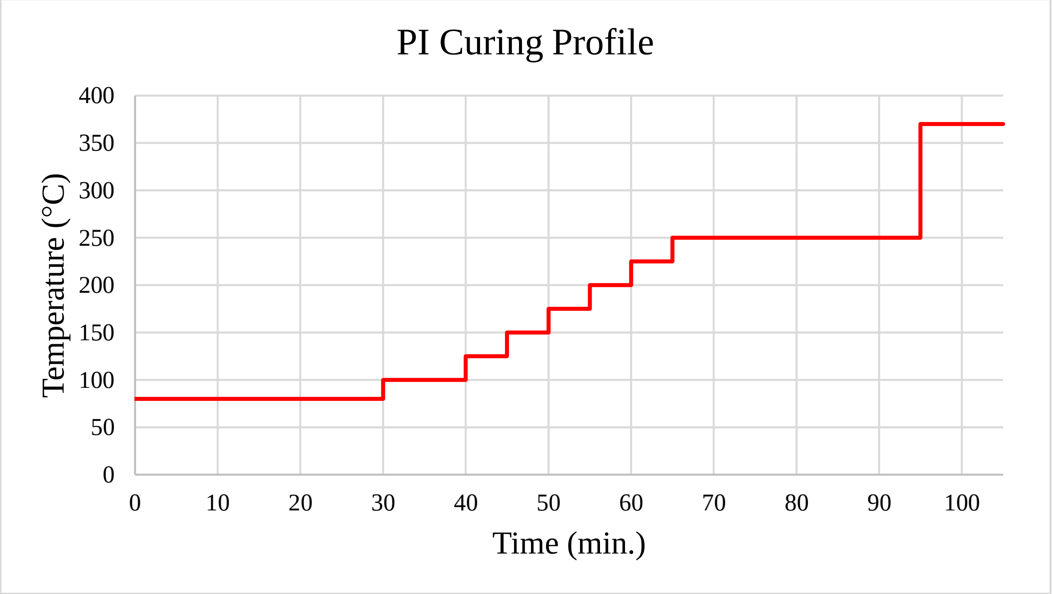

Figure 16

Imidization Reaction of PAA Into PI Through the Removal of Two Water Molecules

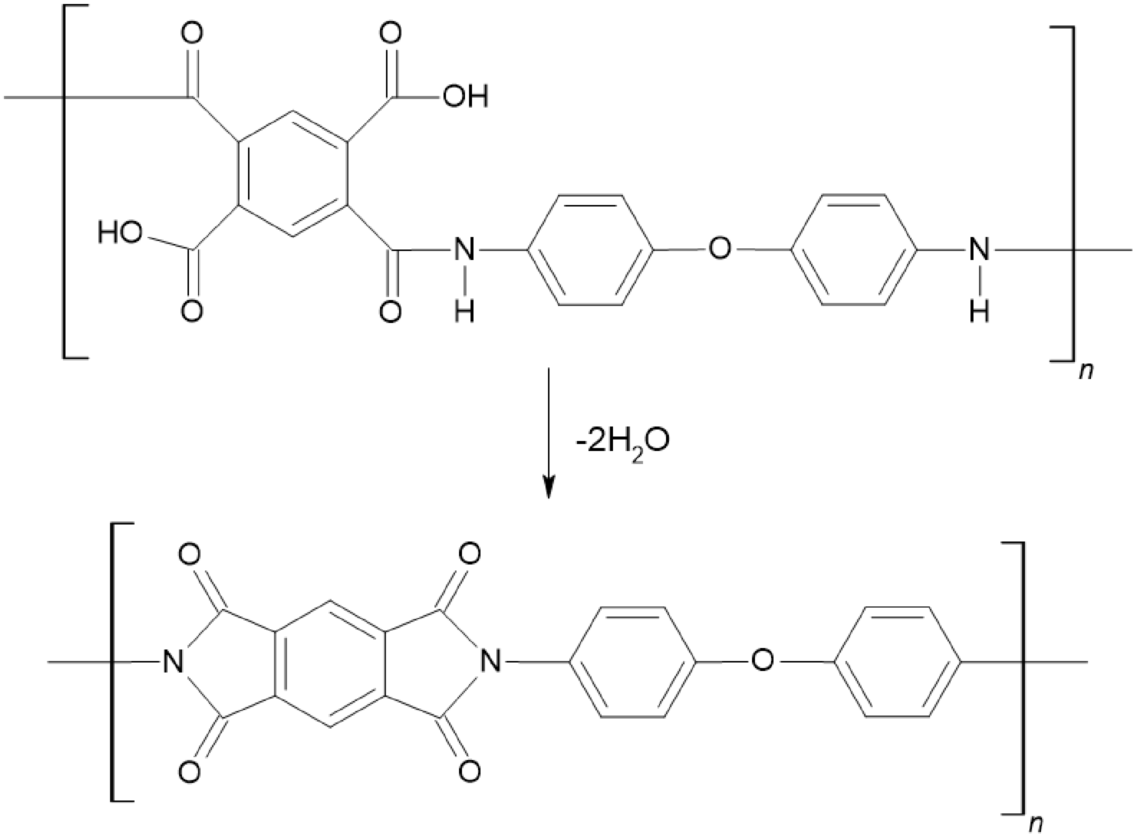

2.2.2 Polyamide-SiO₂ Preparation

The fabrication process for PA-SiO_2 nanocomposites is nearly identical to that of PI-SiO_2 samples with two minor changes relating to calculating filler concentration and the curing process. The final weight percentage of PA from the PAA precursor used in concentration calculations is 15%, as listed by the manufacturer. Adjusting for this, the equation for determining the mass of the sol gel in PA-SiO_2 samples is depicted in Table 2. The curing profile is also much simpler than that of PI, because only the solvents within the PAA need to be vaporized to prepare the final PA-SiO_2 samples. A graph of the curing profile for PA is shown in Figure 17. The curing process utilizes the same initial steps of heating at 80 °C for 30 minutes and 100 °C for 10 minutes. The spin coated samples are then heated at 115 °C for 15 minutes to ensure all solvents are removed from the PAA precursor, resulting in PA-SiO_2 thin films. The average thickness of PA-SiO_2 thin films is greater than that of PI-SiO_2 with a mean value of 23.8 µm. The increased thickness of PA-SiO_2 is a result of the lower curing temperature being unable to densify the films like that of the PI-SiO_2 curing process.

Table 2

Equation used in Sol Gel Mass Calculations for PA-SiO_2 Composite Fabrication

To determine mass of:	Equation	Number
PA sol gel	$m_{solgel} = \frac{n}{1-n} \times \frac{m_{PAA} \times 0.15}{0.1838}$	(6)

Figure 17

Temperature Profile of the Curing Process of PI-SiO₂ Nanocomposites

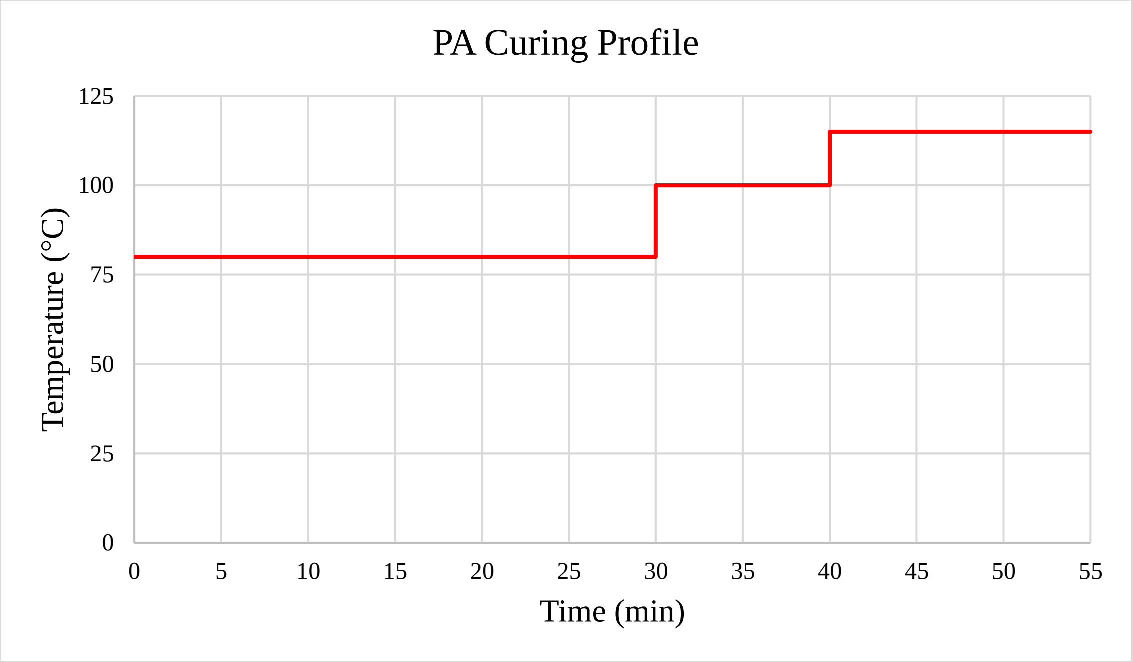

2.2.3 PMMA-SiO$_2$ Preparation

Fabrication of PMMA-SiO$_2$ samples begins with host matrix preparation. PMMA is purchased as a powder from Sigma Aldrich with a molecular weight of 996,000 g/mol. The PMMA powder is then dissolved in dimethyformamide (DMF) in a 1:8 weight ratio respectively. The two materials are heated on a hot plate at 125 °C for 10 minutes to fully dissolve the PMMA and form the host matrix solution. This weight ratio yields a final weight percent of 11.11% for PMMA and the resulting sol gel mass equation, Equation (7), can be seen in Table 3. Equations (2-5) are also employed for the weights of each sol gel precursor. Once formed, the sol gel is introduced to the PMMA solution and let mix for four hours as per the general fabrication method. Prior to spin coating, the PMMA solution is further heated to increase its viscosity for reliable thin film preparation. The solution is heated at 125 °C for one hour and 45 minutes. After solvent reduction, the composite is spin coated onto slides with one notable change from the general fabrication process. All composite samples follow the general spin coating profile; however, pure PMMA samples are accelerated to 1500 RPM for 10 seconds followed by spinning for 45 seconds at the same speed. This higher speed of 1500 RPM, instead of the typical 1000 RPM speed, was necessary to prepare samples with similar thicknesses (20-30 µm) to the composite samples. Spin coated PMMA-SiO_2 samples are then cured at 125 °C for 30 minutes to remove the DMF from the final material. The average thickness of PMMA samples is 29.0 µm.

Table 3

Equation Utilized in Sol Gel Mass Calculations for PMMA-SiO_2 Composite Fabrication

To determine mass of:	Equation	Number
PMMA Sol gel	$m_{solgel} = \frac{n}{1-n} \times \frac{m_{PAA} \times 0.1111}{0.1838}$	(7)

2.3 Attempted Fabrication Methods

Multiple fabrication methods were considered for each composite configuration. This includes several attempts at different nanoparticle dispersions, in-house polymer synthesis, and improvements to current methods. The characterization and results of these efforts are described in Chapter 3, via Fourier-transform infrared spectroscopy (FTIR).

2.3.1 Ex Situ Dispersion

Ex situ nanoparticle dispersion was utilized with 20 nm and 80 nm SiO_2 nanoparticles. The nanoparticles were mixed for 30 minutes with dimethylacetamide (DMAc) with a 1:15 respective weight ratio using an ultrasonicator to disperse the nanoparticles. After dispersion, the mixture is dropped into the polymer host and mixed for four hours, similar to the *in situ* method. *Ex situ* dispersion allows for ease of fabrication without requiring any nanoparticle synthesis. However, the ease of fabrication comes at a cost of uneven nanoparticle dispersion. In *ex situ* methods, the nanoparticles agglomerated considerably more than with *in situ* methods, creating defects and weak points within the nanocomposite [55]. Improving *ex situ* dispersion would require introducing a new material to the dried nanoparticles as a form of surface modification [58]. However, surface modification would mitigate the ease of manufacturing which made *ex situ* desirable in the first place. The addition of a new material to the silica could also negatively impact the material properties of the final composite, leading to *ex situ* being abandoned in favor of *in situ*.

2.3.2 PMMA Preparation

PMMA polymerization from its monomer, MMA, was attempted by mixing 15 g of MMA with 0.87 g of sodium dodecyl sulfate, and 0.75 g of potassium persulfate, in 100 mL of water [59]. MMA and PMMA after the polymerization reaction are depicted in Figure 18. The mixture was placed in a ultrasonication bath and heated to 65 °C for one hour to create a dispersion and begin the reaction. After sonication, the mixture was transferred to a petri dish within a nitrogen rich glove bag and heated at 70 °C for 15 hours to finish the reaction and dry the polymer. A nitrogen rich environment was utilized to mitigate any interaction between oxygen in the air and the polymerization reaction. These methods, however, failed to synthesize PMMA due to the available equipment lacking the necessary control for effective PMMA synthesis.

Figure 18

Chemical Structure of the Polymerization Reaction of MMA into PMMA

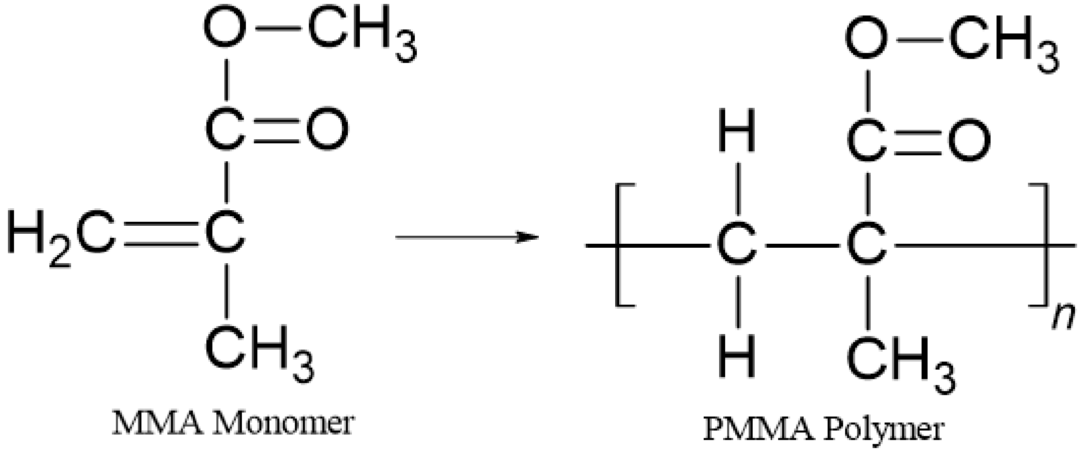

Preparation of PMMA was further attempted through dissolving pre-purchased PMMA powder in readily available solvents. Specifically, two solvents, acetone and toluene, were also employed to dissolve the PMMA powder before DMF was selected as the final solvent. Acetone was mixed with PMMA in weight ratios of 5:1 and 10:1. Various spin speeds and curing temperatures were utilized but all experiments resulted in PMMA samples that would crack and break when removed from the slides. By comparison, toluene, was found to yield desirable PMMA thin films when used to dissolve PMMA in an 8:1 weight ratio. However, toluene still failed as an effective solvent for PMMA preparation as silica particles instantly precipitated and agglomerated when the sol gel was added to the solution.

2.3.3 Low Temperature Imidization: PI

The curing profile for PI requires at least 250 °C to fully imidize the PA to PI without including the 370 °C thermal annealing step. Curing at these temperatures is much higher than the 140 °C delamination temperature of the HTS cables explored in this research. Significant efforts were made to induce the imidization reaction at lower temperatures. These efforts included utilizing thionyl chloride as a low temperature imidization catalyst, employing UV light and low temperature curing, and mixing PAA with DMF and water absorbers [60-62]. The results of these efforts will be discussed in Chapter 3.

Thionyl chloride is a common chemical catalyst and readily reacts with acids like PAA. The goal is to use thionyl chloride to react with the carboxylic acid groups in PAA and replace them with carbonyl-chloride groups [60]. This would enable lower temperature imidization as the chloride ion dissociates bonds easier than the hydroxyl ion. The general chemical formula of the formation of acid chlorides is depicted in Figure 19. Thionyl chloride as an imidization catalyst was experimented with by using an excess amount of DMF to dissolve the PAA. Thionyl chloride was then added to the mixture in an equimolar ratio to the PAA and mixed at 70 °C for 7 hours. The resulting solution was passed through a gravity filter to remove any excess thionyl chloride and is rinsed with DMF. The material was subsequently spin coated onto microscope slides before being left to dry overnight at room temperature. After drying, the acid-chloride was cured at 100 °C for an hour followed by curing at 120 °C for another hour.

Figure 19

Reaction of a Carboxylic Acid Group with Thionyl Chloride

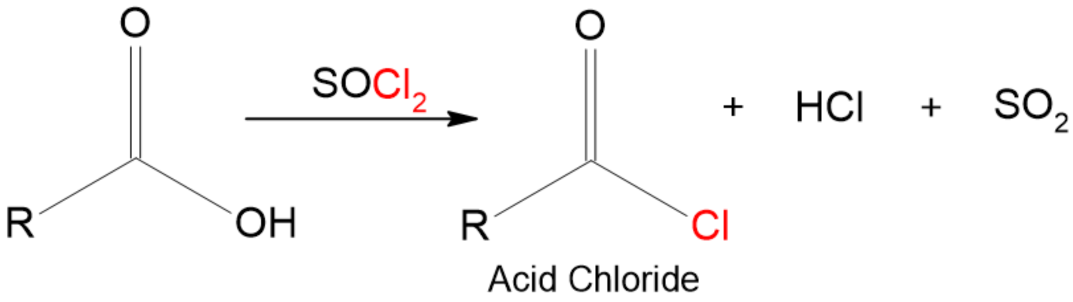

PAA, while a thermoset polymer, can also be imidized through the use of UV light [61]. UV light was employed in tandem with low temperature curing in two experiments. PAA was spin coated onto microscope slides and cured at 120 °C for two hours. The slides were separated into three groups: a control group and two test groups. The two test groups were both subjected to UV light from an OAI 200 system for 66 minutes each at a distance of either 5 cm or 15 cm from the UV bulb. The goal of the experiment was to show a difference in imidization percent across all three sample groups.

The final attempt at low temperature imidization relied on a similar process to the thionyl chloride experiment. PAA was mixed with 10% DMF by weight to dissolve the PAA. DMF being a polar solvent could break down the hydroxyl group bond, allowing for lower temperature curing [62]. A water absorber, in the form of calcium chloride ($CaCl_2$), was added to the solution in a 1.5:1 molar ratio with respect to the PAA to absorb the water formed from the reaction. The mixture was stirred for 30 minutes before being spin coated onto microscope slides. To cure, the slides were heated from 50 °C to 120 °C in 10 °C increments every 30 minutes.

Chapter 3

Material Validation and Characterization Methods

3.1 Scanning Electron Microscopy (SEM)

Thin film samples were imaged with an FEI Apreo SEM. SEM was utilized to validate the impregnation of the host polymers with silica nanoparticles and to examine nanoparticle sizes and dispersion. Samples were prepared for use in the SEM by adhering them to stainless-steel stubs (1 cm in diameter) with carbon tape. The samples were cut into squares roughly 1 cm wide before being placed on the stubs. Proper sample preparation is imperative for adequate imaging of insulating materials to preemptively address electron accumulation on the material's surface. Charge buildup occurs in insulating materials as the charges from the SEM's electron beam have no conductive path to move through, which results in unclear and distorted images [63]. To mitigate this, copper tape was placed over the edges of the nanocomposite films, making the samples more conductive. Samples were cut at random spots on the thin films for PA-SiO_2, PI-SiO_2, and PMMA-SiO_2 to thoroughly examine nanoparticle size. Images of 4% silica loadings for all three composite configurations are shown in Figure 20. Further discussion of nanoparticle sizes and dispersions will be covered in Chapter 4.

Figure 20

SEM Image of (A) PI-SiO$_2$, (B) PA-SiO$_2$, and (C) PMMA-SiO$_2$ Nanocomposites with 4% Filler Concentrations

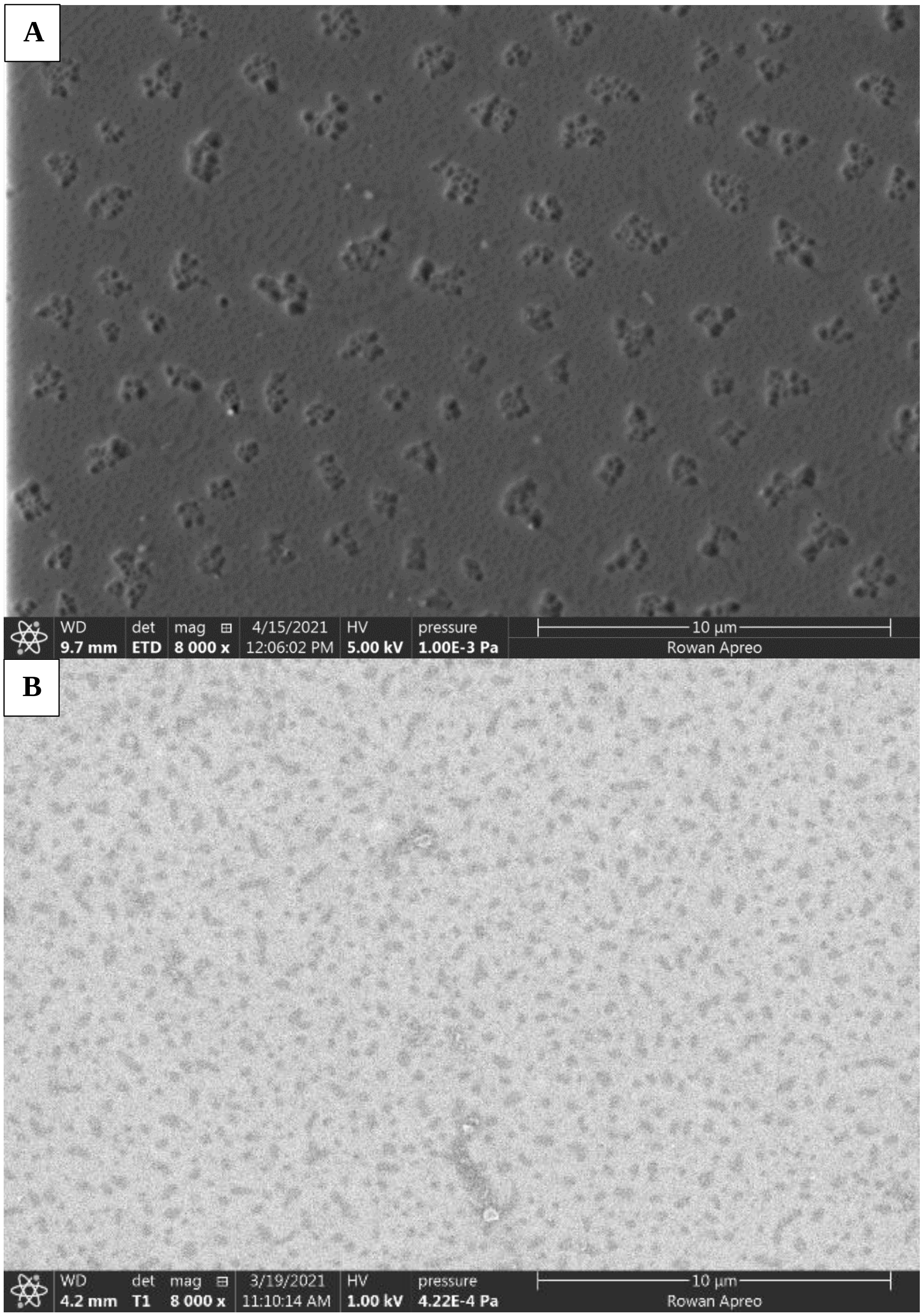

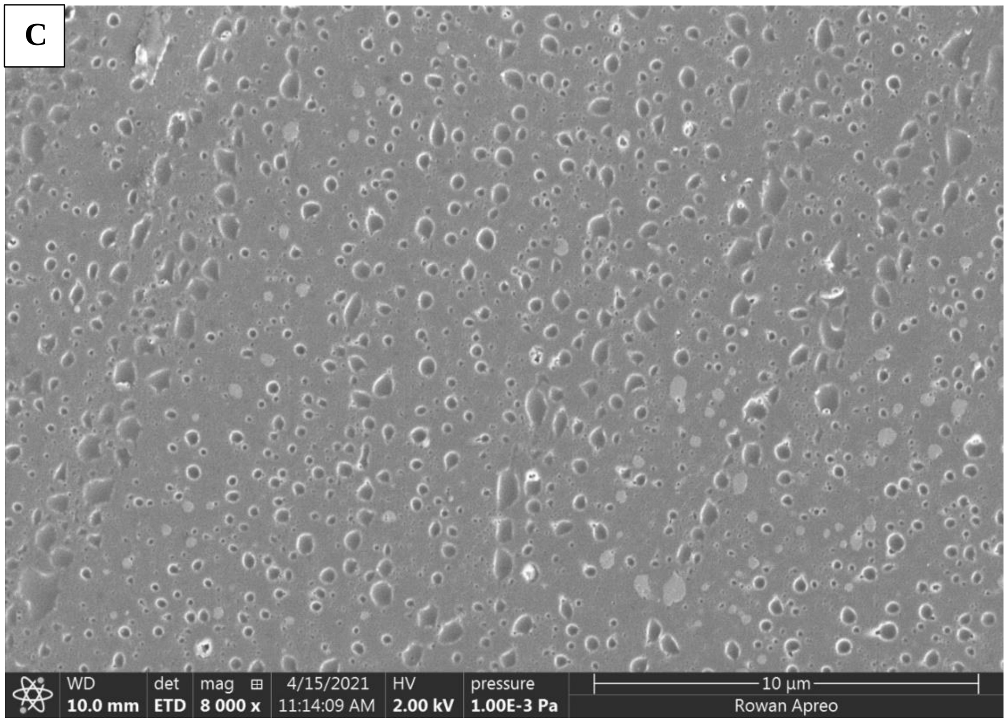

3.1.1 *Energy-Dispersive X-ray Spectroscopy*

To further validate the nanocomposite configurations, energy-dispersive X-ray spectroscopy (EDS) mapping was employed. EDS mapping allows for the spectra of individual elements to be observed and mapped over an SEM image. The system creates maps for all elements present and allows for specific elements to be examined. To prove the nanoparticles being imaged were SiO_2 nanoparticles, the map of silicon was generated for a PA-SiO_2 sample with a 5% filler concentration, as seen in Figure 21 [55]. Figure 21 shows the EDS map of silicon in red while the black areas represent the other elements present. Silicon's map in Figure 21 displays circular particles, verifying the Stöber process was successful in impregnating silica nanoparticles into the polymer hosts. EDS mapping was also attempted on both PMMA and PI based samples, but the process was found to yield poor mappings. The nature of EDS mapping requires higher accelerating voltages and currents than those values used in general SEM imaging. These high voltages and currents led to the degradation of PMMA and PI samples before maps could accurately be generated. Silicon was present in both of these mappings as depicted in Figure 22, but the maps were too degraded to observe nanoparticle geometries.

Figure 21

Elemental Map of Silicon of a 5% wt. PA-SiO_2 Composite Sample Obtained Through SEM-EDS [55]

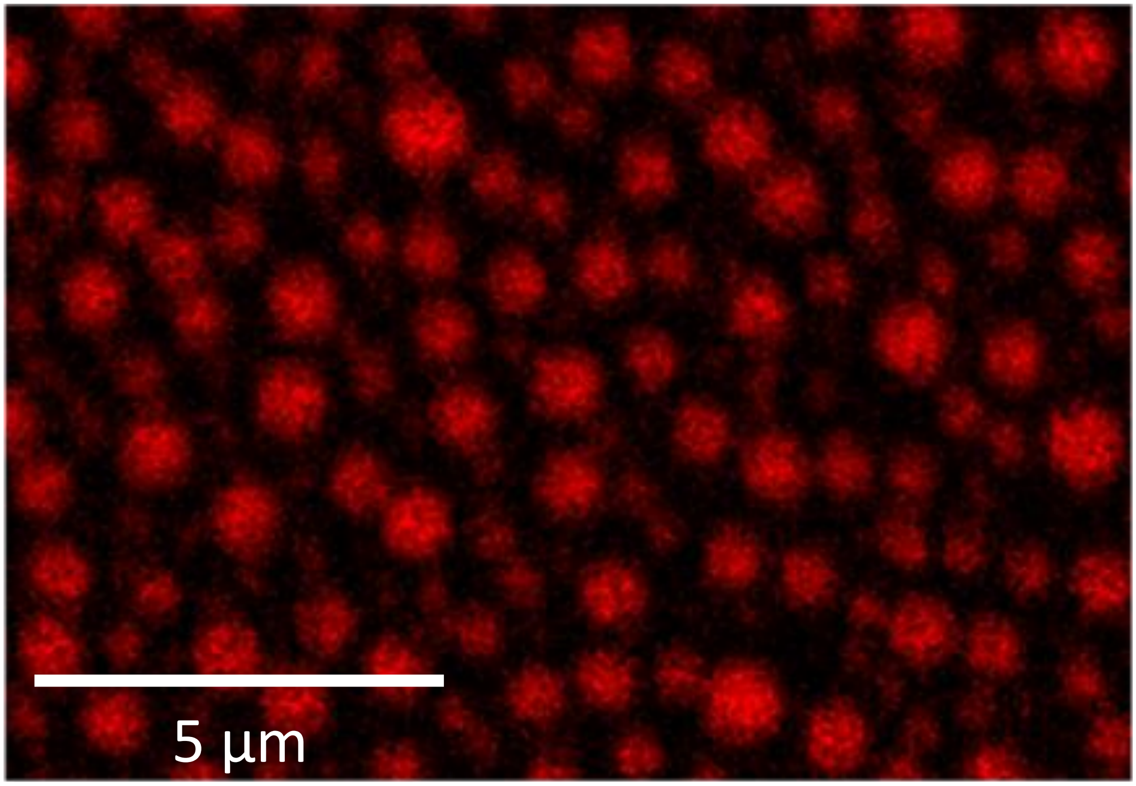

Note. Silicon content in the map is highlighted in red while all other elements appear in black.

Figure 22

EDS Maps of Silicon for (A) PI and (B) PMMA Based Samples

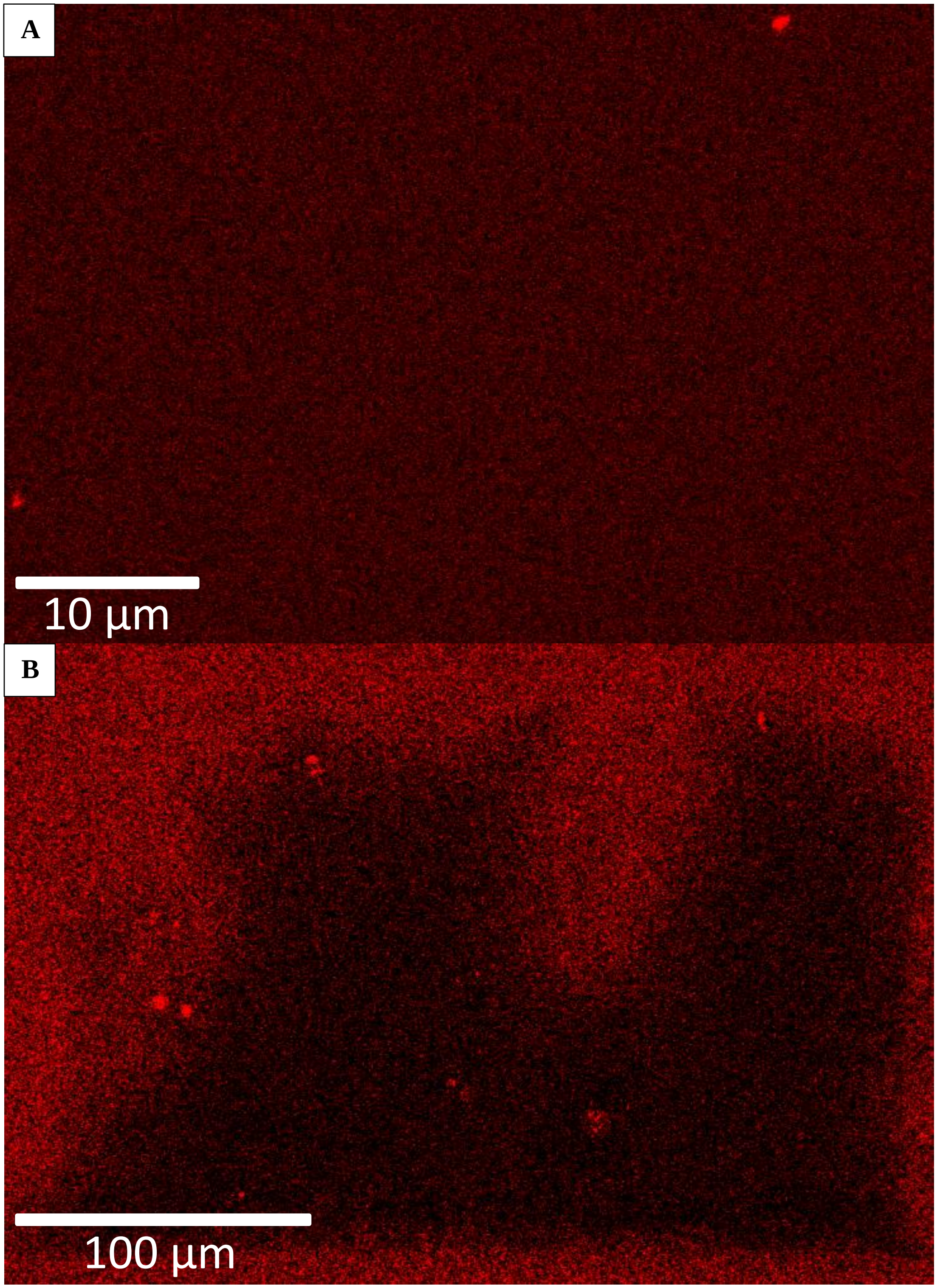

3.2 Thermogravimetric Analysis

A thermogravimetric analyzer operates by measuring the mass of a sample as it is subjected to high temperatures. This instrument helps identify any meaningful change in mass that takes place in a material as temperature increases. This is particularly useful in identifying phase change and carbonization. TGA was employed to inspect whether all the solvents in each material were completely removed at the end of material preparation. To conduct this experiment, a 4% PMMA-SiO_2 sample and a 4% sample of PA-SiO_2 were inspected by slowly increasing their temperature in the TGA to at least 700 °C over the course of 60-75 minutes. The PMMA sample was prepared normally but the PA-SiO_2 sample was cured at 115 °C instead of 125 °C in the final step of its curing process. This change was made to ensure that no imidization took place during the process. An additional control sample of 4% PA-SiO_2 was also prepared by curing at 80 °C for 30 minutes. The results of these experiments can be seen in Figure 23. The mass of the PA-SiO_2 control group demonstrated an abrupt drop in mass at 100 °C, indicating the solvent in its PAA precursor was still present. This drop was absent in the 115 °C cured PA sample which confirmed that no solvents were left in PA-SiO_2 based samples. The subsequent mass decreases were caused by the change in mass from the imidization process and from carbonization. By extension, it can be assumed that PI based samples also had no solvents left in final samples due to its higher curing temperatures. The PMMA sample, however, showed a slight decrease in mass after 125 °C followed by a more considerable drop in mass at 275 °C, due to carbonization. The first small decrease in mass suggested that DMF was likely still present in the final composite.

Figure 23

TGA Weight with Respect to Temperature of (A) 4% PA-SiO$_2$ Cured at 80°C, (B) 4% PA-SiO$_2$ Cured at 115°C, and (C) 4% PMMA-SiO$_2$ Cured at 125°C

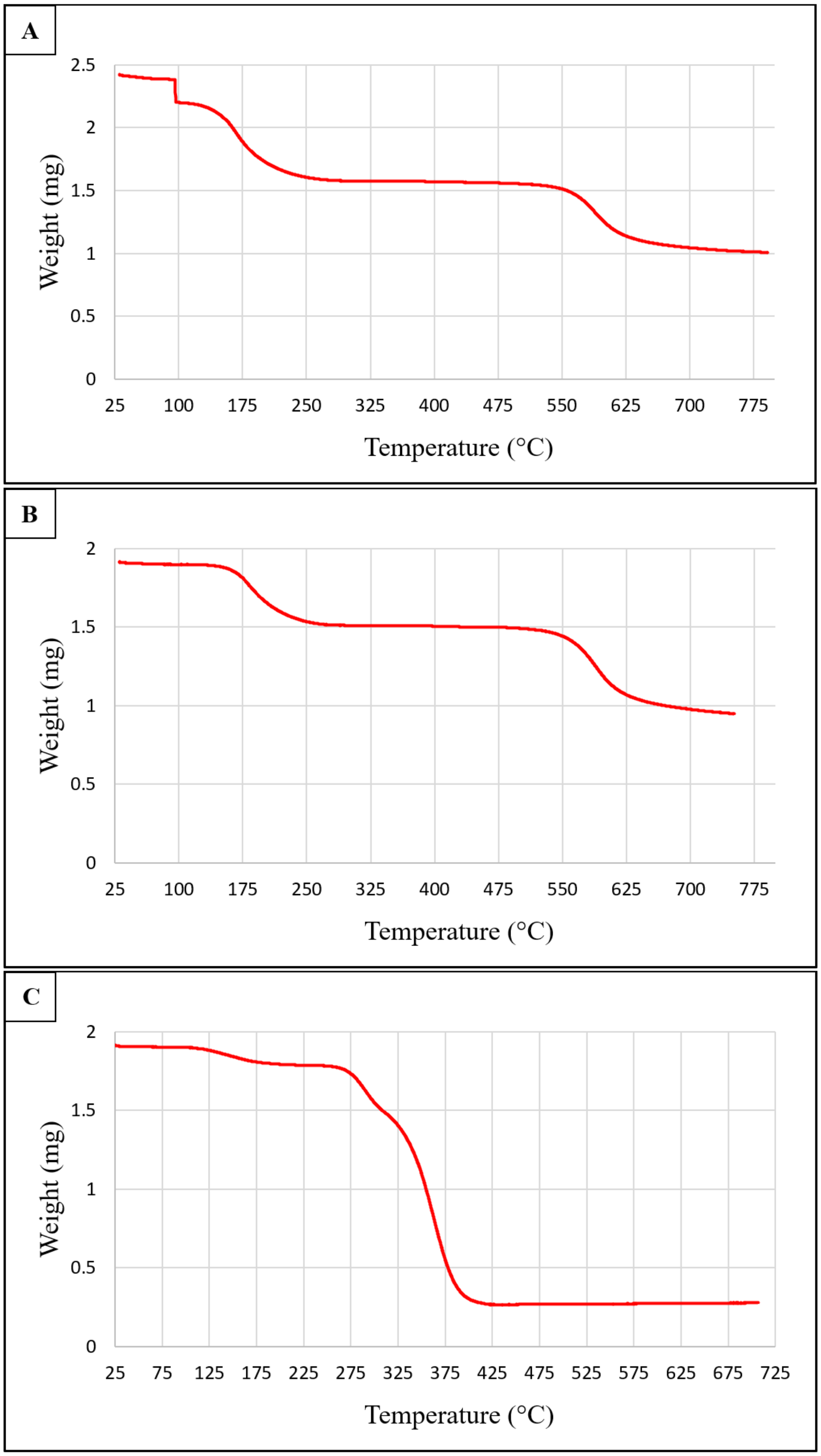

3.3 Fourier-Transform Infrared Spectroscopy

FTIR determines a material's unique absorption of the infrared spectrum between 400 and 4000 cm^{-1} wavelengths by exposing the material to a light source [64]. The absorption spectrum includes signature peaks which can be used to verify the composition of a material. FTIR is used to validate the host matrices used in material preparation and confirm the chemical processes that have taken place in material synthesis. To accomplish this, a Varian FTS 7000 FTIR spectrometer with a resolution of 1 cm^{-1} was utilized for measurements on all materials.

3.3.1 Imidization of Polyamide

The imidization reaction from PA to PI was examined under FTIR. Pure PA and PI samples were prepared, and their respective spectra were collected as seen in Figure 24. The signature peaks of PA and PI are denoted with stars. Peaks on the PA sample at 1399, 1538, ~1630, and ~2500-3500 cm^{-1} confirms the samples are PA. Imidization is characterized by a shrinking of these signature peaks and the rise of peaks at 720, 1364, and 1782 cm^{-1}. These changes indicate the closing of the imide band of PA, forming PI. The PI sample displayed the necessary changes at these peaks, confirming the imidization reaction took place [65-67]. FTIR was also collected on 4% composite samples for PI and PA, with identical spectra to those of pure samples.

Figure 24

FTIR Spectra of PA and PI

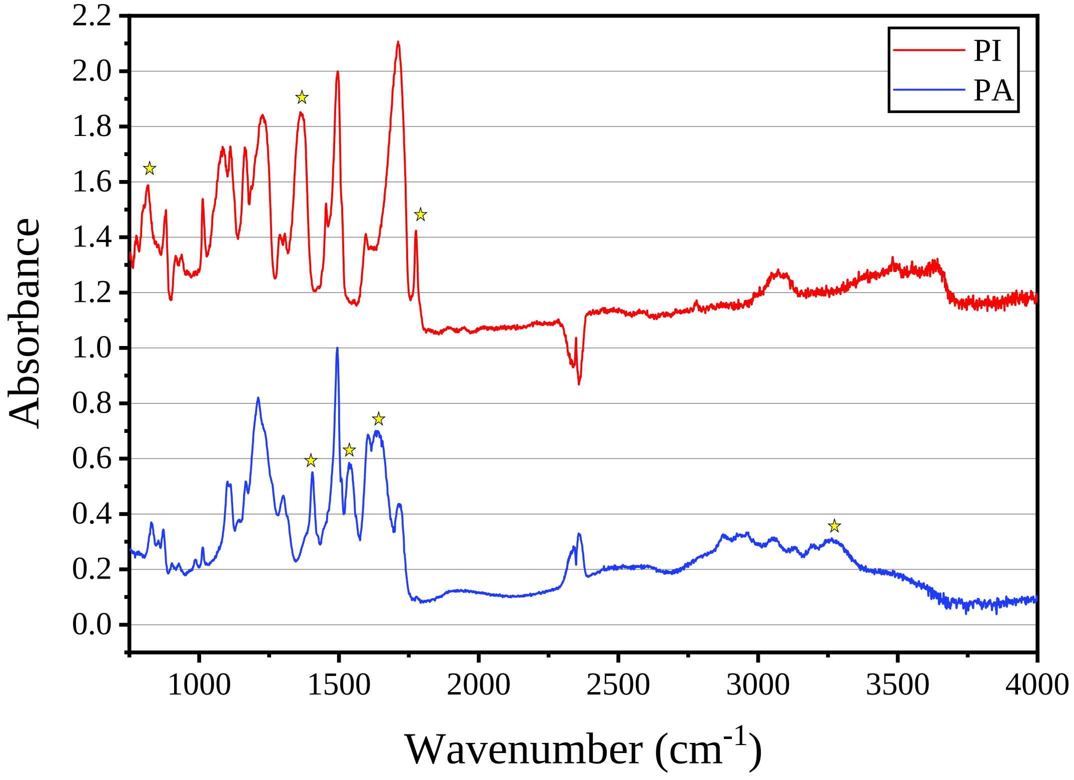

Note. Stars appear over signature peaks for direct comparison.

3.3.2 PMMA Validation

In the effort to synthesize PMMA in-house, a powder believed to be PMMA was synthesized, and its infrared spectra absorbance was collected. The spectrum of this sample is displayed in Figure 25. PMMA has a strong characteristic peak at ~1700-1750 cm^{-1} which is absent in this FTIR spectra graph [68]. A small peak exists near this range; however, this yields inconclusive results because the peak is too small to confirm the material as PMMA. These findings further confirm the difficulty of synthesizing PMMA in-house and validate the decision to purchase premade PMMA powders. More control over the synthesis process is necessary for this process to be valuable to this research. The ease of material preparation through pre-purchased powders, however, makes further efforts into PMMA synthesis impractical.

Figure 25

FTIR Spectrum of Attempted PMMA Synthesis with a Circle over the Characteristic Peak of PMMA

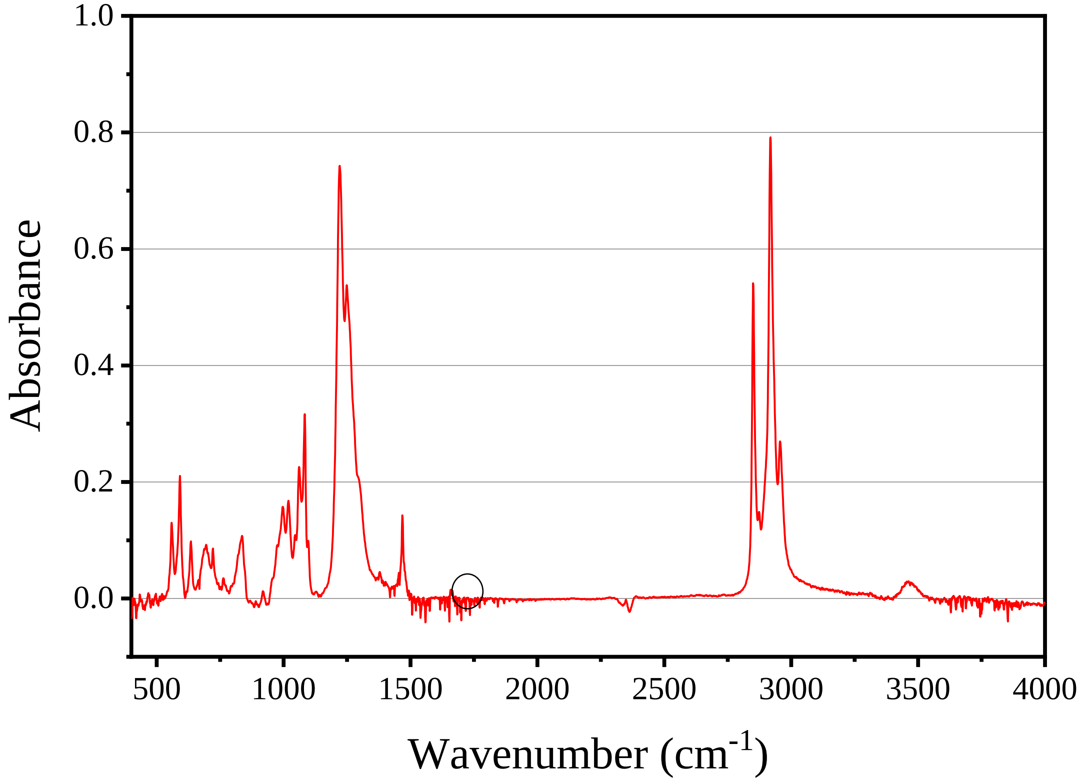

3.3.3 Low Temperature Imidization Attempts

The three attempts at low temperature imidization were all inspected with FTIR to examine if imidization took place. Samples from experiments utilizing thionyl chloride as a chemical catalyst, UV light exposure during curing, and DMF/CaCl to catalyze imidization were synthesized and compared with pure PA control samples. The collected spectra for all three experiments are presented in Figure 26. The spectra from both UV curing and DMF/CaCl yielded similar results with no noticeable change in the characteristic peaks of PA. UV curing and DMF/CaCl were therefore determined to be ineffective in inducing low temperature imidization. UV curing would require the addition of photo-initiators to make its use feasible; which has yet to be explored [69]. DMF/CaCl would also require the synthesis of PAA in-house and would require considerable work to develop a reliable synthesis method.

Figure 26

FTIR Spectra of (A) Thionyl Chloride, (B) UV Curing, and (C) DMF+CaCl Low Temperature Imidization Experiments

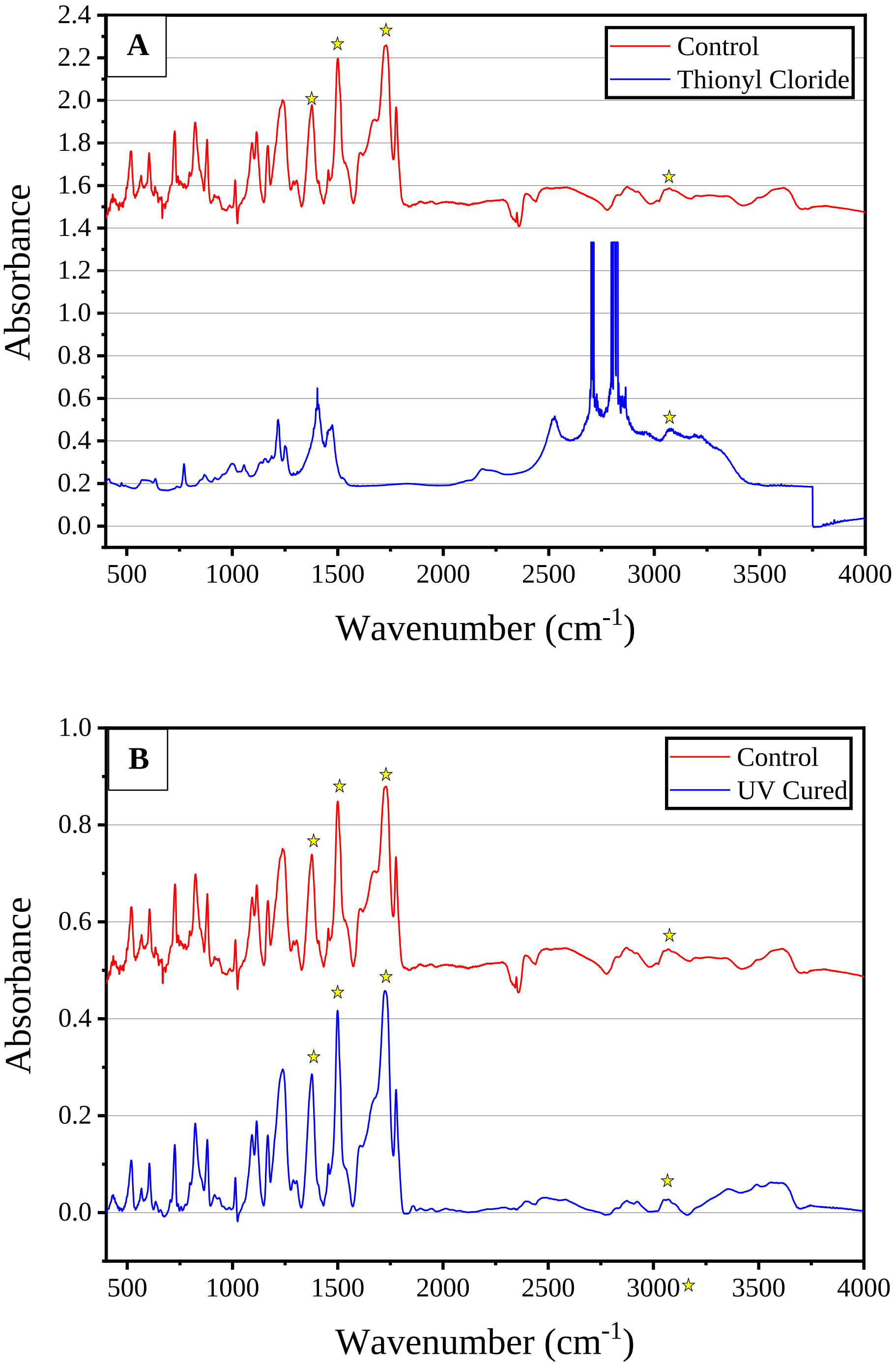

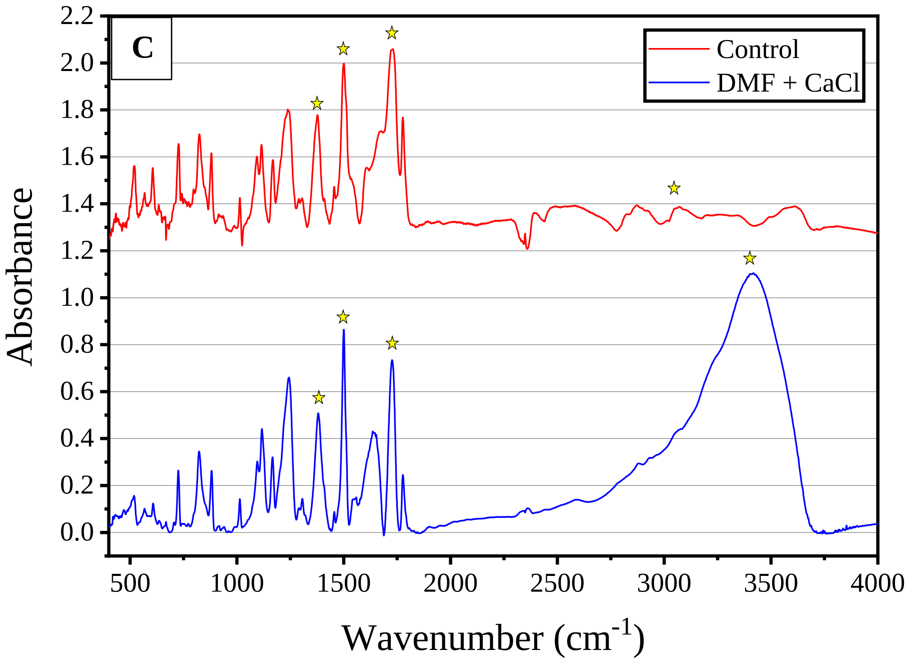

Note. The signature peaks of PA are highlighted with stars above peaks at 1399, 1538, ~1630, and ~2500-3500 cm^{-1}.

The thionyl chloride experiment yielded a sample that was a mixture of multiple materials. Many of the signature peaks of PI and PA are missing but a peak at ~3000-3500 cm^{-1} still exists. The existence of this peak implies imidization had not taken place. Adding thionyl chloride to PAA also resulted in an uncontrollable and volatile reaction that was exothermic and produced both chlorine gas and gaseous HCl. Once the reaction finished, a completely black mixture of liquid and solids was formed. This new material was difficult to spin coat and prepare into a thin film. The uncontrollable nature of this reaction, safety concerns, and lack of imidization evidence led to the abandonment of thionyl chloride as an imidization catalyst.

3.4 Dielectric Breakdown Testing

The dielectric strength of a material is determined by its ultimate breakdown strength and its thickness. Dielectric breakdown occurs in materials when the voltage across them is large enough to induce material failure, allowing current to pass through the material in the form of a hole. Multiple modes of dielectric breakdown are possible. Two of the most common modes are intrinsic and ionization (or avalanche) breakdown mechanisms [70, 71]. Intrinsic breakdown involves the excitation of electrons to higher energy states. Energy band structures are used to describe the energy states of charges in a material, with the valence and conduction bands being the most important to intrinsic breakdown. The valence band describes the highest energy level of unexcited electrons, and the conduction band is composed of the lowest energy states charges can occupy once excited. Under a sufficiently strong electric field, a large number of electrons from the valance band enter the conduction band, resulting in dielectric breakdown [72].

Avalanche breakdown functions similarly to intrinsic breakdown where electrons under strong electric fields enter the conduction band. Mobile charges in the conduction band are then able to accelerate and collide with stationary electrons in the valance band. Collisions between mobile and stationary charges cause some of the mobile charges' kinetic energy to be shared, ionizing the stationary charges. Once ionized, stationary charges become mobile, starting a chain reaction of collisions. The process continues with the number of mobile electrons growing exponentially until an "avalanche" point is achieved and breakdown occurs [72]. Avalanche breakdown is impacted mostly by electric field strength, mean free path of electrons, and the electrons' acceleration.

3.4.1 Room Temperature Testing

Dielectric breakdown testing is conducted on thin films at both room (300 K) and cryogenic (92 K) temperatures. Testing at room temperature was facilitated through the ASTM-D3755 standard Section 4. ASTM-D3755 details breakdown testing in which a thin film is sandwiched between two electrodes with a 50 g mass on top to ensure good contact. A fixture was 3-D printed which allowed for ease of testing to abide by this standard. The fixture, shown in Figure 27, houses two cylindrical brass electrodes 6.35 mm in diameter. The top cap is designed to be 50 g and uses four pins in the bottom of the fixture as a rail system for repeatable contact. Prior to room temperature breakdown testing, 1.5 cm × 1.5 cm squares are cut out of the composite thin films and placed between the electrodes. The electrodes are also polished with acetone to ensure their surfaces are free of debris. A Vitrek 955i high-potential (hipot) tester was utilized to conduct testing. A hipot lead was attached to the top electrode and a return lead was attached to the bottom electrode. The voltage across the electrodes was then ramped up by 500 V/s until a 50 mA current was read through the return wire, indicating dielectric breakdown took place. Often, an audible pop sound also followed the breakdown, which served as a nominal metric of a successful test. After each test, the 955i read out the voltage at the moment of breakdown. Thickness measurements were collected using a Mitutoyo digital micrometer near breakdown holes for accurate measurement of the thickness at the point of breakdown. Breakdown voltages were normalized by film thickness to determine the dielectric strength, which is later used for comparison between all tested samples.

Figure 27

Diagram of the Room Temperature Breakdown Fixture and Electrode Contact

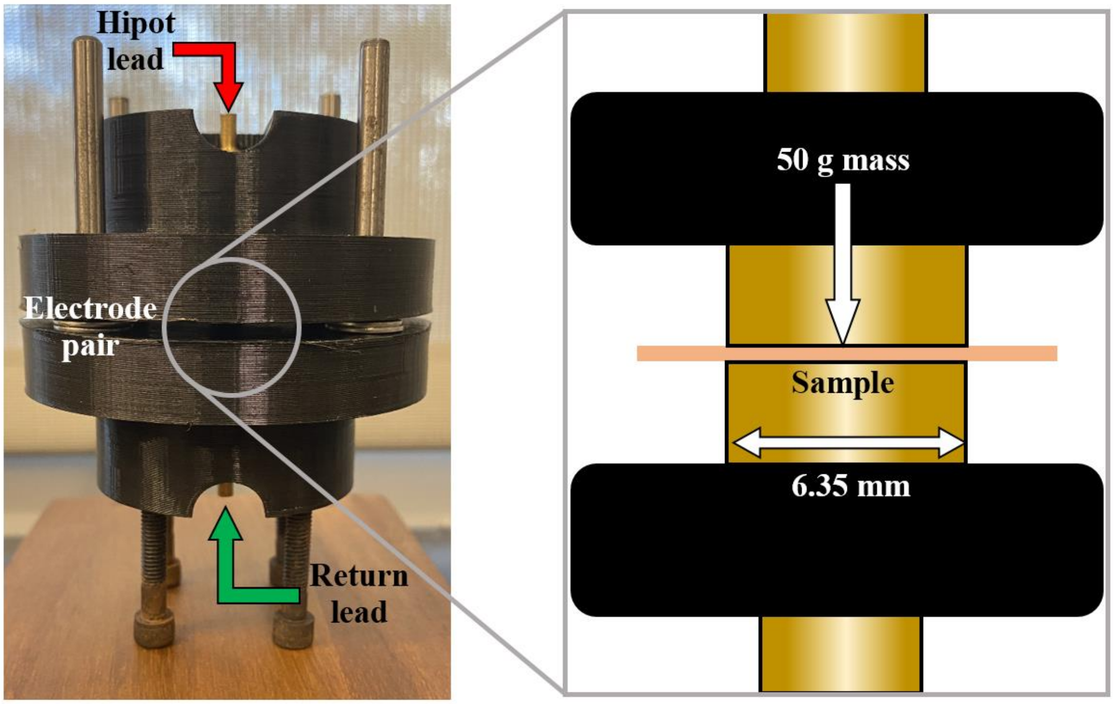

3.4.2 Cryogenic Temperature Testing

Cryogenic breakdown testing was conducted at 92 K through the use of liquid nitrogen (LN_2) inside of an LN_2 dewar. 92 K represents the steady state temperature achievable in the LN_2 dewar without submerging the samples in LN_2. Testing at the HTS cable operating temperature of 55 K requires the completion of the cryogenic testing chamber currently being manufactured. The details of this system will be discussed in Chapter 5. To conduct testing, a custom fixture, depicted in Figure 28, was fabricated to be lowered into the LN_2 dewar. Reaching 92 K was a time intensive process, so increasing the number of tests conducted per cool down cycle was necessary to increase efficiency. To accomplish this, the custom fixture features four sets of stainless steel electrodes with identical geometries to those of room temperature testing. Stainless steel was chosen as the electrode material over brass due to stainless steel's reduced contraction at cryogenic temperatures, which allowed for more repeatable testing. The electrodes were sheathed in Teflon to reduce the risk of arcing around thin film samples during testing. A 3-D printed holder was used to both house the four electrode pairs and limit their motion to maintain good contact between the electrode pairs. The holder was affixed to a wooden shaft, allowing the fixture to be suspended within the LN_2 dewar. Individual threaded wires were attached to the top of each electrode pair for the hipot tester to clip onto. The return wires were soldered to the bottom of each pair; they were all connected together and produced one return lead.

Figure 28

Zoomed in View of the Cryogenic Breakdown Fixture

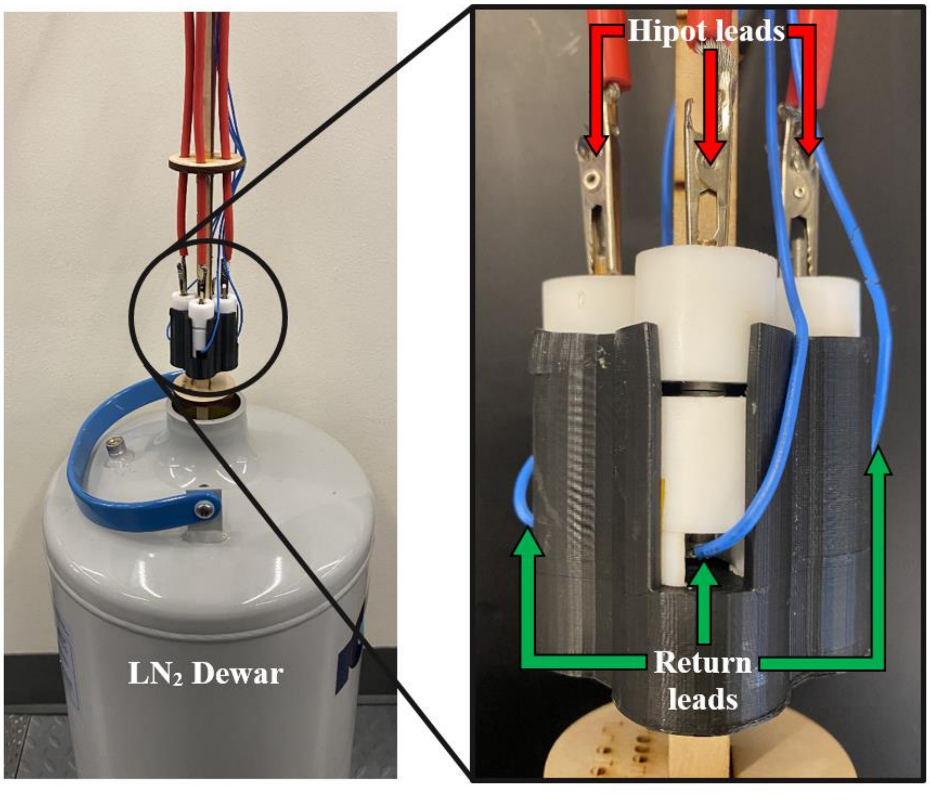

When conducting testing, a sheathed type K thermocouple was placed at the height of the electrode pairs to monitor temperature. The fixture was manually lowered into the dewar and affixed with a clamp, such that the bottom of the 3-D printed holder sat at the surface of the liquid nitrogen as gaseous nitrogen cooled the fixture. When 92 K was reached in 20-30 min, the 955i tester was connected to one of the threaded wires at the top of an electrode pair and the collective return lead. The voltage was increased at the same rate as room temperature testing until breakdown was achieved. After each test, the hipot lead was connected to the next electrode pair until all four tests were conducted. Thickness measurements, to normalize the breakdown voltages, were collected identically to room temperature testing. The results of dielectric breakdown testing will be discussed in Chapter 4.

Chapter 4

Material Characterization Results

4.1 Nanoparticle Dispersion

SEM images of each nanocomposite configuration were assessed for characterization of the nanoparticle sizes and dispersions. To classify as a nanoparticle, a particle must be less than 100 nm in diameter. This is desirable because particles under the 100 nm threshold allow for enhanced mechanical properties when compared to that of microparticles that exceed the threshold [73]. To examine the particle sizes, images were imported into a Python script which inspected both the number and the size of particles. The script employed computer vision to place boxes around nanoparticles for thickness estimations. SEM images of 4% filler concentration samples of all nanocomposite configurations and their histograms are displayed in Figure 29. The images utilized for analysis of each composite configuration are also included for reference in Figure 29. Estimating nanoparticle size through this script has clear limitations due to the difference in brightness and contrast of the particles in the image. Particles without clear boundaries or that exist deeper in the material appear darker, causing only the most visible particles to be captured with the script. This also led to the PA sample being imaged at 12,000× magnification while the PI and PMMA samples were imaged at 8,000× magnification. In spite of these limitations, the script still offers an adequate method for particle analysis and for conclusions to be drawn about nanoparticle sizes and dispersions.

Figure 29

SEM Images and Histograms of 4% Composite Samples of (A) PI, (B) PA, and (C) PMMA

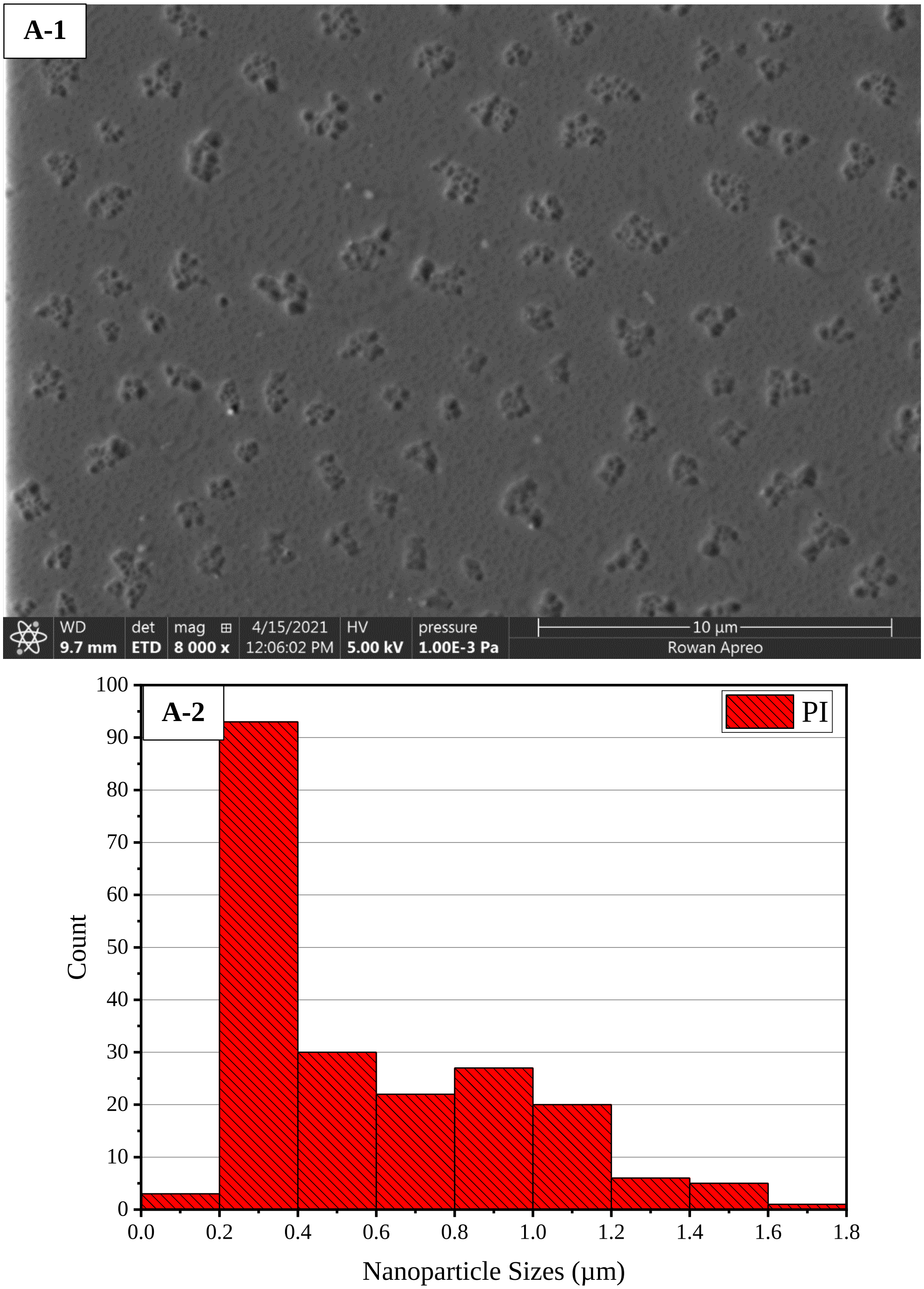

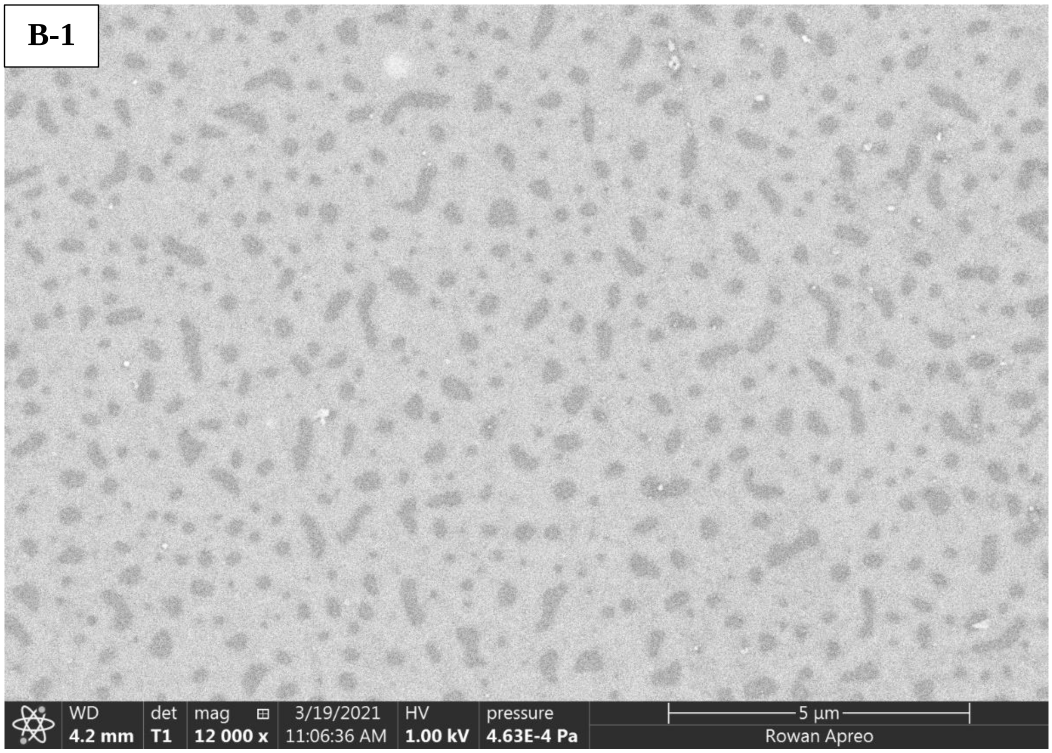
B-1
WD
4.2 mm
det
T1
mag
12 000 x
3/19/2021
11:06:36 AM
HV
1.00 kV
pressure
4.63E-4 Pa
5 µm
Rowan Apreo

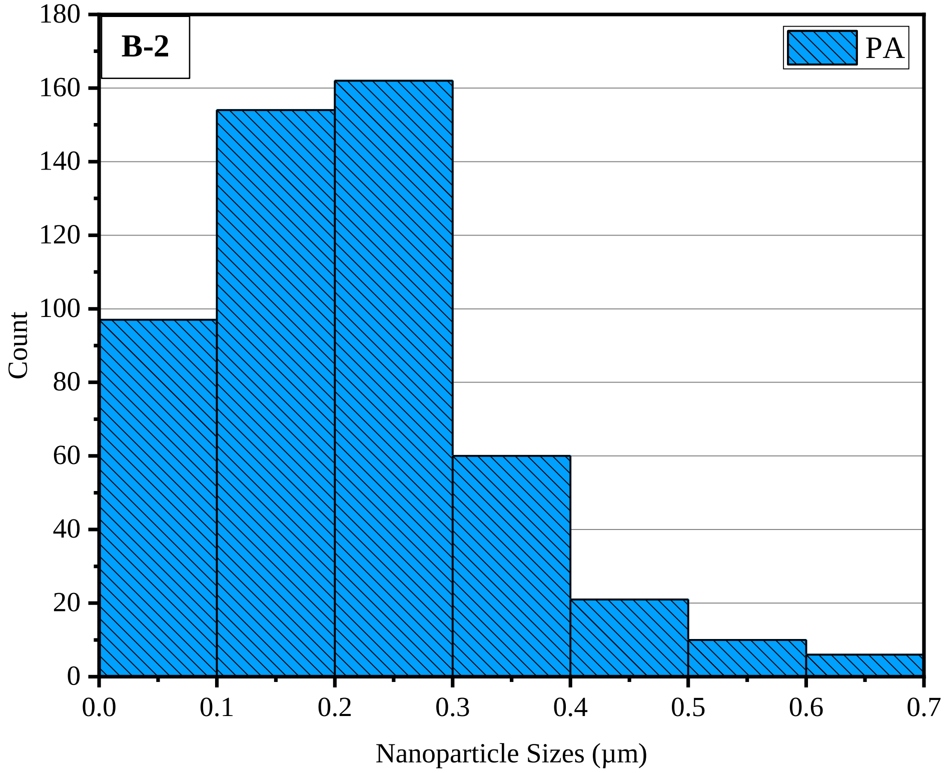
B-2
PA
Count
180
160
140
120
100
80
60
40
20
0
0.0
0.1
0.2
0.3
0.4
0.5
0.6
0.7
Nanoparticle Sizes (µm)

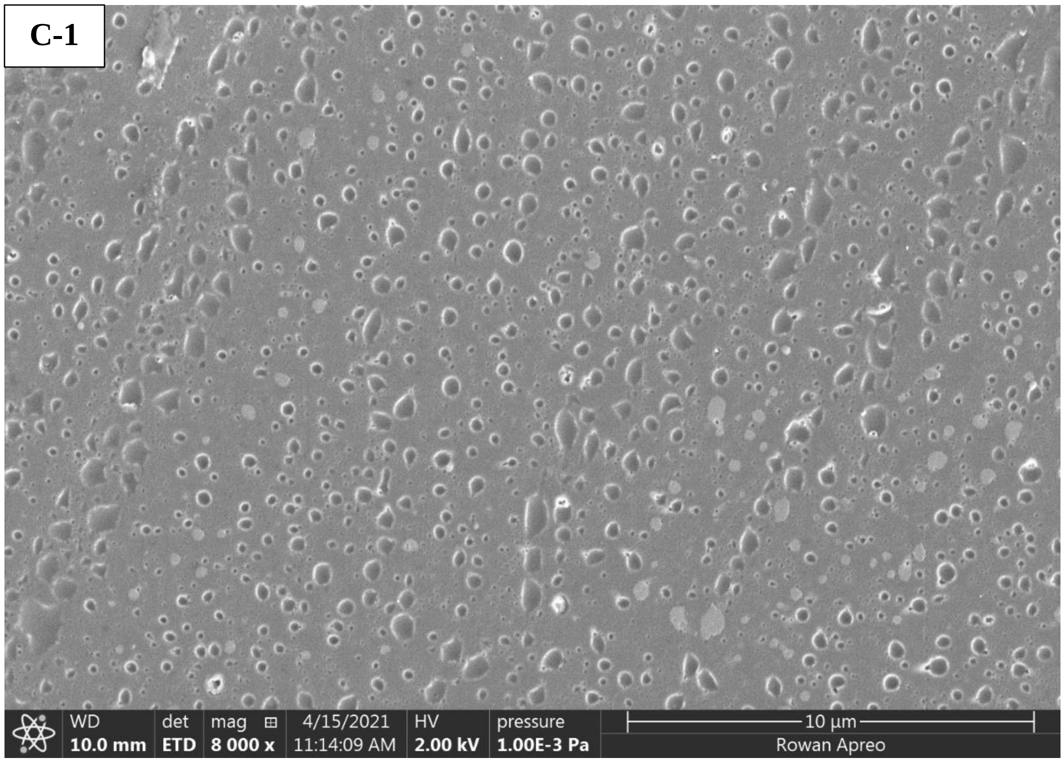
C-1
WD
10.0 mm
det
ETD
mag
8 000 x
4/15/2021
11:14:09 AM
HV
2.00 kV
pressure
1.00E-3 Pa
10 µm
Rowan Apreo

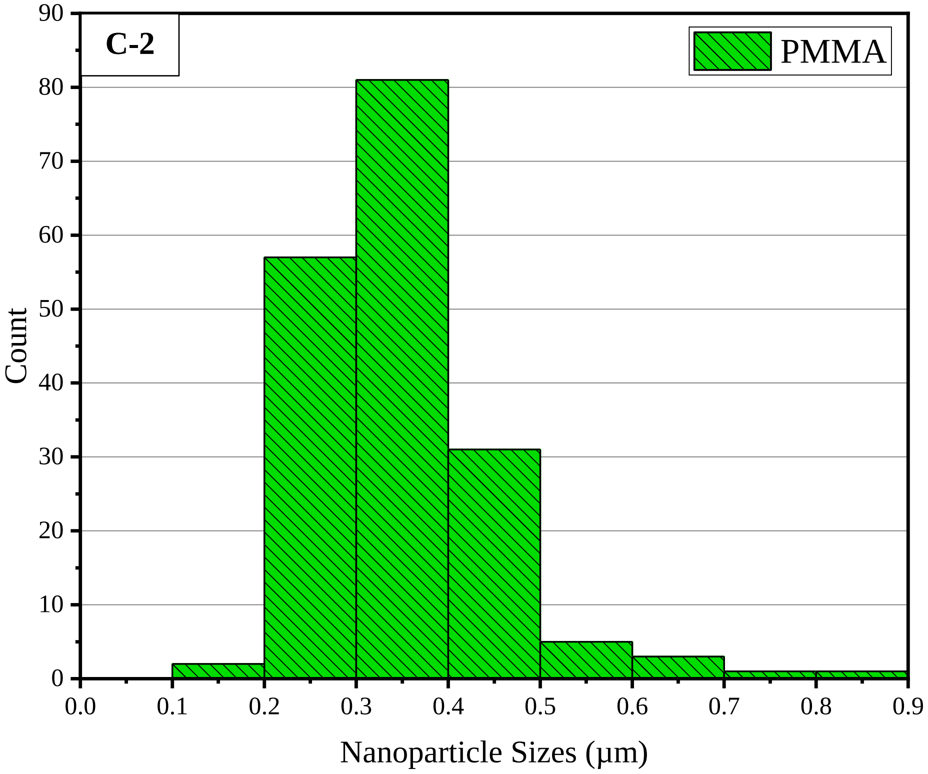
C-2
PMMA
Count
Nanoparticle Sizes (µm)
0
10
20
30
40
50
60
70
80
90
0.0
0.1
0.2
0.3
0.4
0.5
0.6
0.7
0.8
0.9

PA samples displayed a superior average nanoparticle size and dispersion to that of the three host matrices. At 12,000× magnification, 510 particles were measured, and found to have an average diameter of 209.8 nm. The bulk of the nanoparticles were within the range of 0 to 300 nm, with little spread outside of this range. The nanoparticles were also evenly spread out and dispersed, leaving no obvious agglomerations that can become weak points in the material. However, PI and PMMA samples displayed larger average particle sizes and poorer dispersions. PI samples were the most deficient with 207 particles captured and an average diameter of 578.0 nm. Most of these particles were within the range of 200 to 400 nm but the overall sizes ranged from 0 to 1800 nm. It is also clear in Figure 29A-1, small agglomerations of individual particles were formed, increasing the average diameter. Upon inspection, a large number of much smaller nanoparticles were also present outside these agglomerations. These smaller nanoparticles lacked obvious boundaries which prevent them from being detected by the script, leading to a further skew of the data. The PMMA sample displayed similar agglomerations to PI with 181 particles captured and an average diameter of 344.7 nm. Most of the particles were in the range of 200 to 400 nm with less spread from this range when compared to PI. The smallest nanoparticles still lacked enough contrast to be detected by the script, increasing the apparent average diameter.

While the limitations of the Python script skewed the data for PI and PMMA samples, the surface morphologies that resulted from large nanoparticles, nanoparticle agglomerations, and visible microparticles provided critical information on the sample quality. A large quantity of silica nanoparticles existed in both materials and made up a rough majority of the total volume of the silica in each composite. However, the most visible particles in both PI and PMMA existed outside the range of nanoparticles and made up a considerable fraction of the total silica. The notable volume of silica as microparticles helped indicate the need for increased control during nanoparticle generation.

Further control and analysis into the Stöber process and *in situ* fabrication is currently being explored to decrease both average particle size and agglomerations. These efforts focus on mixing times of the sol gel before and after its introduction into the polymer host and heating the sol gel while mixing. The preliminary results of these efforts have shown large agglomerations of nanoparticles (>50 µm) form due to heating. Increased heating from PI's curing temperatures and the reduction of the PMMA precursor are suspected to be the cause of the increased particle sizes and agglomerations in these materials compared to PA.

4.2 Dielectric Breakdown of Polyimide

Dielectric breakdown testing was conducted on PI-SiO_2, PA-SiO_2, and PMMA-SiO_2 composites at both room (300 K) and cryogenic (92 K) temperatures. Samples with silica concentrations of 0, 2, 4, and 6% were tested with 5 data points at each temperature. The performance of PI samples at both temperatures is showcased in Figure 30. In this figure, the mean values of each data set are reported with one standard deviation error bars. Further statistical analysis was conducted on the breakdown data through a Weibull cumulative distribution function. Weibull distributions were selected to conform with common practices within the field of polymer nanocomposite dielectric breakdown analysis [74]. The Weibull distributions were constructed to compare breakdown strength and the probability of breakdown. All distributions were prepared to include individual breakdown data points and a trend line for ease of comparison between data sets. The scale parameter (α) was set as the 63.2% breakdown probability value and the shape parameter (β) was generated accordingly for all concentration data sets. The resulting Weibull distributions for all concentrations of PI-SiO_2 samples at both room and cryogenic temperatures are shown in Figures 31 and 32, respectively. The scale and shape parameters for these distributions are summarized in Table 4. These parameters function to best prepare the Weibull distributions by the scale parameter stretching and compressing the overall distributions and the shape parameter setting the distributions' slopes.

Figure 30

Average Dielectric Breakdown Performance of PI Based Samples at Room (300 K) and Cryogenic (92 K) Temperatures

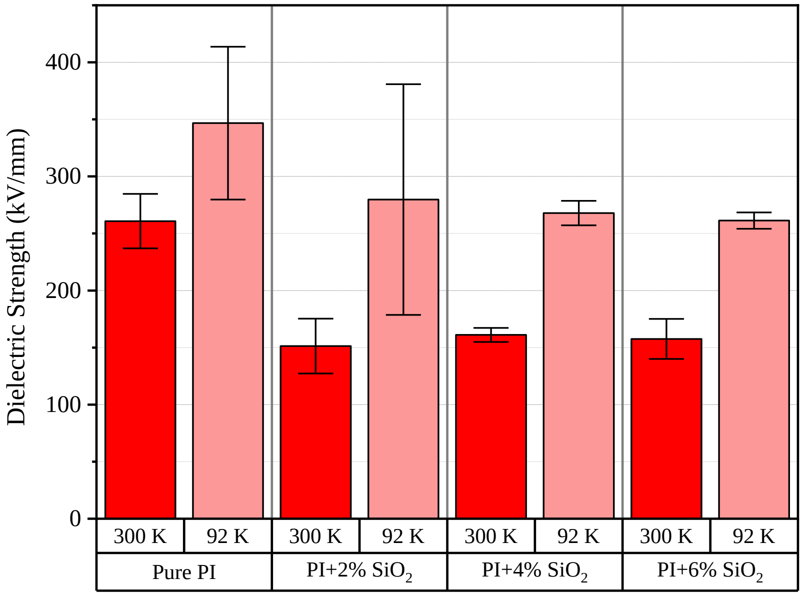

Figure 31

Weibull Distributions for Room Temperature Breakdown Testing of 0-6% PI-SiO₂ Nanocomposites

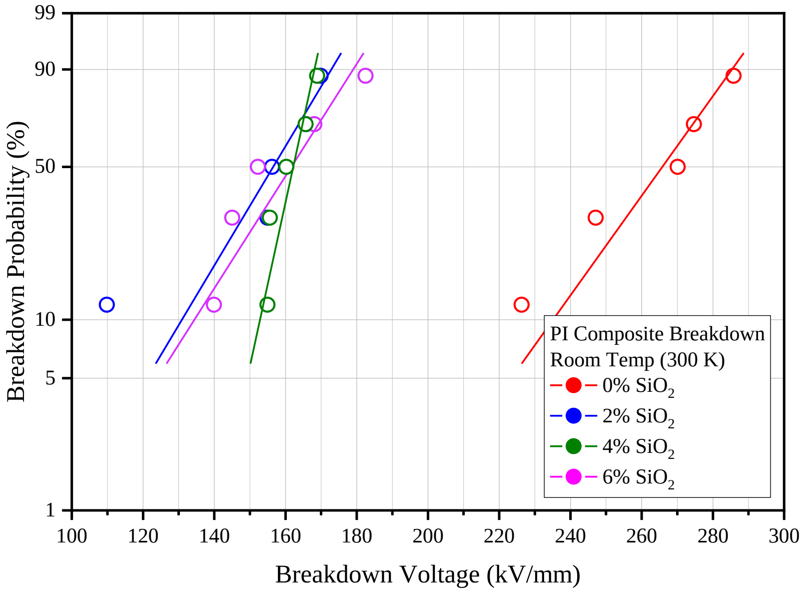

Figure 32

Weibull Distributions for Cryogenic Temperature Breakdown Testing of 0-6% PI-SiO₂ Nanocomposites

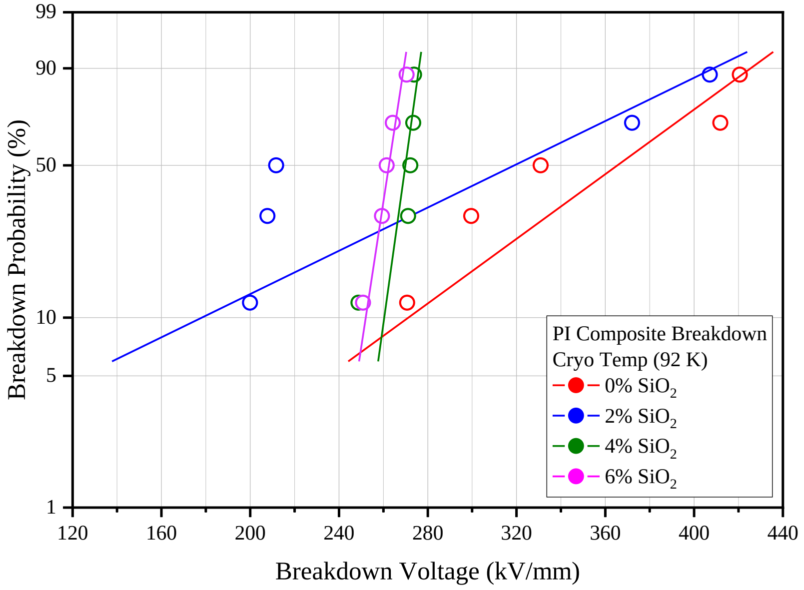

Table 4

Weibull Scale and Shape Parameters for 0-6% PI-SiO₂ Concentration Distributions at Room (300 K) and Cryogenic (92 K) Temperatures

Sample Type	**300 K**		**92 K**	
	Scale Parameter (α)	Shape Parameter (β)	Scale Parameter (α)	Shape Parameter (β)
Pure PI	270.26243	15.73062	372.3931	6.61275
2% PI-SiO_2	159.66833	10.88416	312.60121	3.40525
4% PI-SiO_2	163.77443	32.13374	271.64132	52.91019
6% PI-SiO_2	164.92245	10.55739	264.35949	46.75706

At room temperature, the pure polymer matrix material outperforms its nanocomposites, with pure PI displaying an average dielectric strength of 260.8 kV/mm. The introduction of nanoparticles into the host results in a drop in dielectric strength with a similar performance across all filler concentrations. An average breakdown strength of 2-6% silica concentrations range between 151.3-161.1 kV/mm for the dataset. The error bars between these averages overlap, further affirming the statistically insignificant difference between their breakdown strengths. The room temperature Weibull distributions display similar findings with overlapping fit lines and data points for composite samples. All samples also display fit lines with steep slopes, signifying precise data sets with tight groupings. At cryogenic temperature, however, all concentrations experience a significant increase in average strength. Pure PI broke down at an average value of 346.7 kV/mm. PI's composites also experienced a similar drop in strength seen in room temperature testing but performed comparably better than pure PI at room temperature. The composites' breakdown strength at cryogenic temperature ranged from 261.3-279.7 kV/mm with overlapping error bars. The Weibull distributions highlight the large variations for the pure and 2% samples with shallow slopes on their fit lines. The 4% and 6% samples display more precise data compared to the pure and 2% samples with much steeper slopes on their respective fit lines and slight overlap between data points.

After testing, breakdown holes of each sample are inspected with scanning electron microscopy. The difference in temperature for dielectric breakdown also results in variations to the breakdown holes. Figure 33 compares the breakdown holes of 4% PI samples broken down at either temperature. At both temperatures, a wide damaged area around the breakdown hole is displayed. Room temperature breakdown yields a larger through hole compared to cryogenic breakdown testing. Cryogenic testing also leaves more material behind after breakdown. The difference in breakdown holes is suspected to be caused by heat generation during breakdown. As dielectric breakdown testing is conducted, the material stores energy in the form of heat which can exceed the glass transition temperature of the polymer. Once the glass transition temperature is reached, localized melting can occur between the electrodes and leave large amorphous areas [75]. Evidence of these amorphous areas can be seen around the through hole in the room temperature sample. The smaller hole in cryogenic temperature testing results from the colder environment, which inhibits the glass transition temperature from being as easily achieved. The colder environment also offers better heat dissipation, further inhibiting the chance of hitting the glass transition temperature. These two factors allow breakdown to occur at cryogenic temperatures while the polymer remains a solid [76]. Localized melting still occurred at 92 K, although a majority of the material in the hole remained a solid, causing the visibly smaller through hole.

Figure 33

SEM Images of Dielectric Breakdown Holes for 4% PI-SiO_2 Samples at Room (left) and Cryogenic (right) Temperatures

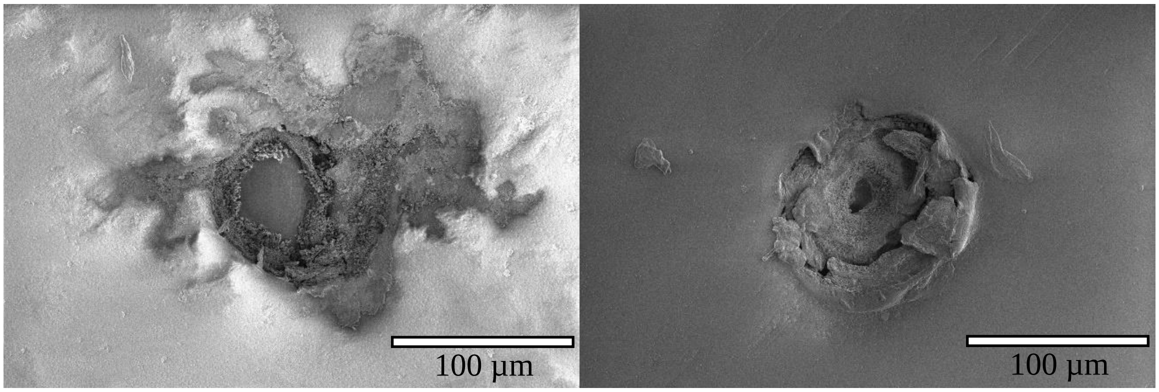

4.3 Dielectric Breakdown of Polyamide

The results of breakdown testing for PA based samples is summarized in Figure 34, where the mean values of dielectric breakdown and standard deviation error bars are presented. Weibull distributions were also generated with the scale parameter (α) being set as the 63.2% breakdown probability value, similar to that of PI based samples. The Weibull distributions for room and cryogenic breakdown data are displayed in Figures 35 and 36 respectively. The accompanying Weibull parameters for Figures 35 and 36 are summarized in Table 5.

Figure 34

Average Dielectric Breakdown Performance of PA Based Samples at Room (300 K) and Cryogenic (92 K) Temperatures

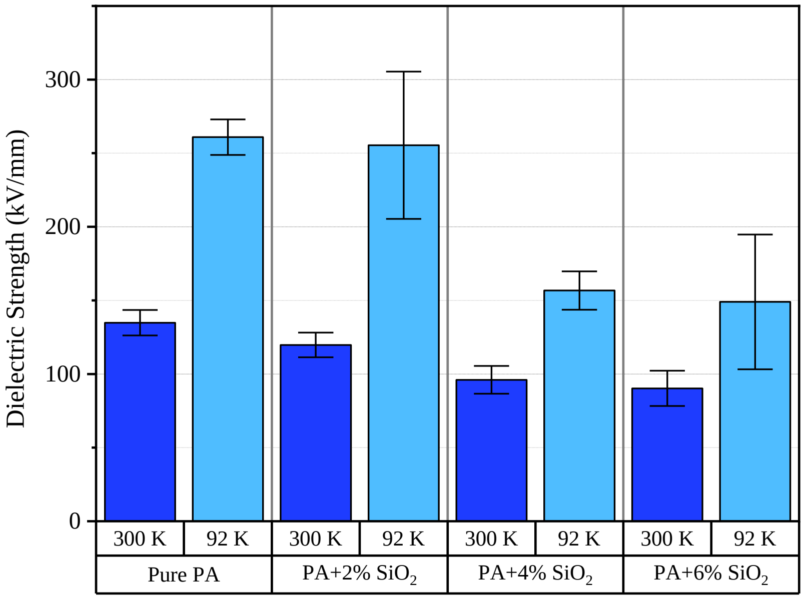

Figure 35

Weibull Distributions for Room Temperature Breakdown Testing of 0-6% PA-SiO$_2$ Nanocomposites

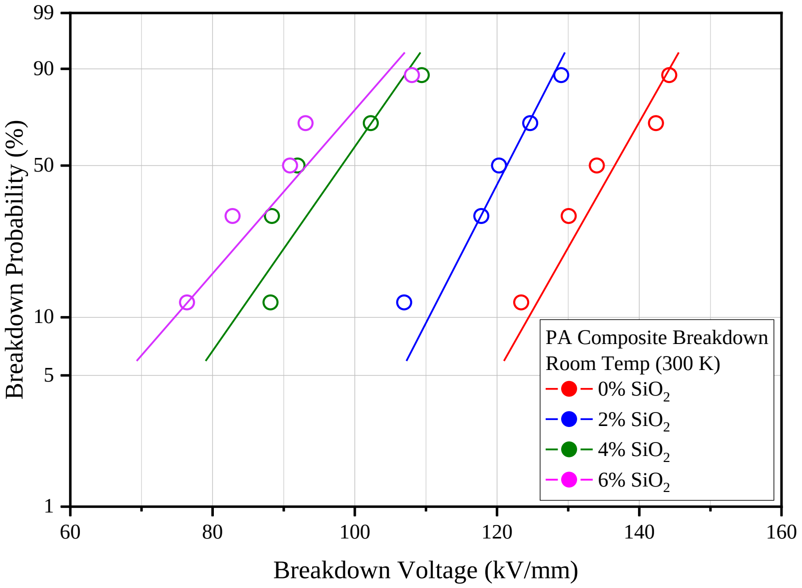

Figure 36

Weibull Distributions for Cryogenic Temperature Breakdown Testing of 0-6% PA-SiO₂ Nanocomposites

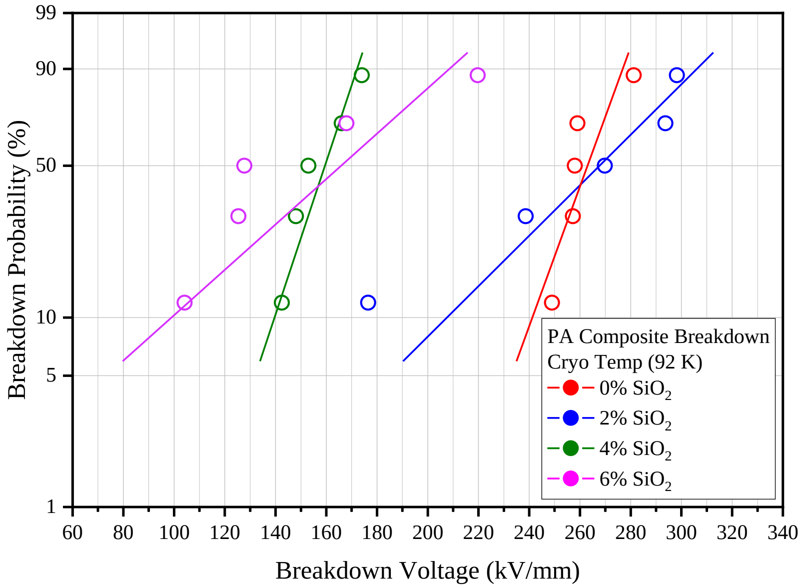

Table 5

Weibull Scale and Shape Parameters for 0-6% PA-SiO₂ Concentration Distributions at Room (300 K) and Cryogenic (92 K) Temperatures

Sample Type	**300 K**		**92 K**	
	Scale Parameter (α)	Shape Parameter (β)	Scale Parameter (α)	Shape Parameter (β)
Pure PA	138.43423	20.70569	266.46313	22.17637
2% PA-SiO2	123.08455	20.27889	273.24274	7.70966
4% PA-SiO2	100.05612	11.82812	162.27209	14.52863
6% PA-SiO2	95.15065	8.81577	164.73432	3.84465

PA is a dielectrically weaker polymer compared to PI and exhibits lower dielectric strength values for all concentrations. At room temperature pure PA breaks down at an average value of 134.8 kV/mm. A slight decreasing trend in dielectric strength in room temperature data is observed as filler concentration increases. The PA composites at room temperature exhibit strength values between 90.3-119.8 kV/mm. The Weibull distributions all display similar shaped distributions and fit lines with similar slopes, implying equally precise data sets. PA-SiO_2 composites experience a large increase in dielectric strength at 92 K compared to room temperature testing. The pure polymer and 2% filler concentration nearly double in strength from room temperature testing with average dielectric breakdown values of 260.9 and 255.4 kV/mm, respectively. The 4% and 6% samples experience more moderate increases of about 1.5× from their room temperature values. The average strength value for 4% is 156.7 kV/mm compared to 6% samples displaying a mean value of 149.0 kV/mm. Significant overlap between error bars is also present between the pure PA and 2% samples as well as between the 4% and 6% samples, implying their differences are insignificant. Weibull distributions of the cryogenic breakdown data show overlapping fit lines and data sets for these two concentration pairs. The pure and 4% samples display more precise data than the 2% and 6% samples with similarly steep slopes.

Breakdown holes of 4% PA-SiO_2 samples were inspected with scanning electron microscopy and compared in Figure 37. The breakdown hole for room temperature testing displays a medium sized through hole with little damage around the breakdown point. The cryogenic breakdown hole, however, displays a significantly larger hole with more damage around breakdown. In both cases, heating from testing was able to deform and melt the composite. The glass transition temperature of PA is 55 °C, which is much lower than that of PI’s of 321 °C [77, 78]. This lower value makes achieving the glass transition temperature more attainable in both testing environments.

Figure 37

SEM Images of Dielectric Breakdown Holes for 4% PA-SiO$_2$ *Samples at Room (left) and Cryogenic (right) Temperatures*

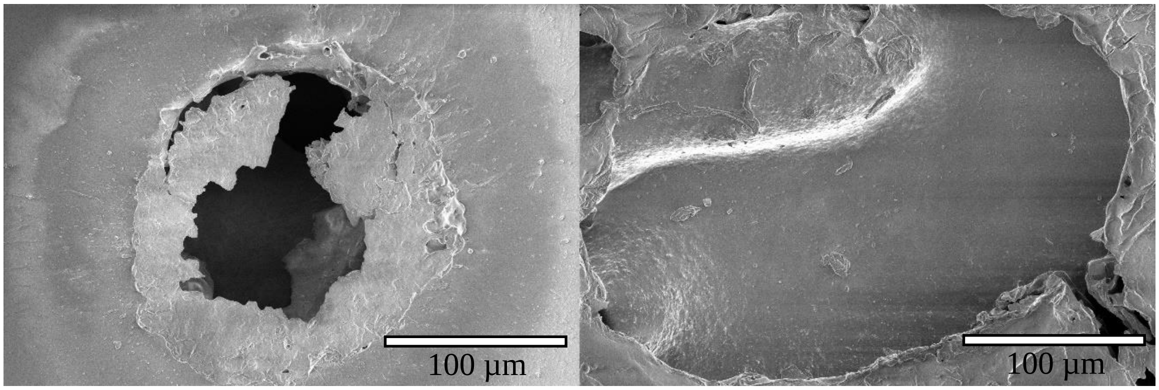

4.4 Dielectric Breakdown of PMMA

The performance of PMMA based samples is compiled identically to that of PI and PA based materials. A graph of mean breakdown values is displayed in Figure 38. The accompanying room and cryogenic temperature Weibull distributions are plotted in Figures 39 and 40, respectively. The parameters used to construct the Weibull distributions are tabulated in Table 6.

Figure 38

Average Dielectric Breakdown Performance of PMMA Based Samples at Room (300 K) and Cryogenic (92 K) Temperatures

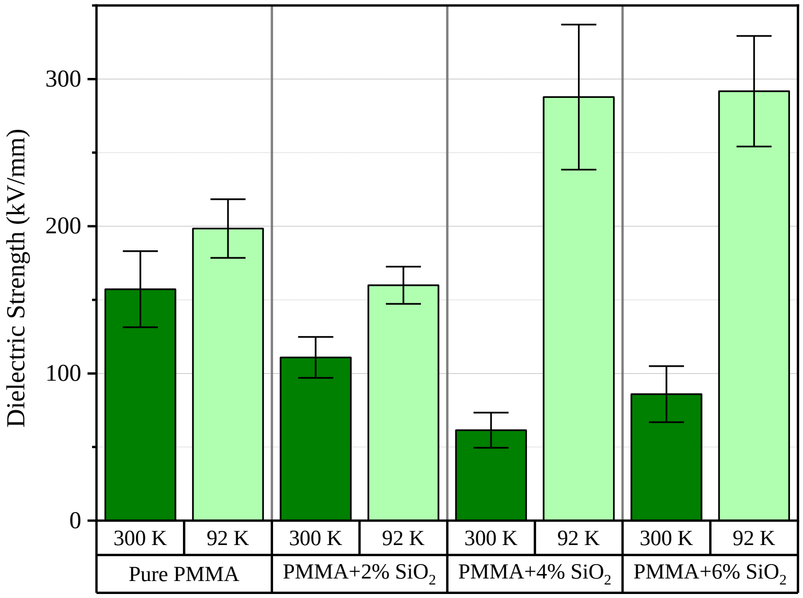

Figure 39

Weibull Distributions for Room Temperature Breakdown Testing of 0-6% PMMA-SiO$_2$ Nanocomposites

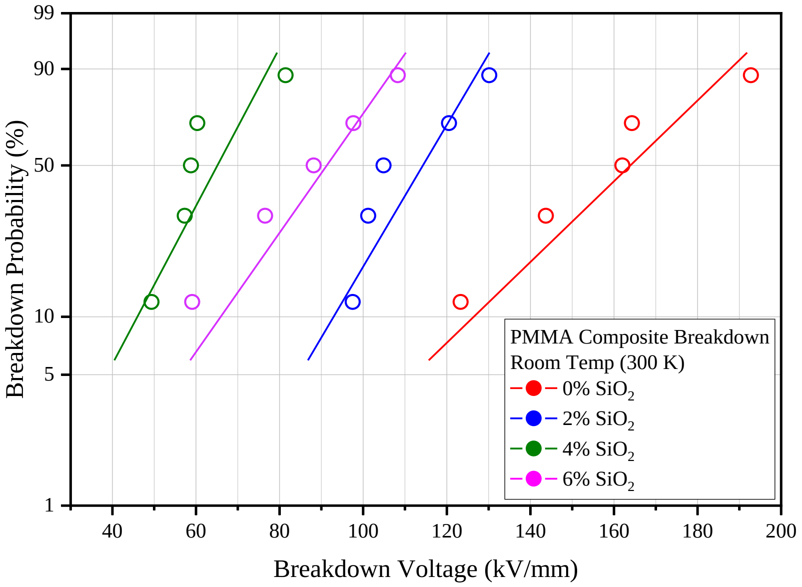

Figure 40

Weibull Distributions for Cryogenic Temperature Breakdown Testing of 0-6% PMMA-SiO_2 Nanocomposites

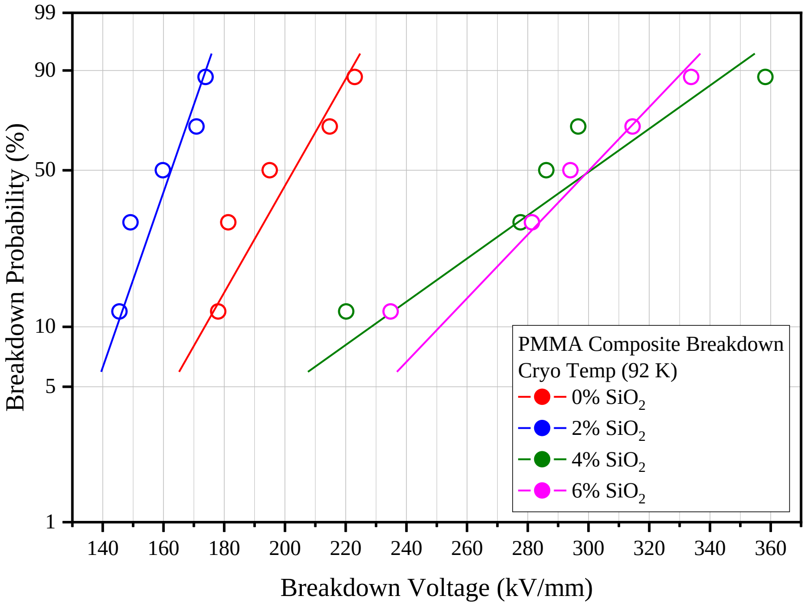

Table 6

Weibull Scale and Shape Parameters for 0-6% PMMA-SiO2 Concentration Distributions at Room (300 K) and Cryogenic (92 K) Temperatures

Sample Type	**300 K**		**92 K**	
	Scale Parameter (α)	Shape Parameter (β)	Scale Parameter (α)	Shape Parameter (β)
Pure PA	167.28394	7.56745	206.7548	12.4195
2% PA-SiO_2	116.63888	9.43217	165.14673	16.51614
4% PA-SiO_2	66.13628	5.67724	306.82755	7.14244
6% PA-SiO_2	92.87232	6.0621	306.17106	10.88053

PMMA is a polymer with a similar dielectric strength to PA and also displays similar performances at room temperature for all filler concentrations. Pure PMMA exhibits an average dielectric strength of 157.2 kV/mm. Its composites all demonstrate a drop in dielectric strength from the pure polymer with 4% having the lowest performance. PMMA-SiO_2 composites exhibit mean strength values between 61.5-110.9 kV/mm. Weibull distributions for room temperature data display similar trend lines and distributions for all concentrations. Cryogenic temperature data, however, demonstrates a significant increase in strength as filler concentration increases. The pure polymer performs slightly better at cryogenic temperature than room temperature, with an average dielectric strength of 198.4 kV/mm. A slight drop in strength from the pure polymer occurs at 2%, displaying a dielectric strength of 160.0 kV/mm. The 4% and 6% samples almost double their strength from the 2% samples. These higher concentrations exhibit mean strength values of 287.8 and 291.7 kV/mm, respectively. Their mean values are also statistically insignificant as they share overlapping error bars. The higher concentration samples display larger variations in data points, as shown in the Weibull distributions for cryogenic data. Despite the greater variations, the 4% and 6% samples consistently perform better than the pure and 2% samples.

PMMA-SiO_2 samples with 4% filler concentrations were broken down at room and cryogenic temperatures, and were inspected with the SEM, as displayed in Figure 41. The breakdown holes at both temperatures exhibit similar geometries and sizes. The cryogenically broken down sample exhibits marginally more damage and more amorphous areas around the breakdown hole compared to the room temperature sample. Both samples also display signs of the glass transition temperature being reached, with material being completely removed from each through hole. The glass transition temperature of PMMA varies between 60 °C and 130 °C, corroborating the likelihood of localized melting occurring at 92 K [37, 39, 79].

Figure 41

SEM Images of Dielectric Breakdown Holes for 4% PMMA-SiO$_2$ Samples at Room (left) and Cryogenic (right) Temperatures

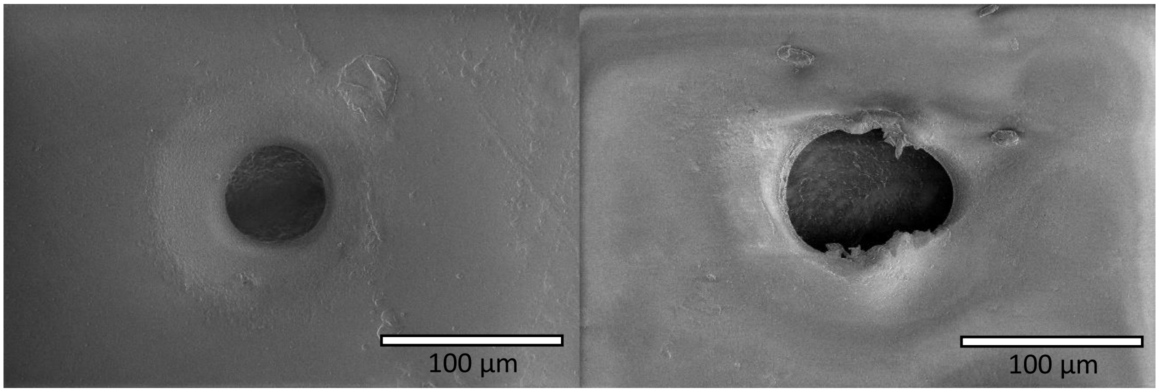

4.5 Expanded Model of Dielectric Breakdown Mechanisms

The breakdown data from the pure polymers and nanocomposites both demonstrate an increased dielectric strength when going from room to cryogenic temperature. For pure polymers, it is suspected that the improvement of dielectric strength at cryogenic temperatures is caused by their thermal contraction and the reduced number of free electrons. The free volumes in polymers directly affect the transport of charge carriers, and consequently the dielectric breakdown of polymers [80]. When a polymer is cooled, the free volumes are expected to decrease in both size and number, as some of them can collapse and disappear due to contraction, as shown in Figure 42 (top). As a result, the polymer becomes denser with smaller and fewer free volumes at the cryogenic temperature, leading to higher dielectric strength. Furthermore, the thermally excited charge carriers in a material are temperature dependent. The number of free electrons in a polymer can be significantly smaller in a cryogenic environment than at room temperature, affecting the material’s dielectric performance.

Figure 42

Temperature-Dependent Model Depicting the Impact of Temperature on (top) Pure Polymers and (bottom) Polymer Nanocomposites

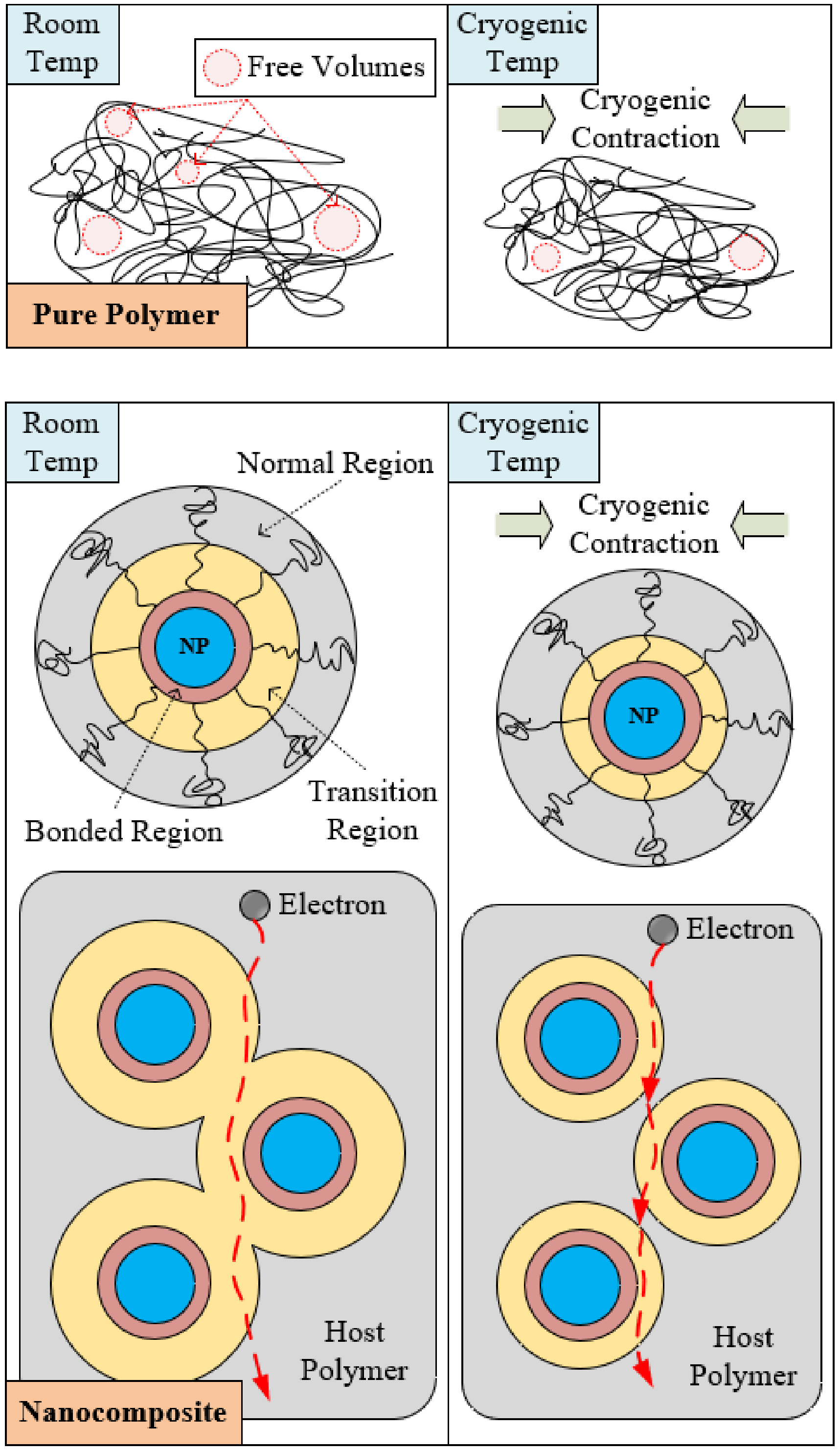

The dielectric behavior of nanocomposites at the cryogenic temperature can be explained from two main perspectives, first, as described earlier, by the performance improvement of the host polymer, and second, by a new temperature-dependent model modified from previously reported multi-core (by Tanaka) and potential barrier models (by Li *et al.*) [18, 46]. The filler silica has a very low thermal contraction rate of 0.05% (from 300 K to 4 K) [17]. As a result, the structural change of SiO_2 nanoparticles is negligible when analyzing the temperature-dependent interfacial change between the nanoparticles and the polymer. In a cryogenic environment, the molecular chains wrapped around the nanoparticle are tightened due to the polymer contraction, resulting in a reduced transition region. It is worth noting that the thermal contraction of a nanocomposite can be significantly lower than that of its host polymer [20-22]. This suggests that the local contraction around the transition region of the host polymer can be greater than the global contraction of the nanocomposites. Therefore, the initially overlapped transition regions around dispersed nanoparticles can break apart into separate regions, as illustrated in Figure 42 (bottom). According to the potential barrier model, this separation will create additional energy barriers around nanoparticles at the interface between the transition region and the surrounding host polymer, increasing the dielectric strength [18].

4.6 Discussion of All Composite Configurations

Of the three polymer nanocomposite configurations characterized in this study, PI-SiO_2 proved to be the superior dielectric for nearly all concentrations tested at both testing temperatures. The dielectric performance of PI-SiO_2 samples were only outperformed by PMMA-SiO_2 for 4% and 6% filler concentrations at 92 K, however the difference between their performances at this temperature is marginal (~20-30 kV/mm). PI-SiO_2 displayed impressive dielectric strengths despite displaying the largest average nanoparticle size (avg. size of 578 nm) and the poorest dispersions. This suggested that, with further control over nanoparticle size and dispersions, PI-SiO_2 would represent the ideal candidate for adoption as a gaseous helium cooled HTS cable dielectric. PI-SiO_2 was still unsuitable for use as HTS cables dielectrics due to its high processing temperature. The lack of an effective low temperature imidization process meant that the HTS cables in question would be destroyed before a PI-SiO_2 coating could be prepared.

PA-SiO_2 and PMMA-SiO_2 both perform comparably well in dielectric breakdown testing with PMMA-SiO_2 performing better at higher concentrations in the cryogenic environment. However, the difference in their performances is of little concern as both materials greatly outperform the 12 kV/mm dielectric requirement for use in HTS cables. Of the two, PA-SiO_2 displays a smaller average nanoparticle size and superior dispersion. The decreased nanoparticle size of PA-SiO_2 increases the likelihood of improved mechanical and thermomechanical properties, such as CTE, in the final material. PMMA-SiO_2 samples would require considerable experimentation into increasing the control over the sol gel process to overcome this deficit. Furthermore, PMMA is cured at 125 °C which is lower than the boiling point of DMF at 153 °C. This lower temperature is employed to avoid reaching the delamination temperature of the HTS cables. In order to remove the un-vaporized DMF in the material at 125 °C, a vacuum environment would be required. Therefore, the larger average nanoparticle size of PMMA-SiO_2 and the unknown effect of the un-vaporized DMF has on its mechanical properties make PA-SiO_2 the superior candidate as an HTS cable dielectric. Further CTE testing at 55 K is required to confirm this recommendation prior to adoption into HTS cables.

Chapter 5

Material Validation Apparatuses

5.1 Wire Coating

Further material testing is required to validate the polymer nanocomposite's use as a dielectric layer in gaseous helium cooled HTS cables. Testing up to this point has focused on thin film samples, but the nanocomposite's end use as a cable coating requires testing of the dielectric on a cable or cable analog. The HTS cables in question can be manufactured at various lengths but are generally fabricated in 50-100 m sections. However, processing cables of these lengths presents issues with space and storage. A cable coating system that utilized spools to uncoil and recoil the cables while coating them would be necessary to save space. Prior to investment in such a system, small scale testing of the polymer nanocomposites is currently being explored to characterize the materials on a cable analog.

5.1.1 Cable Coating Set-Up

The HTS cable cores explored in this research have a diameter of roughly ¼ in. Without cable cores readily available to test with, ¼ in. stainless steel rods cut to 3 in. in length were implemented as cable core analogs. An adapted form of spin coating was selected to coat the cable analogs. A proof-of-concept system was designed for small scale cable coating, depicted in Figure 43 and Figure 44, and employed a convection furnace to cure the composite. A motor, chain, and sprocket system were utilized to spin the cable analog in the heated environment. The motor is mounted outside the furnace and powered by a

12 V power supply. A speed controller and a magnetic tachometer are also employed to accurately control the speed of the motor.

Figure 43

Rendering of the Initial Proof of Concept Wire-Coating Design

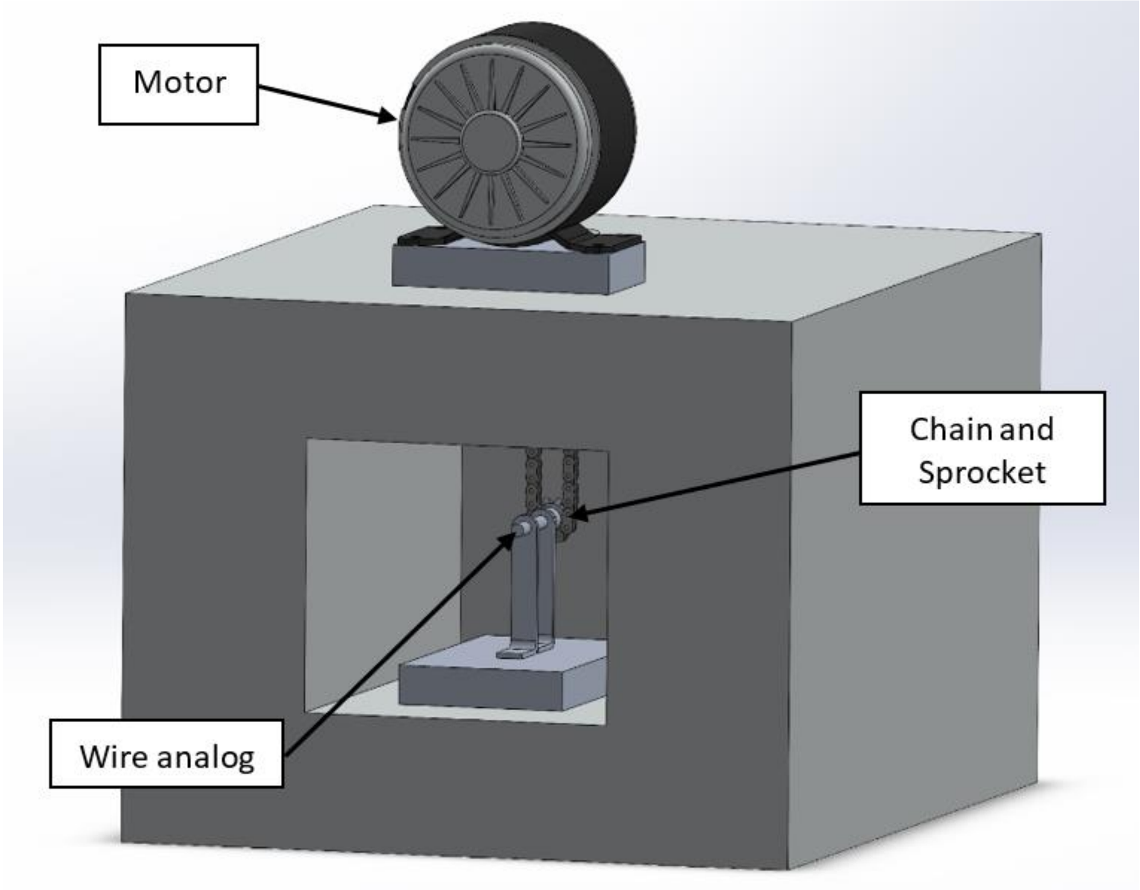

Note. A box with cutouts is employed as a stand-in for the furnace.

Figure 44

Motor, Tachometer, and Speed Controller Set-Up Used to Run the Cable Coating System

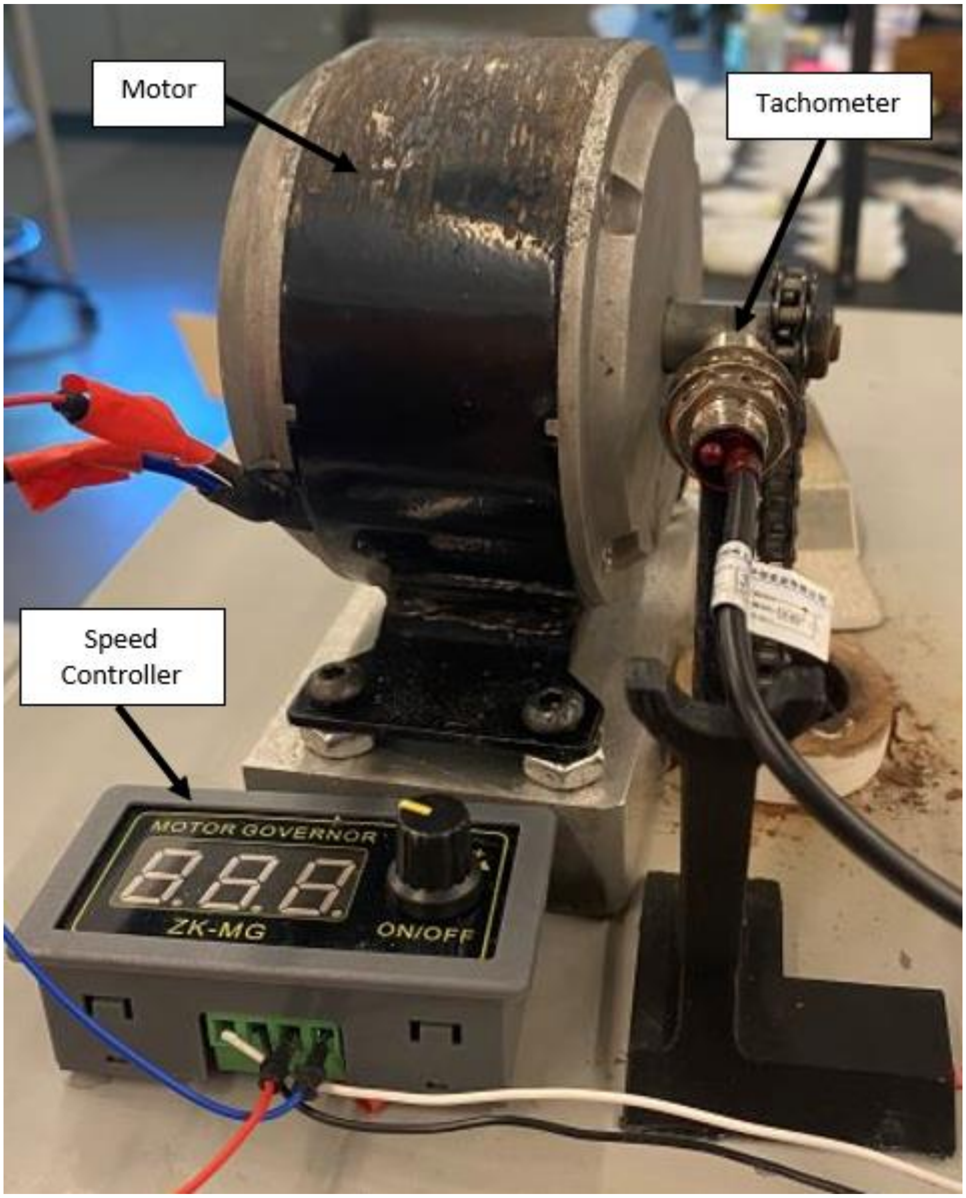

To coat samples, a cable analog is loaded into the coating fixture and placed inside the convection furnace. The coating fixture features two posts with holes in them to hold the cable analog while the analog is being spun. A sprocket is affixed at the end of the analog and engaged with a chain feeding through a vent hole at the top of the furnace. An excess of composite precursor is applied via syringe prior to turning the system on. The motor is turned on and the furnace is heated to the composite's curing temperature. Curing takes place as the analog spins, resulting in a cured polymer nanocomposite coating.

The proof-of-concept system was tested at various spin speeds and was found to successfully coat cable analogs, as shown in Figure 45. The coatings, however, were uneven and displayed varied thicknesses, even among tests at the same spin speed. In an effort to improve coating thicknesses and uniformity, the design was improved to include a cutting edge below the surface of the cable analog. The new coating fixture, displayed in Figure 46, added a holder for a razor to be affixed at different heights. A razor was selected as the cutting edge for ease of replacement and coating finish consistency. Slots were also cut into the posts that hold the analog, enabling threaded rods and hex nuts to secure the razor holder to the fixture at different heights. Adding a cutting edge allowed for more control over both the final thickness of the coating and the amount of material removed during curing. The cable coating system has been tested to examine pure PA coatings and requires further experimentation for developing a standard operating procedure for an ideal spin speed.

Figure 45

Cable Analog After a PA Coating has Been Applied and Cured

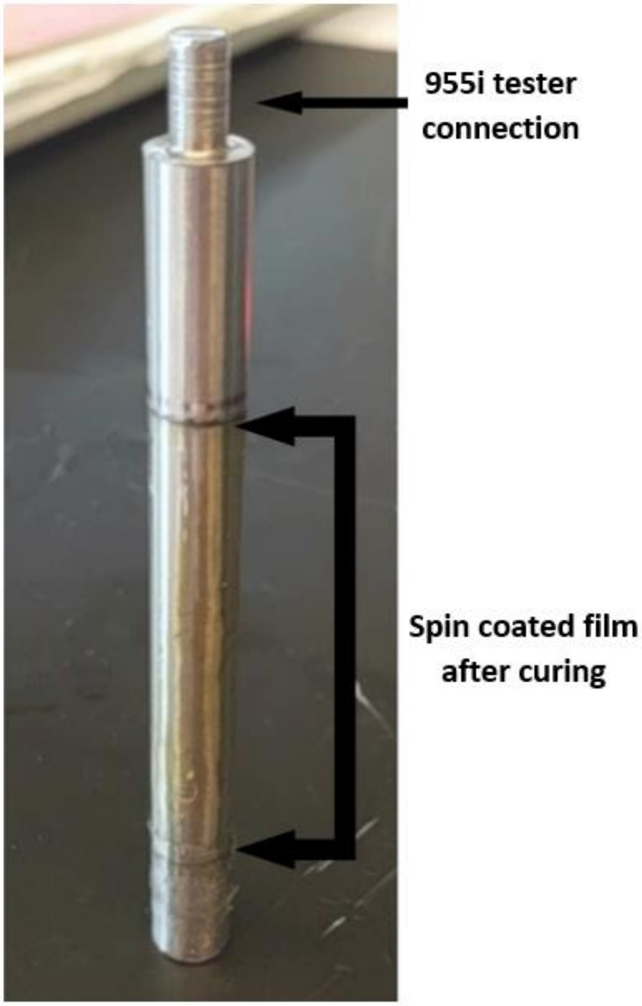

Figure 46

Front and Side View of the Improved Cable Coating Fixture

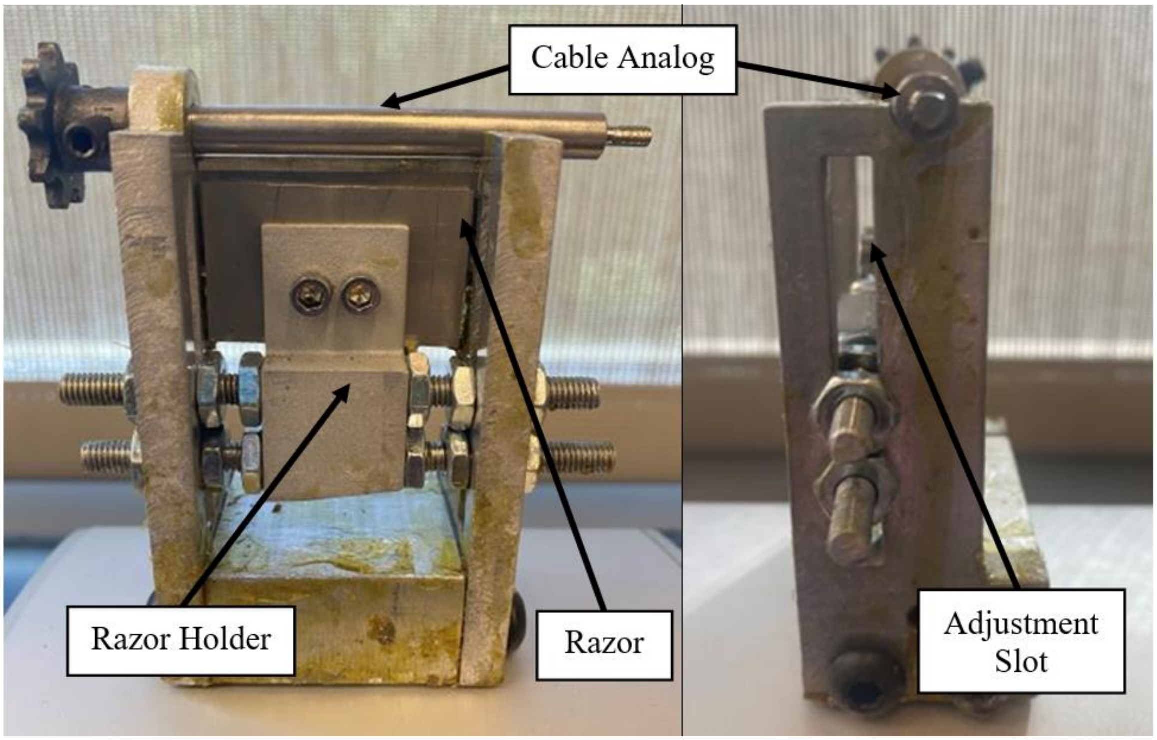

5.1.2 Cable Coated Dielectric Breakdown Fixture

Conducting breakdown on cable coated analogs presents issues with utilizing the ASTM-D3755 in employing two flat electrodes. The room temperature thin film dielectric breakdown fixture lacks a method of securing cable coated analogs during testing. Utilizing two electrodes also introduces inaccuracies in dielectric breakdown data. Breakdown testing in this configuration needs to occur through both sides of the cable to register a failure. This can artificially increase the dielectric strength of the coating if one side is weaker than the other. A new cable coated dielectric breakdown fixture was proposed to mitigate these issues.

The cable coated dielectric breakdown fixture, as depicted in Figure 47, adapts ASTM D3755 and the thin film breakdown fixture for cable coated samples. In this fixture, the electrode pair is replaced with a single top electrode with a curved surface for better contact on the cable coating. The cable coated wire analog is treated as the bottom electrode and machined to allow an alligator clip to connect to the tip, as shown in Figure 45. The top electrode is machined out of stainless steel with a curved surface slightly wider than 0.25 in. in diameter. Coated analogs are placed inside the polylactic acid (PLA) sheathe attached to the bottom of the breakdown fixture. The top electrode interfaces with the analog through a hole in the sheathing. The top electrode and cap are weighted to be 50 g, to abide by ASTM-D3755. Testing is conducted identically to the dielectric breakdown of thin film samples and is facilitated through a 955i hipot tester. After breakdown occurs, the cable coated analog is inspected for a breakdown hole and a micrometer is utilized to measure the thickness near this site. Once coated, the cable coating cannot be removed in one solid layer, introducing slight inaccuracies in thickness measurements and dielectric strength values. The thickness of the coating is determined by subtracting the thickness of the pre-coated analog from the overall thickness of the coating. If the coating is not uniform, the thickness measurement may be skewed, highlighting the importance of the improved cable coating fixture's control over coating thickness and uniformity.

Figure 47

Diagram of the Cable Coated Dielectric Breakdown Fixture

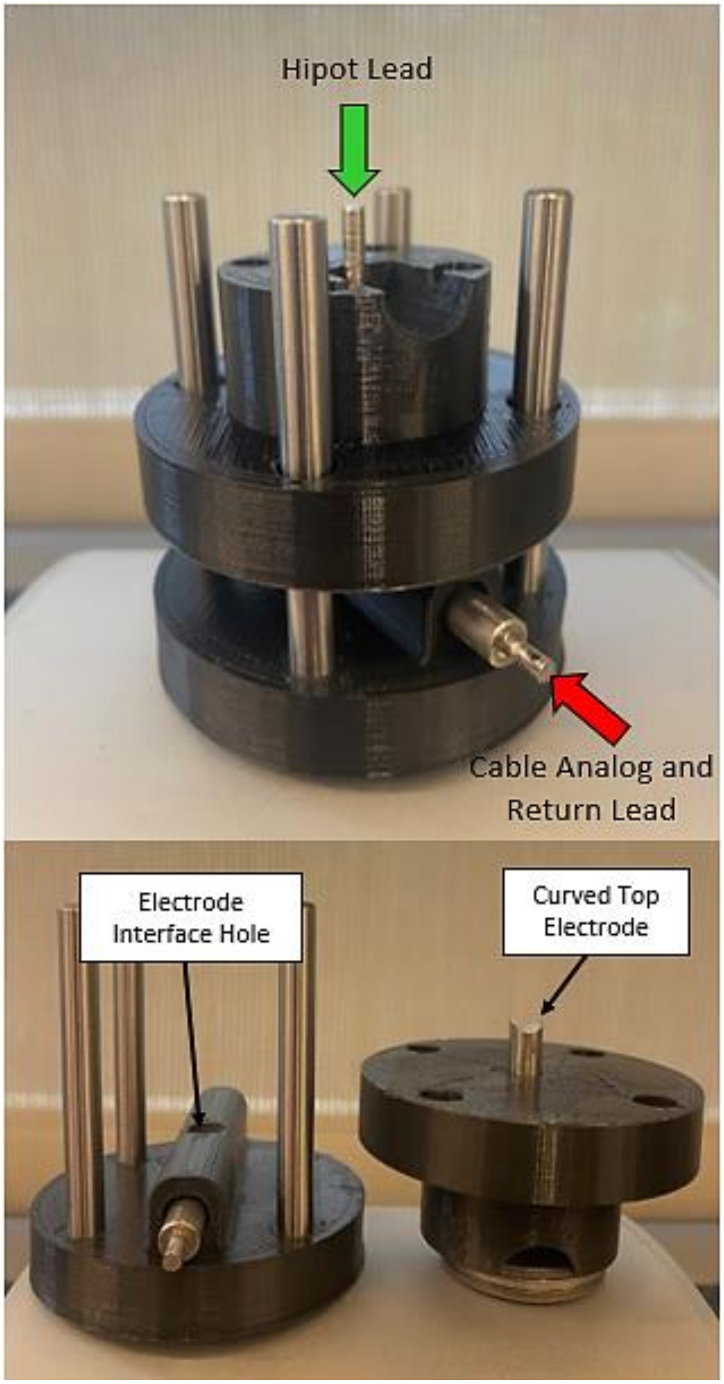

5.2 55 K Testing Chamber Design

Development of the 55 K testing chamber began with utilizing a Gifford-McMahon cryocooler system, provided by the Applied Superconductivity Team at NSWCPD. The system, depicted as a schematic in Figure 48, employs 50 psi gaseous helium, a compressor, a circulation fan, and a cold head to deliver helium at temperatures above 40 K. Helium feeds into the system and is cooled by the cold head’s heat exchanger. The circulating fan helps circulate the cooled gas to cool the helium and its surrounding volume. A vacuum jacket surrounds the cryocooler’s inner volume and all the piping is covered in multi-layer insulation (MLI) to mitigate heat loss. Bayonet fittings are attached at the side to allow the system to create a larger cooling cycle for operation in a larger system. The system also includes a 150 psi pressure release valve, for added safety. A closed loop cooling test was conducted to confirm the cooling capabilities of the system, as temperatures below 50 K were reached after 4 hours.

Figure 48

Schematic of the Closed Loop Gifford-McMahon Cryocooler System

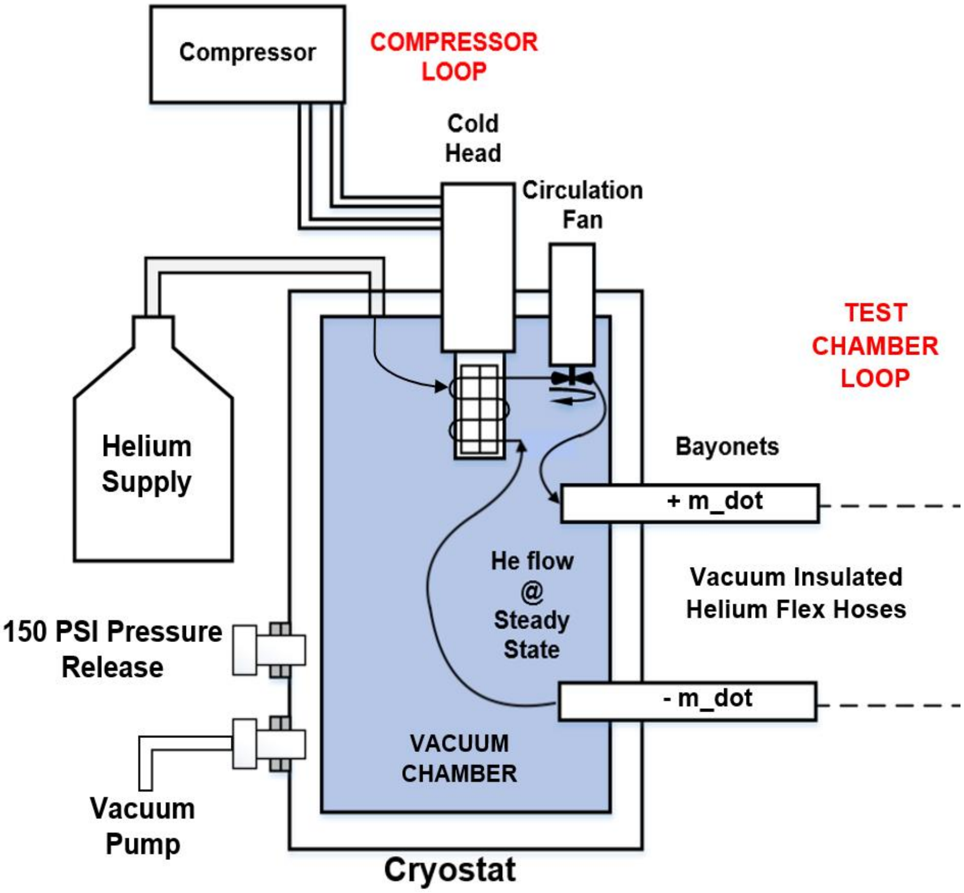

The 55 K testing chamber has been designed to connect to the cryocooler system through the bayonets, creating one large cooling loop. The testing chamber, depicted in Figure 49, is housed within a larger vacuum chamber to mitigate convective heat loss. Flex hoses connect the helium inlet and outlet to the inner testing chamber to mitigate conduction between the connections. The design also features minimal penetrations into the system to further minimize conductive heat loss. The flex hoses and the inner testing chamber are covered with MLI blankets to mitigate radiative heat transfer. The vacuum chamber and

inner testing chamber are fabricated from rolled 304 stainless steel plate and 304 stainless steel pipe weldments, respectively. 304 stainless steel CF flanges with ultra-high vacuum rated copper gaskets provide user entry into the vacuum and testing chambers. Material characterization in this system is facilitated via electrical feedthroughs on the side of the vacuum chamber and the top of the inner testing chamber. The electrical feedthroughs also allow a silicon diode temperature sensor to be used to monitor the temperature in the inner chamber. The system’s current design is focused on dielectric breakdown testing but can be adapted for CTE measurement and other cryogenic material characterization. Orders for all necessary hardware, including the parts needed for the fabrication of the outer vacuum chamber, have been placed. Manufacturing of the inner testing chamber is also currently taking place, allowing the system to be operational in the near future.

Figure 49

Rendering of the 55 K Testing Chamber’s Inner and Outer Vacuum Chambers

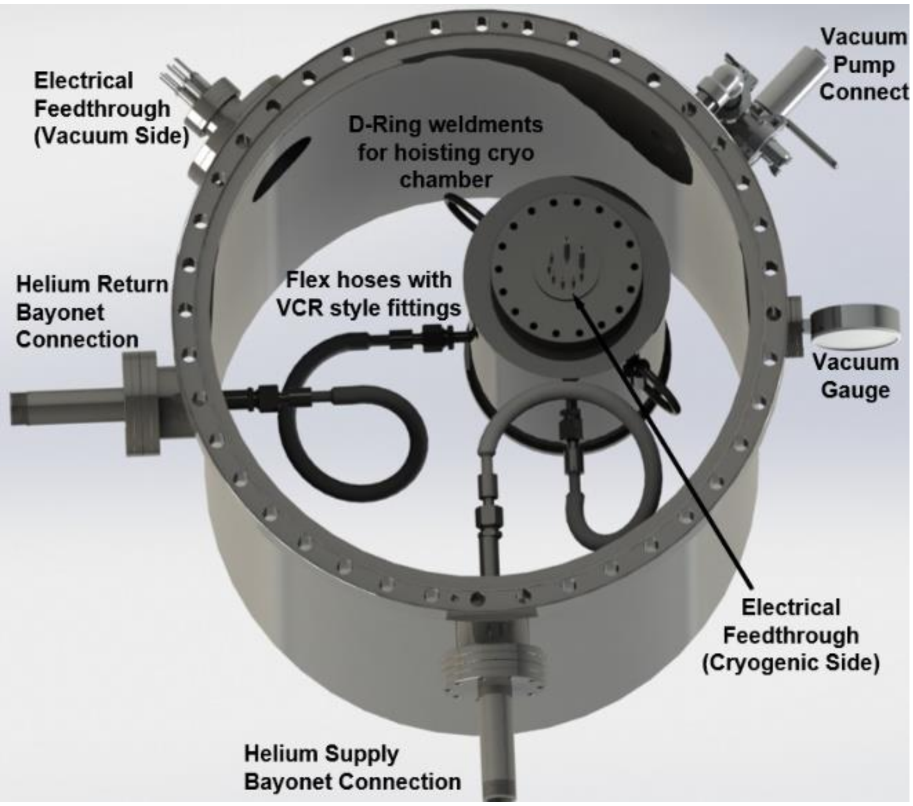

5.3 55 K Dielectric Breakdown Fixture

To conduct dielectric breakdown testing in the 55 K testing chamber, another custom fixture has been designed and is currently being fabricated. The fixture, shown in Figure 50, adapts and improves upon the multi-testing capabilities of the 92 K fixture. In this design, three Teflon “pucks” are to be machined with each of them holding five sheathed electrode pairs. The 15 electrode pairs are identical in design to that of the 92 K testing fixture. This large increase in the number of usable electrode pairs over the 92 K testing fixture is driven by the anticipated long cool down time of the chamber for each testing cycle. The three pucks are fixed at different heights to increase the compactness inside the testing chamber. A hipot wire connects from the electrical feedthrough and runs down the middle of the fixture, supplying power to each electrode pair. Return wires are clipped onto the ends of each pair and connect back to the electrical feedthrough. A plug board utilizing banana plugs, seen in Figure 51, was fabricated to enable both quick swapping and further grounding between electrode pairs during testing. The plug board will connect the 955i tester to the electrical feedthrough, enabling control over which electrode pair is being used to conduct breakdown testing. Upon completion of this fixture, dielectric breakdown testing will be conducted via the 955i hipot tester and with the same voltage ramp speed of 500 V/s.

Figure 50

Rendering of the 55 K Dielectric Breakdown Fixture

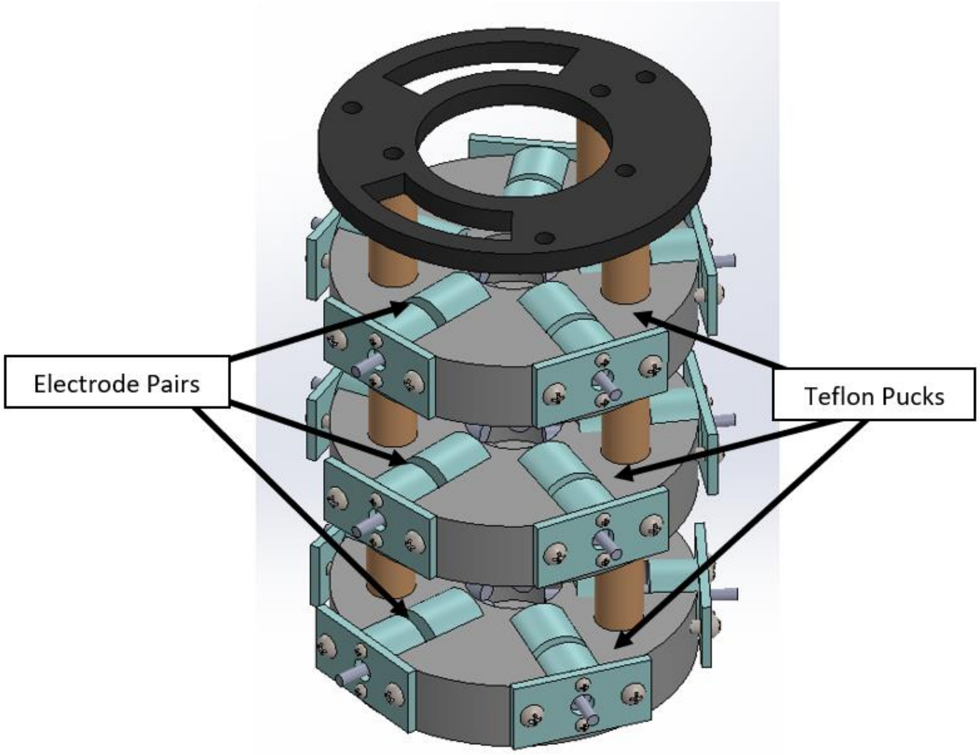

Figure 51

(A) Front and (B) Back of the 55K Dielectric Testing Fixture Plug Board

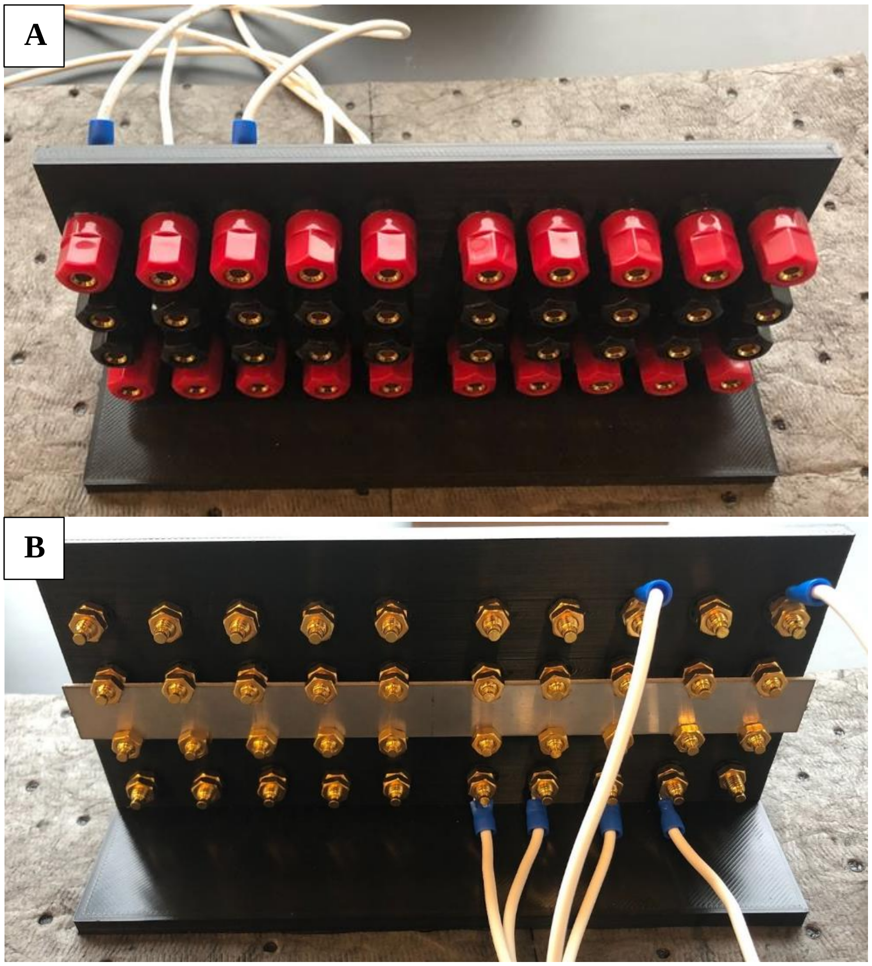

Chapter 6

Conclusions and Future Works

6.1 Summary

In this thesis, three potential polymer nanocomposite dielectrics were explored for adoption into gaseous helium cooled HTS cables. PI, PA, and PMMA all served as host matrices for SiO_2, the nanoparticle filler. In the right concentration, the addition of silica to a polymer host can potentially match the nanocomposite's CTE to that of HTS cable cores, while maintaining a sufficiently high dielectric strength. Each polymer nanocomposite configuration was fabricated in a similar manner, employing *in situ* nanoparticle synthesis. Samples were prepared via spin coating, yielding thin films for use in material characterization and validation efforts.

Polymer nanocomposite samples were characterized through SEM, TGA, FTIR, and dielectric breakdown testing. SEM imaging validated the existence of silica nanoparticles via EDS mapping and examined nanoparticle dispersion within the three host polymers. Each composite configuration yielded varying nanoparticle dispersions with PA-SiO_2 displaying a superior dispersion, and smaller average nanoparticle size, to PI-SiO_2 and PMMA-SiO_2 samples. TGA was utilized to investigate whether all the solvents were removed from the final nanocomposite samples. PA and PI based samples were found to have all their solvents removed while PMMA based samples still had DMF in them. FTIR was employed to validate the synthesis of PMMA and imidization of PA into PI. FTIR was also utilized to examine low temperature imidization reaction experiments. PMMA was found to be difficult to synthesize in-house, leading to the purchase of pre-made PMMA powder for material preparation. The imidization reaction was also proven to take place at high temperatures. However, all low temperature imidization efforts yielded no notable imidization from PA to PI.

Thin film dielectric breakdown testing was conducted at room and cryogenic temperatures to determine the dielectric strength of the composites. ASTM-D3755 standard was employed for breakdown testing at room temperature. This standard was also adapted for cryogenic dielectric breakdown at 92 K in an LN_2 dewar, through the use of a specialized 3-D printed fixture. PI-SiO_2 samples generally exhibited the highest dielectric strength out of the three configurations, with PA-SiO_2 and PMMA-SiO_2 samples exhibiting weaker, yet similar, strengths at both temperatures. PA-SiO_2 and PMMA-SiO_2 samples also performed similarly at room and cryogenic temperatures. All three composite configurations showed large increases in dielectric strength when going from room to cryogenic temperature breakdown testing. The increase in strength based on temperature change can be explained through the lower temperature's effect on charge carriers and the shrinking transition region around nanoparticles. SEM images of breakdown holes also displayed differences in shape and geometry when comparing holes at room and cryogenic temperatures. After all material characterization efforts, PA-SiO_2 was determined to be the most likely candidate for adoption into gaseous helium cooled HTS cables. PA based materials were selected because of their low processing temperature, adequate dielectric strength, superior dispersion, and lack of un-vaporized solvent, when compared to PI-SiO_2 and PMMA-SiO_2.

Further characterization of the dielectric breakdown behavior of polymer nanocomposites is required prior to adoption into HTS cable dielectrics. Preparation of polymer nanocomposites as cable coatings is expected to result in lower dielectric performance, necessitating characterization of the materials on a wire analog. A proof-of-concept design, which involves a rotating stainless-steel wire analog via a sprocket, chain, and motor system, was developed to prepare cable coatings. A cable coating fixture was also fabricated to include a cutting edge which aided in coating uniformity. Dielectric breakdown testing of cable coatings required the fabrication of a specialized breakdown fixture. This fixture functions by employing the cable analog as one of the electrodes during testing. Further testing is required to develop a standard operating procedure for polymer composite cable coatings before cable coated breakdown data can be compiled. A cryogenic testing chamber was also designed and is currently being manufactured, to allow for material characterization at 55 K. This chamber connects to a cryocooler system and is currently focused on dielectric breakdown testing; however, it can be adapted for other cryogenic material property characterization such as thermomechanical testing. Dielectric breakdown at 55 K is a time consuming process, leading to a design of a dielectric breakdown fixture that allows for 15 tests during each cool down cycle. Upon competition of the chamber and the dielectric breakdown fixture, polymer nanocomposite thin films can be validated at the 55 K operating temperature of the HTS cables.

The research presented herein expands the fields of polymer nanocomposites, cryogenic dielectrics, and HTS cable research. The results collected across this project have led to multiple publications detailing the *in situ* polymer nanocomposite fabrication process, the behavior of nanocomposites in cryogenic environments, and the impact dielectric breakdown has on polymer nanocomposites. A comparison between the dielectric breakdown behaviors of various other studies and the results presented in this thesis is displayed in Table 7. The expanded, temperature-dependent model of dielectric breakdown is novel, as previous works on the subject of breakdown focus on room temperature data and models. The work presented here also advances naval research into gaseous helium cooled HTS cables, as an adequate dielectric layer is close to being validated for use in the cables. Through continued efforts into this work, the materials investigated within this research may solve the issues with current HTS cable dielectrics and improve the efficiency of HTS cable systems in naval applications.

Table 7

Comparison of Polymer Composites' Dielectric Strengths Across Various Studies

Ref.	Testing Temperature (K)	Host Matrix	Nanofiller	Conc. (%)	Dielectric Strength (kV/mm)
[81]	77	Araldite®	$BaTiO_3$	0	97
				10	91
		Polyvinyl Alcohol	$BaTiO_3$	0	95
				10	105
			TiO_2	0	96
				25	119
		Polymethyl Methacrylate	$CoFe_2O_4$	0	139
				2	145
			BaF_2	0	139
				5	161
[82]	300	Polystyrene	SiO_2	0	400
				5	420
		Poly-4-Vinylpridene		0	490
				5	490
		Polymethyl Methacrylate		0	815
				5	580
		Polyimide		0	570
				5	530

Ref.	Testing Temperature (K)	Host Matrix	Nanofiller	Conc. (%)	Dielectric Strength (kV/mm)
[83]	300	High Density Polyethylene	SiO_2	0	22
				5	20
This Thesis	300	Polyimide	SiO_2	0	261
				6	158
		Polyamide		0	135
				6	90
		Polymethyl methacrylate		0	157
				6	86
	92	Polyimide	SiO_2	0	347
				6	261
		Polyamide		0	261
				6	149
		Polymethyl methacrylate		0	198
				6	292

6.2 Future Works

The research being conducted in this project is still ongoing and future research focuses on improving upon the materials and results presented here. Future researchers will also be focused on developing a greater understanding of the proposed polymer nanocomposites as they would perform in HTS cables. Continued efforts into the following areas are required to confirm the ideal polymer nanocomposite configuration for HTS cable dielectrics and to develop a process of coating HTS cables:

1) PMMA solvent evaporation: PMMA composites are currently prepared by dissolving premade PMMA powders in DMF. The PMMA composites are subsequently cured at 125 °C to avoid reaching the delamination temperature of HTS cables. However, this temperature is below the boiling point of DMF at

153 °C, meaning DMF is still present in the final samples. The effect the un-vaporized DMF has on the material properties of PMMA composites is unknown, and could present issues at 55 K. This added DMF also skews the concentration calculation of composite samples, making accurate material preparation difficult. Moving forward, a vacuum oven or another solvent with a lower boiling point could be employed to ensure that no solvent is left in the final PMMA composite samples.

2) Improved nanoparticle dispersion and size: As stated previously, particles must be smaller than 100 nm to be considered nanoparticles. The nanocomposites explored in this work all exhibit agglomerations and large nanoparticles. Improving dispersion quality and decreasing average particle size is likely to improve the mechanical properties of the final materials. This is possible by conducting a parametric study of the mixing times of the sol gel reagents, the mixing time of the sol gel within the polymer host, and the temperature of the sol gel as it forms. As a better understanding of the sol gel process is developed, greater control over the dispersion and particle sizes can be achieved.
3) Characterization of further material properties: Material characterization has previously focused primarily on the dielectric strength of the polymer nanocomposites at temperatures above 55 K. Prior to adoption into HTS cables, the tensile strength, CTE, and the effect the cyclic thermal loading has on the polymer nanocomposites should be explored. Characterizing the tensile strength and CTE of PA-SiO_2 and potentially PMMA-SiO_2 in the future is imperative to ensure these materials will not form cracks or breaks at 55 K as

cable coatings. The cables are also likely to be cooled from room temperature to 55K and back multiple times over the lifespan of the HTS cables. Understanding the effects this cyclic thermal loading has on the polymer nanocomposites is valuable to determine their life span as cable coatings. The completion of the 55 K testing chamber will allow for data on these material properties to be explored in great detail.

4) Large-scale wire coating system: The proof-of-concept wire coating system has allowed for preliminary testing of polymer nanocomposites as cable coatings. Currently, only pure PA has been successfully coated on cable analogs. Further testing is necessary to deliver a process that prepares uniform and reliable coatings prior to conducting dielectric breakdown testing as cable coatings. This process should be expanded to PA-SiO_2 composites and potentially PMMA composites. The data being collected from the proof-of-concept system represents small-scale testing and will enable efforts to address full scale cable coating operations. HTS cables are fabricated in 50-100 m sections, highlighting the need to develop a method of coating long cable sections. A large scale, spool-to-spool cable coating system, that employs a form of polymer extrusion, should be designed to enable the adoption of polymer nanocomposites onto HTS cables.

5) Aging study of dielectrics: When collecting data on dielectric breakdown, samples are prepared as required and are utilized in a timely manner. This means the effect time has on the stability of the composites has not been a quantified. Therefore, an aging study, to determine the shelf life of the

nanocomposites, should be conducted. This study can be achieved over a long period of time (>1-2 years) by preparing a sample and storing it, or over a shorter period of time, artificially. The results of this aging study would help determine the maintenance requirements of HTS cables and further aid in understanding the lifetime of their nanocomposite dielectrics.

References

[1] T. Masuda *et al.*, "High-temperature superconducting cable technology and development trends," *SEI Technical Review*, pp. 8-13, 01/01 2005.

[2] K. Hamidieh, "A data-driven statistical model for predicting the critical temperature of a superconductor," *Computational Materials Science*, vol. 154, pp. 346-354, 2018/11/01/ 2018, doi: https://doi.org/10.1016/j.commatsci.2018.07.052.

[3] J. Lee, G. Hwang, S. Jeong, B. J. Park, and Y. H. Han, "Design of high efficiency mixed refrigerant Joule–Thomson refrigerator for cooling HTS cable," *Cryogenics,* vol. 51, no. 7, pp. 408-414, 2011/07/01/ 2011, doi: https://doi.org/10.1016/j.cryogenics.2011.04.007.

[4] M. Frank, F. Merschel, M. Noe and A. Hobl, "AmpaCity project—Update on World's first superconducting cable and fault current limiter installation in a German city center", *Proc. IEEE 12th EUCAS*, pp. 1-4, Sep. 2015.

[5] U.S. Department of Energy. (2007). *A National Effort to Introduce New Technology into the Power Delivery Infrastructure*.

[6] H. Yumura *et al.*, "Phase II of the Albany HTS cable project," *IEEE transactions on applied superconductivity*, vol. 19, no. 3, pp. 1698-1701, 2009.

[7] M. Stemmle, F. Merschel, M. Noe, and A. Hobl, "AmpaCity—Advanced superconducting medium voltage system for urban area power supply," in *2014 IEEE PES T&D Conference and Exposition*, 2014: IEEE, pp. 1-5.

[8] S. Honjo *et al.*, "Status of superconducting cable demonstration project in Japan," *IEEE transactions on Applied Superconductivity*, vol. 21, no. 3, pp. 967-971, 2010.

[9] D. Patterson *et al.*, "Design and simulation of a permanent-magnet electromagnetic aircraft launcher," *IEEE Transactions on Industry Applications*, vol. 41, no. 2, pp. 566-575, 2005.

[10] B. K. Fitzpatrick, J. T. Kephartl, and E. M. Golda, "Characterization of gaseous helium flow cryogen in a flexible cryostat for naval applications of high temperature superconductors," *IEEE Transactions on Applied Superconductivity,* vol. 17, no. 2, pp. 1752-1755, 2007.

[11] J. T. Kephart, B. K. Fitzpatrick, P. Ferrara, M. Pyryt, J. Pienkos, and E. M. Golda, "High Temperature Superconducting Degaussing From Feasibility Study to Fleet Adoption," *IEEE Transactions on Applied Superconductivity,* vol. 21, no. 3, pp. 2229-2232, 2011, doi: 10.1109/TASC.2010.2092746.

[12] E. B. Forsyth, "The dielectric insulation of superconducting power cables," *Proceedings of the IEEE,* vol. 79, no. 1, pp. 31-40, 1991, doi: 10.1109/5.64381.

[13] M. Kosaki, "Research and development of electrical insulation of superconducting cables by extruded polymers," *IEEE Electrical Insulation Magazine,* vol. 12, no. 5, pp. 17-24, 1996.

[14] M. Kosaki, M. Nagao, Y. Mizuno, N. Shimizu, and K. Horii, "Development of extruded polymer insulated superconducting cable," *Cryogenics,* vol. 32, no. 10, pp. 885-894, 1992.

[15] M. G. Danikas and T. Tanaka, "Nanocomposites-a review of electrical treeing and breakdown," *IEEE Electrical Insulation Magazine,* vol. 25, no. 4, pp. 19-25, 2009.

[16] P. Cheetham, J. Viquez, W. Kim, L. Graber, C. H. Kim, and S. V. Pamidi, "High-Temperature Superconducting Cable Design Based on Individual Insulated Conductors," *Advances in Materials Science and Engineering,* vol. 2018, p. 3637873, 2018/11/01 2018, doi: 10.1155/2018/3637873.

[17] J. Ekin, *Experimental techniques for low-temperature measurements: cryostat design, material properties and superconductor critical-current testing*. Oxford university press, 2006.

[18] L. Shengtao, Y. Guilai, B. Suna, and L. Jianying, "A new potential barrier model in epoxy resin nanodielectrics," *IEEE transactions on dielectrics and electrical insulation*, vol. 18, no. 5, pp. 1535-1543, 2011, doi: 10.1109/TDEI.2011.6032822.

[19] C. B. Anna, E. Todd, and P. R. Thomas, "Nanoparticle Polymer Composites: Where Two Small Worlds Meet," *Science (American Association for the Advancement of Science),* vol. 314, no. 5802, pp. 1107-1110, 2006, doi: 10.1126/science.1130557.

[20] Y.-J. Kim, J.-H. Kim, S.-W. Ha, D. Kwon, and J.-K. Lee, "Polyimide nanocomposites with functionalized SiO2 nanoparticles: enhanced processability, thermal and mechanical properties," *RSC Advances,* vol. 4, no. 82, pp. 43371-43377, 2014.

[21] X.-G. Chen, J.-D. Guo, B. Zheng, Y.-Q. Li, S.-Y. Fu, and G.-H. He, "Investigation of thermal expansion of PI/SiO2 composite films by CCD imaging technique from− 120 to 200° C," *Composites science and technology,* vol. 67, no. 14, pp. 3006-3013, 2007.

[22] P. V. Komarov, Y. T. Chiu, S. M. Chen, and P. Reineker, "Investigation of thermal expansion of polyimide/SiO2 nanocomposites by molecular dynamics simulations," *Macromolecular theory and simulations,* vol. 19, no. 1, pp. 64-73, 2010.

[23] X. Cui *et al.*, "Mechanical and dielectric properties of polyimide/silica nanocomposite films," *Plastics, Rubber & Composites,* Article vol. 44, no. 10, pp. 435-439, 2015, doi: 10.1080/14658011.2015.1104087.

[24] S. i. Numata, S. Oohara, K. Fujisaki, J. I. Imaizumi, and N. Kinjo, "Thermal expansion behavior of various aromatic polyimides," *Journal of applied polymer science,* vol. 31, no. 1, pp. 101-110, 1986.

[25] E. Sacher, "Dielectric Properties of Polyimide Film. II. DC Properties," *IEEE Transactions on Electrical Insulation,* vol. EI-14, no. 2, pp. 85-93, 1979, doi: 10.1109/TEI.1979.298160.

[26] M. Li *et al.*, "Enhanced the mechanical strength of polyimide (PI) nanofiber separator via PAALi binder for lithium ion battery," *Composites communications,* vol. 24, 2021, doi: 10.1016/j.coco.2020.100607.

[27] W. Chen, W. Chen, B. Zhang, S. Yang, and C.-Y. Liu, "Thermal imidization process of polyimide film: Interplay between solvent evaporation and imidization," *Polymer,* vol. 109, pp. 205-215, 2017/01/27/ 2017, doi: https://doi.org/10.1016/j.polymer.2016.12.037.

[28] M. Heinle and D. Drummer, "Temperature-dependent coefficient of thermal expansion (CTE) of injection molded, short-glass-fiber-reinforced polymers," *Polymer Engineering & Science*, vol. 55, no. 11, pp. 2661-2668, 2015.

[29] D. Zhang *et al.*, "Fabrication of high-temperature aromatic polyamides with ultra-high breakdown strength via complex-assisted chain arrangement," *Chemical Engineering Journal*, vol. 432, p. 134407, 2022/03/15/ 2022, doi: https://doi.org/10.1016/j.cej.2021.134407.

[30] L. Nasrat, A. Eid, A. Fahmy, and S. Qenawy, "Electrical and Mechanical Properties of Aromatic Polyamide/Polyester Composites," *International Research Journal of Innovations in Engineering and Technology,* vol. 5, no. 7, p. 46, 2021.

[31] N. Fuse, M. Kozako, T. Tanaka, and Y. Ohki, "Effects of mica fillers on dielectric properties of polyamide nanocomposites," in *CEIDP'05. 2005 Annual Report Conference on Electrical Insulation and Dielectric Phenomena, 2005.*, 2005: IEEE, pp. 148-151.

[32] J. T. Cook, H. M. Hones, J. R. Mahon, L. Yu, R. R. Krchnavek, and W. Xue, "Temperature-Dependent Dielectric Properties of Polyimide (PI) and Polyamide (PA) Nanocomposites," *IEEE Transactions on Nanotechnology,* vol. 20, pp. 584-591, 2021.

[33] M. Buccella, A. Dorigato, E. Pasqualini, M. Caldara, and L. Fambri, "Chain extension behavior and thermo-mechanical properties of polyamide 6 chemically modified with 1,1′-carbonyl-bis-caprolactam," *Polymer engineering and science,* vol. 54, no. 1, pp. 158-165, 2014, doi: 10.1002/pen.23547.

[34] F. Yang and G. L. Nelson, "PMMA/silica nanocomposite studies: synthesis and properties," *Journal of applied polymer science,* vol. 91, no. 6, pp. 3844-3850, 2004.

[35] V. Charlot, A. Ibrahim, X. Allonas, C. Croutxé-Barghorn, and C. Delaite, "Photopolymerization of methyl methacrylate: effects of photochemical and photonic parameters on the chain length," *Polymer Chemistry,* vol. 5, no. 21, pp. 6236-6243, 2014.

[36] X. Huang and W. J. Brittain, "Synthesis and characterization of PMMA nanocomposites by suspension and emulsion polymerization," *Macromolecules,* vol. 34, no. 10, pp. 3255-3260, 2001.

[37] J. H. Park, D. K. Hwang, J. Lee, S. Im, and E. Kim, "Studies on poly(methyl methacrylate) dielectric layer for field effect transistor: Influence of polymer tacticity," *Thin Solid Films,* vol. 515, no. 7, pp. 4041-4044, 2007/02/26/ 2007, doi: https://doi.org/10.1016/j.tsf.2006.10.121.

[38] S. K. Griffiths, J. Crowell, B. Kistler, and A. Dryden, "Dimensional errors in LIGA-produced metal structures due to thermal expansion and swelling of PMMA," *Journal of Micromechanics and Microengineering,* vol. 14, no. 11, p. 1548, 2004.

[39] H. Q. Zhang, Y. Jin, and Y. Qiu, "The optical and electrical characteristics of PMMA film prepared by spin coating method," *IOP Conference Series: Materials Science and Engineering,* vol. 87, p. 012032, 2015/07/16 2015, doi: 10.1088/1757-899x/87/1/012032.

[40] C. Osburn and D. Ormond, "Dielectric breakdown in silicon dioxide films on silicon: I. Measurement and interpretation," *Journal of The Electrochemical Society,* vol. 119, no. 5, p. 591, 1972.

[41] Y. Hu, D. Diehl, Q. Liu, C. Zhao, and E. Irene, "In situ real time measurement of the incubation time for silicon nucleation on silicon dioxide in a rapid thermal process," *Applied physics letters,* vol. 66, no. 6, pp. 700-702, 1995.

[42] K. Achuthan, J. Curry, M. Lacy, D. Campbell, and S. Babu, "Investigation of pad deformation and conditioning during the CMP of silicon dioxide films," *Journal of Electronic Materials,* vol. 25, no. 10, pp. 1628-1632, 1996.

[43] Y. Hoshikawa, H. Yabe, A. Nomura, T. Yamaki, A. Shimojima, and T. Okubo, "Mesoporous silica nanoparticles with remarkable stability and dispersibility for antireflective coatings," *Chemistry of Materials,* vol. 22, no. 1, pp. 12-14, 2010.

[44] C. J. Huang, S. Y. Fu, Y. H. Zhang, B. Lauke, L. F. Li, and L. Ye, "Cryogenic properties of SiO2/epoxy nanocomposites," *Cryogenics (Guildford),* vol. 45, no. 6, pp. 450-454, 2005, doi: 10.1016/j.cryogenics.2005.03.003.

[45] S. Li *et al.*, "Short-term breakdown and long-term failure in nanodielectrics: a review," *IEEE Transactions on Dielectrics and Electrical Insulation,* vol. 17, no. 5, pp. 1523-1535, 2010.

[46] T. Tanaka, "Dielectric nanocomposites with insulating properties," *IEEE Transactions on Dielectrics and Electrical Insulation,* vol. 12, no. 5, pp. 914-928, 2005, doi: 10.1109/TDEI.2005.1522186.

[47] Y. Zare and K. Y. Rhee, "A multistep methodology for calculation of the tensile modulus in polymer/carbon nanotube nanocomposites above the percolation threshold based on the modified rule of mixtures," *RSC advances,* vol. 8, no. 54, pp. 30986-30993, 2018.

[48] C. H. Kim, S.-K. Kim, L. Graber, and S. V. Pamidi, "Cryogenic thermal studies on terminations for helium gas cooled superconducting cables," *Physics Procedia,* vol. 67, pp. 201-207, 2015.

[49] N. Suttell, C. H. Kim, J. Ordonez, D. Shah, L. Graber, and S. Pamidi, "Thermal modeling of gaseous helium as a cryogen for high temperature superconducting cable components," *IEEE transactions on applied superconductivity,* vol. 25, no. 3, pp. 1-5, 2014.

[50] S. Ilican, Y. Caglar, and M. Caglar, "Preparation and characterization of ZnO thin films deposited by sol-gel spin coating method," *Journal of optoelectronics and advanced materials,* vol. 10, no. 10, pp. 2578-2583, 2008.

[51] L. L. Hench and J. K. West, "The sol-gel process," *Chemical reviews,* vol. 90, no. 1, pp. 33-72, 1990.

[52] R. Lindberg, J. Sjöblom, and G. Sundholm, "Preparation of silica particles utilizing the sol-gel and the emulsion-gel processes," *Colloids and Surfaces A: Physicochemical and Engineering Aspects,* vol. 99, no. 1, pp. 79-88, 1995/06/10/ 1995, doi: https://doi.org/10.1016/0927-7757(95)03117-V.

[53] M. McCaffrey, H. Hones, J. Cook, R. Krchnavek, and W. Xue, "Geometric analysis of dielectric failures in polyimide/silicon dioxide nanocomposites," *Polymer Engineering & Science,* vol. 59, no. 9, pp. 1897-1904, 2019.

[54] W. Stöber, A. Fink, and E. Bohn, "Controlled growth of monodisperse silica spheres in the micron size range," *Journal of colloid and interface science,* vol. 26, no. 1, pp. 62-69, 1968.

[55] H. M. Hones, "Polyimide / silicon dioxide nanocomposites as dielectrics for helium-cooled high-temperature superconducting cables," Rowan University, Glassboro, N.J, 2020.

[56] K. Yang, D. D. Edie, D. Lim, Y. Kim, and Y. Choi, "Preparation of carbon fiber web from electrostatic spinning of PMDA-ODA poly (amic acid) solution," *Carbon,* vol. 41, no. 11, pp. 2039-2046, 2003.

[57] W. Chen, W. Chen, B. Zhang, S. Yang, and C.-Y. Liu, "Thermal imidization process of polyimide film: Interplay between solvent evaporation and imidization," *Polymer (Guilford),* vol. 109, pp. 205-215, 2017, doi: 10.1016/j.polymer.2016.12.037.

[58] Y. Song, J. Yu, D. Dai, L. Song, and N. Jiang, "Effect of silica particles modified by in-situ and ex-situ methods on the reinforcement of silicone rubber," *Materials & Design,* vol. 64, pp. 687-693, 2014.

[59] M. K. Poddar, S. Pradhan, V. S. Moholkar, M. Arjmand, and U. Sundararaj, "Ultrasound–assisted synthesis and characterization of polymethyl methacrylate/reduced graphene oxide nanocomposites," *AIChE Journal,* vol. 64, no. 2, pp. 673-687, 2018.

[60] Y. T. Hong, M. Y. Jin, D. H. Suh, J. H. Lee, and K. Y. Choi, "New preparation method of poly (amide-imide) s using direct polycondensation with thionyl chloride and their characterization," *Die Angewandte Makromolekulare Chemie: Applied Macromolecular Chemistry and Physics,* vol. 248, no. 1, pp. 105-122, 1997.

[61] J.-Y. Zhang and I. W. Boyd, "UV light-induced deposition of low dielectric constant organic polymer for interlayer dielectrics," *Optical Materials,* vol. 9, no. 1-4, pp. 251-254, 1998.

[62] A. Amini Majd, M. Mortezaei, and I. Amiri Amraei, "Curing behavior, thermal, and mechanical properties of epoxy/polyamic acid based on 4, 4′-biphtalic dianhydride and 3, 3′-dihydroxybenzidine," *Polymer Engineering & Science,* vol. 60, no. 8, pp. 1917-1929, 2020.

[63] D. Moncrieff, V. Robinson, and L. Harris, "Charge neutralisation of insulating surfaces in the SEM by gas ionisation," *Journal of Physics D: Applied Physics,* vol. 11, no. 17, p. 2315, 1978.

[64] R. Sindhu, P. Binod, and A. Pandey, "Chapter 17 - Microbial Poly-3-Hydroxybutyrate and Related Copolymers," in *Industrial Biorefineries & White Biotechnology*, A. Pandey, R. Höfer, M. Taherzadeh, K. M. Nampoothiri, and C. Larroche Eds. Amsterdam: Elsevier, 2015, pp. 575-605.

[65] D. Cho and L. T. Drzal, "Characterization, properties, and processing of LaRC™ PETI-5 as a high-temperature sizing material. I. FTIR studies on imidization and phenylethynyl end-group reaction behavior," *Journal of applied polymer science,* vol. 76, no. 2, pp. 190-200, 2000.

[66] Y. Ji *et al.*, "DFT-calculated IR spectrum amide I, II, and III band contributions of N-methylacetamide fine components," *ACS omega,* vol. 5, no. 15, pp. 8572-8578, 2020.

[67] Y. Chen and J. O. Iroh, "Synthesis and characterization of polyimide/silica hybrid composites," *Chemistry of materials,* vol. 11, no. 5, pp. 1218-1222, 1999.

[68] V. V. Soman and D. S. Kelkar, "FTIR studies of doped PMMA-PVC blend system," in *Macromolecular symposia*, 2009, vol. 277, no. 1: Wiley Online Library, pp. 152-161.

[69] X. Zheng, J. Liu, K. Wang, R. Liu, Y. Yuan, and X. Liu, "Preparation of polyimide/amino-modified reduced graphene oxide composite matrix and its application in UV-cured functionalized films," *Progress in Organic Coatings,* vol. 124, pp. 122-128, 2018/11/01/ 2018, doi: https://doi.org/10.1016/j.porgcoat.2018.08.002.

[70] J. Kuffel and P. Kuffel, *High voltage engineering fundamentals*. Elsevier, 2000.

[71] J. Artbauer, "Electric strength of polymers," *Journal of Physics D: Applied Physics,* vol. 29, no. 2, p. 446, 1996.

[72] P. Barber *et al.*, "Polymer composite and nanocomposite dielectric materials for pulse power energy storage," *Materials,* vol. 2, no. 4, pp. 1697-1733, 2009.

[73] U. Burman and P. Kumar, "Plant response to engineered nanoparticles," in *Nanomaterials in Plants, Algae, and Microorganisms*: Elsevier, 2018, pp. 103-118.

[74] D. Q. Tan, "The search for enhanced dielectric strength of polymer-based dielectrics: a focused review on polymer nanocomposites," *Journal of Applied Polymer Science,* vol. 137, no. 33, p. 49379, 2020.

[75] H. Lee, N. J. Smith, C. G. Pantano, E. Furman, and M. T. Lanagan, "Dielectric breakdown of thinned BaO–Al2O3–B2O3–SiO2 glass," *Journal of the American Ceramic Society,* vol. 93, no. 8, pp. 2346-2351, 2010.

[76] K. Tienda *et al.*, "Investigation of glass transition temperature for polyimide composites: Study of influence of specimen thickness and thermo-mechanical response," in *SAMPE International Technical Conference, Long Beach, CA (May 2013)*, 2013.

[77] S. A. Jenekhe and M. F. Roberts, "Effects of intermolecular forces on the glass transition of polymers," *Macromolecules,* vol. 26, no. 18, pp. 4981-4983, 1993.

[78] T. Agag, T. Koga, and T. Takeichi, "Studies on thermal and mechanical properties of polyimide–clay nanocomposites," *Polymer,* vol. 42, no. 8, pp. 3399-3408, 2001.

[79] B. J. Ash, R. W. Siegel, and L. S. Schadler, "Glass-transition temperature behavior of alumina/PMMA nanocomposites," *Journal of Polymer Science Part B: Polymer Physics,* vol. 42, no. 23, pp. 4371-4383, 2004.

[80] S. Li, L. Yang, W. Liu, and W. Wang, "Dielectric Breakdown of Polymer Nanocomposites," in *Tailoring of Nanocomposite Dielectrics: From Fundamentals to Devices and Applications*, T. Tanaka and A. S. Vaughan Eds. New York, NY: Jenny Stanford Publishing, 2016, ch. 9, pp. 243-280.

[81] E. Tuncer *et al.*, "Nanodielectrics for cryogenic applications," *IEEE transactions on applied superconductivity*, vol. 19, no. 3, pp. 2354-2358, 2009.

[82] S. Abdalla, F. Al-Marzouki, A. Obaid, and S. Gamal, "Effect of Addition of Colloidal Silica to Films of Polyimide, Polyvinylpyridine, Polystyrene, and Polymethylmethacrylate Nano-Composites," (in eng), *Materials (Basel),* vol. 9, no. 2, p. 104, 2016, doi: 10.3390/ma9020104.

[83] P. T.A, S. R. J, and S. R.R.N, "Comparative study of dielectric and mechanical properties of HDPE-MWCNT-SiO2 nanocomposites," *Materials Research Bulletin*, vol. 83, pp. 294-301, 2016/11/01/ 2016, doi: https://doi.org/10.1016/j.materresbull.2016.06.017.